5-2009

Design of a "Figure-8" Spherical Motion Flapping Wing for Miniature UAV's

Zohaib Parvaiz Rehmat
University of Nevada, Las Vegas

Follow this and additional works at: https://digitalscholarship.unlv.edu/thesesdissertations

Part of the Aeronautical Vehicles Commons, Mechanical Engineering Commons, Navigation, Guidance, Control and Dynamics Commons, and the Structures and Materials Commons

Repository Citation

DESIGN OF A "FIGURE – 8" SPHERICAL MOTION FLAPPING

WING FOR MINIATURE UAV'S

by

Zohaib Parvaiz Rehmat

Bachelor of Science
Vaughn College of Aeronautics and Technology, New York, USA
2005

A thesis submitted in partial fulfillment
of the requirements for the

Master of Science Degree in Mechanical Engineering
Department of Mechanical Engineering
Howard R. Hughes College of Engineering

Graduate College
University of Nevada, Las Vegas
May 2009

UMI Number: 1472437

INFORMATION TO USERS

The quality of this reproduction is dependent upon the quality of the copy submitted. Broken or indistinct print, colored or poor quality illustrations and photographs, print bleed-through, substandard margins, and improper alignment can adversely affect reproduction.

In the unlikely event that the author did not send a complete manuscript and there are missing pages, these will be noted. Also, if unauthorized copyright material had to be removed, a note will indicate the deletion.

UMI®

Thesis Approval

The Graduate College
University of Nevada, Las Vegas

April 28, 2009

The Thesis prepared by

Zohaib Parvaiz Rehmat

Entitled

Design of a "Figure-8" Spherical Motion Flapping Wing for Miniature

UAV's

is approved in partial fulfillment of the requirements for the degree of

Master of Science in Mechanical Engineering

_____
Examination Committee Co-Chair

_____
Examination Committee Chair

_____
Dean of the Graduate College

_____
Examination Committee Member

_____
Examination Committee Member

_____
Graduate College Faculty Representative

ii

ABSTRACT

Design of a "Figure – 8" Spherical Motion Flapping Wing for Miniature UAV's

by

Zohaib Parvaiz Rehmat

Dr. Mohamed B. Trabia, Examination Committee Co-Chair/Professor
Dr. Woosoon Yim, Examination Committee Co-Chair/Professor
Department of Mechanical Engineering
University of Nevada, Las Vegas

Hummingbirds and some insects exhibit a Figure-8 motion, which allows them to undergo variety of maneuvers including hovering. It is therefore desirable to have flapping wing miniature air vehicles (FWMAV) that can replicate this unique wing motion. In this research, a design of a flapping wing for FWMAV that can mimic Figure-8 motion using a spherical four bar mechanism is presented. To produce Figure-8 motion, the wing is attached to the coupler point of the spherical four bar mechanism and driven by a DC servo motor. For verification of the design, a prototype of the wing and mechanism is fabricated to determine whether the design objectives are met. Additionally, experimental testing is conducted to determine the feasibility of this design with the wing driven at speeds ranging from 2.5 to 12.25 Hz. To determine the aerodynamic coefficients the wing experiences during the Figure-8 cycle, wind tunnel experimentation is conducted. The results show good correlation between the model and experimental testing.

TABLE OF CONTENTS

LIST OF FIGURES

LIST OF TABLES

ACKNOWLEDGEMENTS

CHAPTER 1

INTRODUCTION

Unmanned Aerial Vehicle (UAV) design has shown an evolutionary trend during the

past quarter century stemming from the desire to reproduce what is seen in nature. The

exploration in UAV design began with the concept of recreating fixed wing flight at a

smaller scale since it was well understood. The concept of inducing flight by creating

thrust using a propeller or other mean and generating lift by the pressure difference

created by the free stream velocity provided a simplistic and practical UAV design.

Commonly used fixed wing UAV's provided a usable design for many military,

reconnaissance, and civilian applications. However, fixed wing UAV's provided no

design challenges and little enhancements to be made since maneuverability is limited at

most. The flight mechanics seen in nature, birds and insects, has proposed another

technique that can be utilized to enhance UAV design. Nature's flying animals use their

flapping wings to generate thrust and create lift with superior maneuverability and

mobility throughout flight.

Flapping wings flight can yield many benefits to UAV design. Recent advances in the

study of the biological understanding of bird and insect flapping wings has motivated

many researchers to recreate these many flapping motions in a mechanized form. In

essence, the versatility exhibited during flight by birds and insects has created a design

model for UAV design. The various distinctive flapping patterns provide researchers

many design options in accordance with the flight characteristics desired. Nevertheless, flapping wing unmanned air vehicles (FWMAV) can provide greater usage as they can travel about confined areas, hover, and easily modulate direction. These ideal characteristics have made many researchers dedicated in the design and modeling of FWMAVs.

The potential of FWMAVs seem promising; however, mimicking nature involves great difficulty and engineering challenges. Nature's unique flight patterns are complex and at a small scale. To replicate these flapping patterns, a thorough understanding of the motion pattern is required to design a precise mechanism. The wings must be carefully designed and fabricated to retain many of the characteristics present in bird and insect wings, i.e. light and flexible. The modeling of unsteady aerodynamic is another aspect that needs careful attention. Bird and insect flight is at low Reynolds number regime, thus overall aerodynamic forces may be very small. With all these considerations, FWMAV design requires extensive engineering and biological understanding for successful application.

In this research, we will present a bio-inspired wing mechanism design based on the flight pattern of hovering birds and insects, primarily the hummingbird. Hummingbirds and some insects outline a Figure-8 spherical motion trajectory enabling high maneuverability and hovering capabilities. Considering these characteristics, this wing motion provides desirable option for integration with FWMAVs. To produce Figure-8 spherical motion, a spherical four-bar mechanism was designed such that a wing attached to coupler point would outline the desire motion. Following the design and fabrication process, a setup is devised to conduct experimentation that would elucidate whether the

2

wing trajectory is achieved. A force signal will be measured with the wing in motion at increasing frequencies. The measured force signal will be used to predict the forces induced by this motion and serve as validation for the modeling of this motion. Additionally, an experimental approach using a subsonic wind tunnel is setup to determine the lift and drag associated with this flapping motion. This purpose of research was to determine a reasonable design for a Figure-8 spherical motion flapping using a unique design and conduct experimentation, determine the force model of the associated forces produces, and create a CFD model. This thesis will discuss the subtask of design and experimentation of a Figure-8 spherical motion flapping wing.

CHAPTER 2

LITERATURE REVIEW

2.1 Overview

Flapping Wing Miniature Air Vehicles (FWMAV) can offer potential abilities that stand unmatched compared to fixed wing flight. Nature's flying animals' exhibit mobility and maneuverability to travel about confined spaces, hover, and modulate direction with minimal effort and without loss of balance. These ideal behavioral aspects are desirable in the expansion of UAV design with the implementation of flapping wings that can recreate the motion seen in nature. Considering the exceptional benefits integration of flapping wings can offer to UAV design, researchers have tried to understand and quantify the flight aspects as exhibited in nature to begin the exploration of flapping wing UAVs. Researchers have also dedicated their time in producing a design that can replicate flapping patterns as seen in nature. In doing so, the biological foundation allowing bird and insect flapping wing flight must also be well understood.

2.2 Biological Flight Classification

Comprehension of flight seen in nature is needed in order to employ the same concepts in flapping wing designs. Flapping wings typically exhibit complex motion that simultaneously combines three angles: heaving (back and forth motion in the stroke plane), stroke (angle out of the stroke plane), and feathering (twist around the wing axis).

Many researchers studied various aspects of flapping wing motion of insects and birds. The following is a brief survey of the work presented which identifies certain aspects of flapping motion.

Ellington, [1], researched the flapping motion dynamics seen in nature. His work signifies that flapping motions can yield high lift and thrust values within low Reynolds number flight regimes. The minimal effect of inertial force contribution in this case maximizes the aerodynamics of flapping wing flight that provides the ability for various maneuvers as compared to fixed wing flight. Kinematic groups that pertain to the flapping patterns most commonly seen in nature are also outlined in this study. These patterns can be generally classified according to stroke planes. Stroke planes are conventionally defined as the plane to which wing stroke is confined. The three types of stroke planes identified are Horizontal Stroke Planes (hummingbirds and most insects), Inclined Stroke Planes (bats, passerine birds, and dragonflies), and Vertical Stroke Planes (butterflies). The flight uniqueness of each stroke plane is detailed in his work. Examples of the flapping patterns categorized by stroke planes can be seen in Figures 2.1 to 2.3.
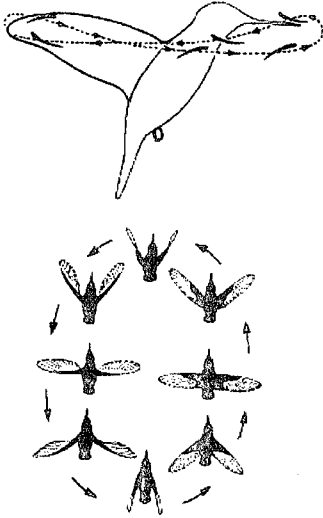
Figure 2.1   Horizontal Stroke Plane Wing Motion as seen in Hummingbirds, [1]
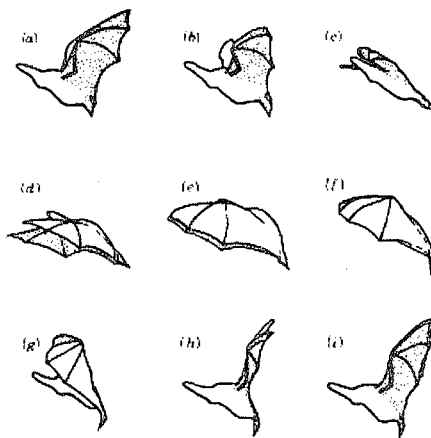
Figure 2.2   Inclined Stroke Plane Motion, i.e. Bats and Dragonflies, [1]
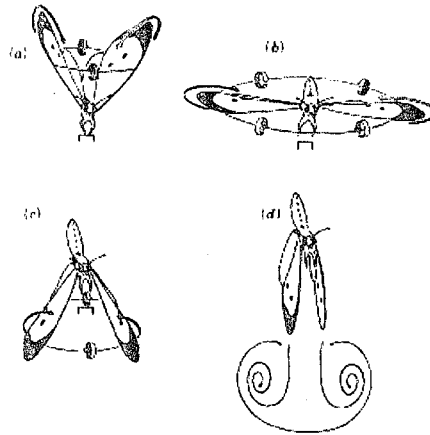
Figure 2.3   Vertical Stroke Plane Motion, Butterflies, [1]

The research by Shyy et al. [2] details the factors that affect scaling laws of biological and micro air vehicles such as wing span, wing loading, vehicle mass, cruising speed, flapping frequency, and power. Kinematics of flapping wings and an aerodynamic model for lift and drag forces associated with flapping motions are also presented. The research also enlightens on the ability of a hummingbirds to produce lift during both the up-stroke and down-stroke phases of its motion enabling it to hover. Figure 2.4 shows a hummingbird cycling through its flapping motion as it hovers.
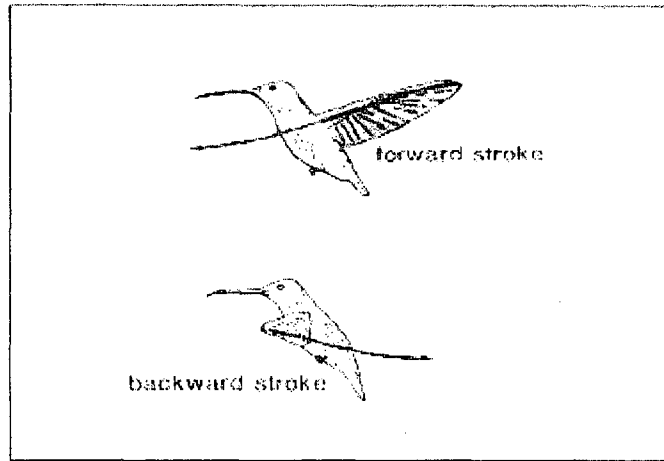
Figure 2.4   Lift Generation of a hummingbird while in hover is seen in up-stroke and down-strokes during both the forward and backward strokes of the flapping motion, [2]

For micro air vehicle design consideration, Ellington [3] presents insight on the ability of insects to produce high lift ratios by different techniques during the flapping motion cycle. The effects of wing frequencies and power demands as a function of the mass of the vehicle are presented. The paper concludes by outlining design challenges consisting of the mass, power, and maximum speed of insect-based micro air vehicles that would need to be resolved for successful autonomous designs. These design challenges will limit applicable FWMAV designs since the probability of achieving a balance of all three aspects is difficult. In nature, birds and insects have limited mass, require little power for flapping, and reach beat frequencies of up to 200 Hz, i.e. hummingbirds. Nonetheless, researchers seem undeterred as many design concepts are presented in hopes of creating succesful FWMAVs.

2.3 Bio-Inspired Flapping Wing Mechanical Concepts

The research available on the flight patterns of birds and insects has paved the way for research in the development of flapping wing miniature air vehicles with different mechanical concepts that attempt to reproduce what is seen in nature. The fascination of researchers with creating FWMAVs has yielded unique designs that accomplish various flapping wing motions. A summary of the mechanical design concepts introduced by many researchers are discussed.

To generate insect-like flapping motion, a planar four-bar mechanism is utilized by Zbikowski et al. [4]. The four-bar mechanism is designed to outline figure-of-eight wing path similar to many hovering insects. Figure 2.5 displays the configuration of the four bar mechanism used to generate the desired wing motion. A wing using a composite frame and Mylar membrane is a feasible option explored in the research. Using the mechanism concept and wing design, a prototype is fabricated to determine the forces induced at a wing beat frequency of up to 20 Hz and compared to those produced by unsteady aerodynamics. Similarly, Zbikowski et al. [5] presents the insect-like flapping kinematics of hover with a four-bar linkage and a spatial articulation. By re-configuring the coupler link, planar figure-of-eight motion is transformed into spherical Figure-8 motion at the wing tips. This design enhancement provided a more practical design since it creates more precise wing motion. Furthermore, Galinski and Zbikowski, [6], expand on their ongoing research by incorporating a spatial mechanism to improve their design. A spherical double Scotch yoke is integrating into the design to produce Figure-8 wing motion as a spherical Lissajous' curve. This design enhancement provides a smoother

9

spherical curve as compared to Figure-8 motion generated by the planar mechanism. The

complete mechanism with the addition of the double Scotch yoke is shown in Figure 2.6.
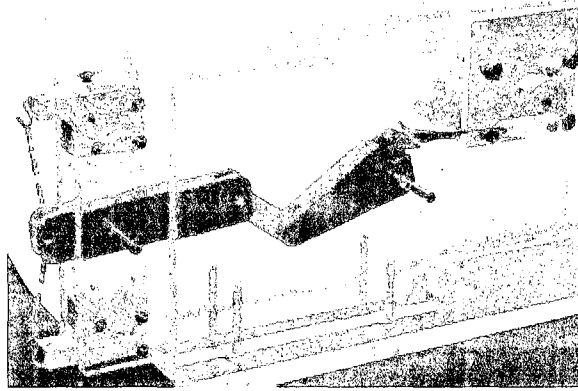
Figure 2.5   Planar Four-Bar Mechanism Used to Generate Figure-8 Motion, [4]
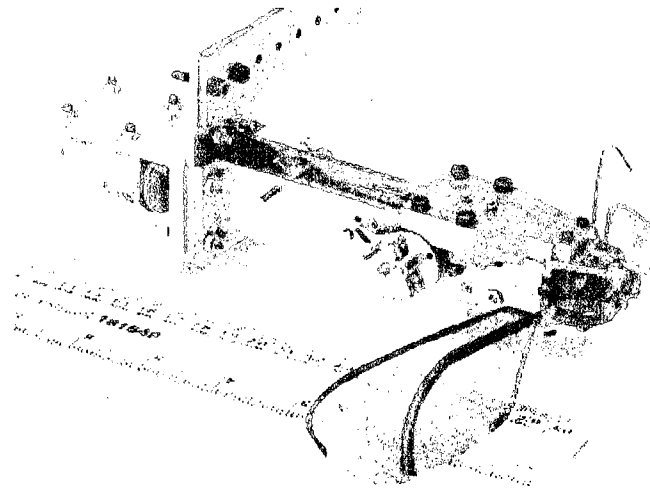
Figure 2.6   Prototype of FWMAV with double Scotch Yoke Spherical Mechanism

Which Produces Figure-8 Motion, [6]

Banala and Agrawal, [7], designed a single degree of freedom multipart mechanism

consisting of a five bar mechanism and an auxiliary four bar mechanism. The mechanism

is designed for out of the stroke plane flapping with time varying twist. The design was optimized by adjusting its parameters and comparing them to the kinematic flight data from a hawk moth. A prototype is fabricated, Figure 2.7, to verify the design objectives and test performance for future miniaturized application.
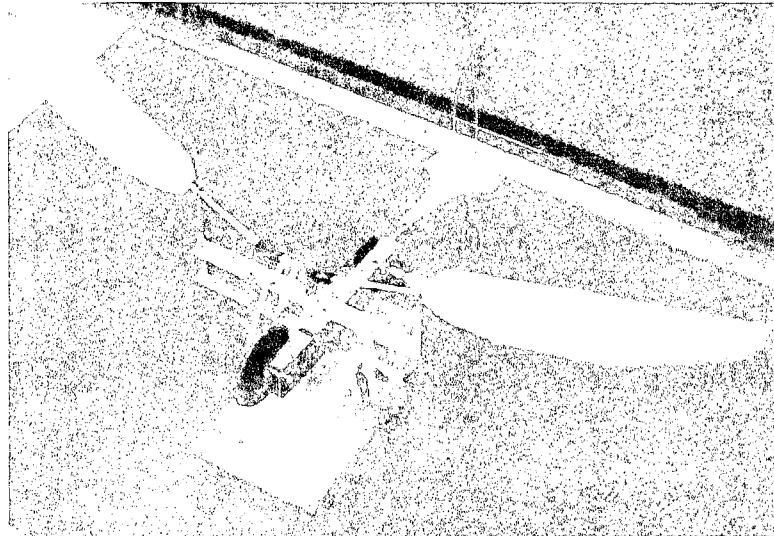
Figure 2.7   Prototype of FWMAV with Out-of-Stroke Plane Motion, [7]

A design for a flapping wing miniature air vehicle (FWMAV) capable of generating sufficient lift was developed by McIntosh et al. [8]. The design was inspired by the ability of a hummingbird to generate ample lift for hovering. The mechanism used generated in-plane stroke motion in addition to feathering using a spring-loaded cam follower system driven by a four bar mechanism. The mechanism is able to actuate two flapping wings using one motor and allows each wing to rotate about two orthogonal axes. The motion of the wing by the use of this mechanism is shown in Figure 2.8. Testing of this FWMAV prototype indicated that enough lift could potentially be generated to enable hover.

Feathered wing   *Fully pronated wing*
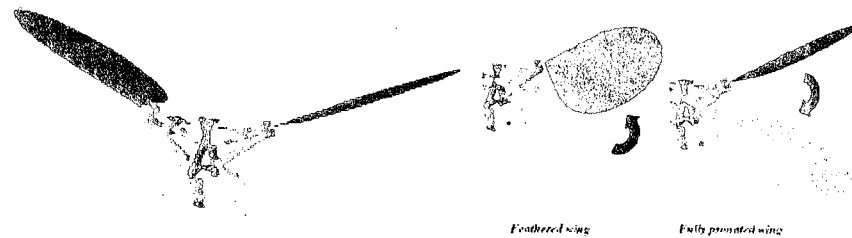
Figure 2.8   FWMAV Prototype with Mechanism Capable of Biaxial Rotation, [8]

Optimization of the flapping process was explored by Mandangopal et al. [9] by designing an energy storage mechanism that can be integrated into FWMAV designs. This design is based on the function of the insect thorax to store elastic potential energy for release in the subsequent stroke. The concept presented provides a technique to limit peak torque requirements of the drive motor of FWMAV prototypes.

Other ongoing research continues to present design ideas for FWMAV application. A novel micro air vehicle design with the objective of reproducing the unsteady aerodynamics of insect flight is presented by Conn et al., [10] and [11], using a parallel crank rocker mechanism. This mechanism discussed, PCR, allows for unconstrained motion as compared to other designs because of an integrated flapping and pitching motion output. The mechanism is designed such that a phase lag between two linkages can alter the wing angle of attack. By controlling the wing angle of attack, this mechanism allows for control of pitching facilitating greater maneuverability induced by adjusting the wing angle of attack and beat frequency as compared to other FWMAV wing mechanisms. Figure 2.9 shows the parallel crank rocker mechanism presented by the authors.
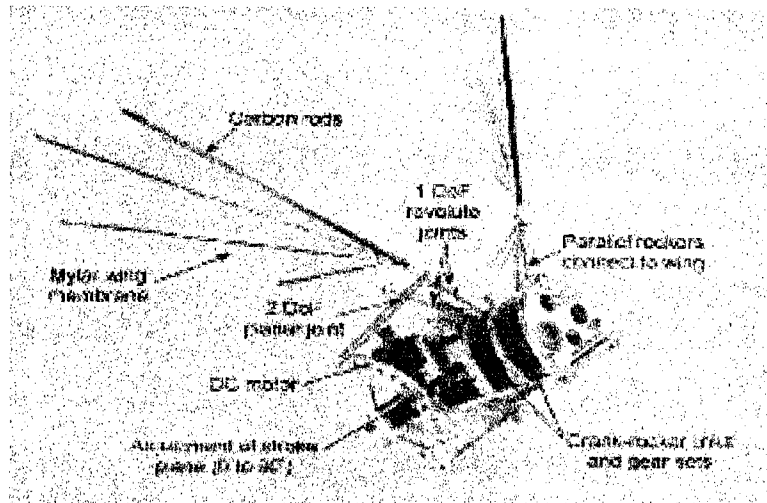
Figure 2.9   Parallel Crank-Rocker Flapping Mechanism, [10] and [11]

Khan and Agrawal, [12], recently proposed the design and optimization of a biologically inspired resonance-based flapping mechanism for flapping wing micro air vehicles. The design integrated three elements: aerodynamics, oscillator dynamics, and four-bar mechanism driven by an electric motor. For this design, the rotary motion is converted into oscillatory excitation through a four-bar mechanism. The design presented is to mimic elastic behavior of biological wings which allow for aerodynamic efficiency.

2.4 Flapping Wing Design Validation

The complexity of flapping wing assimilation into UAVs is also noticed in determining the flight characteristics of the flapping patterns that the design is made to accomplish. In order to create wing force models and model the aerodynamics of various flapping patterns, verification of flight characteristics using experimental analysis is often needed to determine certain unknown parameters and provide a justification tool for the model. As many researchers focused on various designs for flapping wing UAVs, other

researchers have primarily focused on experimental investigation and modeling of flapping wing UAVs to substantiate their abilities. An outline of experimental techniques used by researchers is detailed in this section.

2.4.1 Experimental Investigation Approach

Extensive experimental testing is conducted by researchers as a means of determining factors that can yield a FWMAV capable of mimicking a bird or insect. To comprehend how enough force is produced by insects, Dickenson et al., [13], did testing with a dynamically scaled wing model of a fruit fly, termed robotic fly. To simulate airflow around the wing, it is immersed in mineral oil with a load cell attached to the base and driven by a set of stepper motors for flapping in accordance with the actual flight pattern of a fruit fly, Figure 2.10. With this study, the authors presented the concept that flapping motion of insects is a function of three distinct and interactive mechanisms that generate lift at low Reynolds number flight. The translational stroke enables delayed stall by sweeping the air at large angles of attack and the production of aerodynamic forces occur during rotational circulation and wake capture as stroke reversing by quickly rotating and changing direction. The author also elaborates on the high maneuverability and hovering made possible by the two rotational mechanisms.
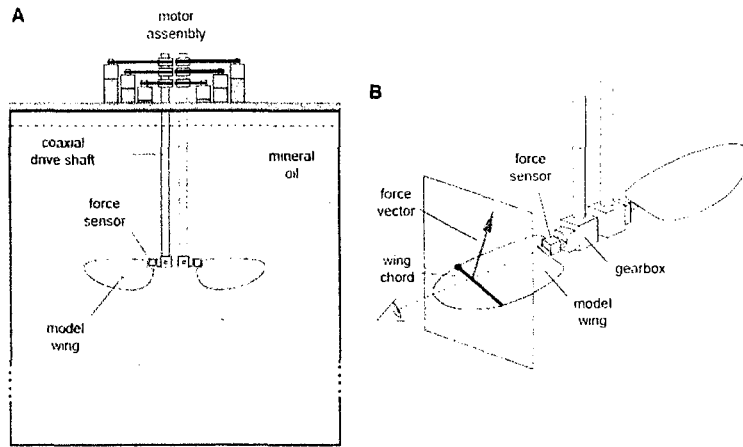
Figure 2.10 (A) Robotic Fly Immersed in 1 m x 1m x 2m tank of mineral oil, and (B)

close up view of robotic flapper, [13]

The aerodynamics force generated by wing rotation is examined Sane and Dickenson, [14]. An aerodynamic force signal is obtained by a steady translating wing which is rotated at constant angular velocities with results then incorporated into traditional, translational based models of insect flight. This study attempted to determine the aerodynamics force contribution associated simply with wing rotation. Incorporating the rotational effects into flapping wing models provides more precise modeling in turn assisting researchers in predicting the generated forces of flapping wings.

Considering the low Reynolds number flight regime and diminutive aerodynamic forces created by these flying animals, Singh et al., [15], wanted to determine the aerodynamic forces experimentally. To measure the thrust force generated by two insect-like wings mounted on flapping wing and pitching mechanism, the inertial loads were subtracted from a measured force signal to determine the aerodynamic contribution. An experimental technique to determine the thrust by both wings is employed. Since it was determined that inertial loads dominate low Reynolds number flight, the researcher's

attempted to filter the aerodynamic force contribution by testing their prototype in a vacuum chamber to determine the inertial loads. From these tests, the temporal variation of the aerodynamic forces was determined.

An experimental approach to analyze the aerodynamics of four-winged insects was presented by Maybury and Lehmann, [16]. The study included investigating the effect of changing the fore and hindwing stroke-phase relationship on the aerodynamic performance while hovering. This experimental investigation of the wing-wake and the effect of stroke-phase modulation on wake structure through the interaction of forces on the forewings and hindwings were conducted using a electromechanical dragonfly insect prototype. The aerodynamic performance of the prototype under various scenarios is documented in their work.

A generalized methodology for investigating the steady and unsteady aerodynamics of flapping wings using experimental techniques is presented Khan and Agrawal, [17]. Force coefficients are obtained from experimentation using a robotic flapper attached to a six-axis load cell for integration into a model. The robotic flapper is designed to give three degrees of freedom flapping motion consisting of the flap angle (flapping translational motion), feathering angle (rotation), and elevation angle (angle of the stroke plane). Figure 2.11 shows the robotic flapper used for this experimentation. This experimental technique was also used for modeling and simulation of a FWMAV based on the geometry hummingbirds or large insects by Khan and Agrawal, [18].
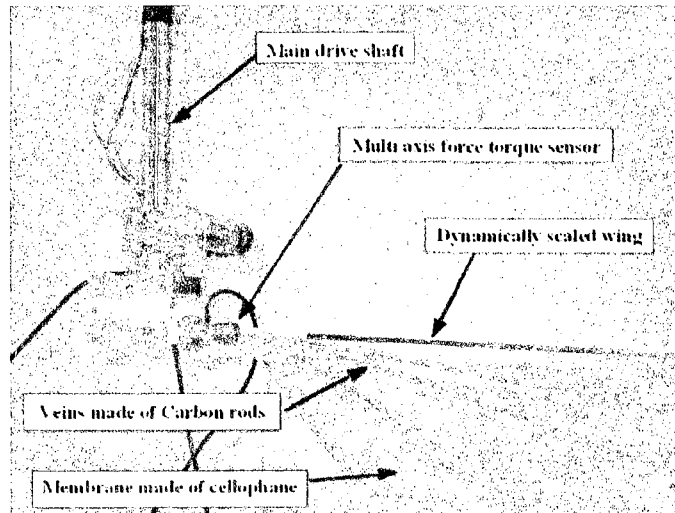
Figure 2.11   Robotic Flapper used for experimentation in [17] and [18]

In the research by Lehmann and Pick, [19], comparisons of the aerodynamic benefits

of various stroke strategies are established. Using a dynamically scaled two-wing

electromechanical flapping device, the forces and moments due to dorsal wing-wing

interaction, 'clap and fling', are analyzed. Seventeen different kinematic patterns are

tested to determine the aerodynamic performance of each. The determined aerodynamic

performance with respect to kinematic pattern is documented in their work.

In our study, experimental investigation will serve to validate the design of the

Figure-8 spherical motion and provide a measured force signal produced by this motion

for analysis. A discussion and brief introduction on the flapping mechanism of choice,

spherical four-bar mechanism, and relevant research that area is shared in the following

section.

2.5 Spherical Motion Approach

2.5.1 Spherical Four-Bar Mechanism for Flapping Wing Design

The creation of many mechanical concepts has been introduced for FWMAVs in order generate the flapping patterns exhibited in nature. Investigation techniques to validate designs and provide aerodynamic insight on the flight characteristics of flapping motions has also played in vital role in shaping FWMAV design. Applying the same methodology, an attempt to create a bio-inspired flapping wing using a spherical four-bar mechanism for miniature UAVs will be made. This mechanism is chosen because it most accurately replicates the function of a shoulder joint used by birds and insects to perform a variety flapping motions by their wings. Prior to constructing a spherical four-bar mechanism, an understanding of on the synthesis of spherical mechanisms is needed. The following is a brief outline of research on the synthesis of spherical four-bar mechanisms.

2.5.2 Spherical Four-Bar Mechanism Synthesis Review

Spherical four-Bar mechanisms generate coupler-curves about the sphere it is constrained to. The mechanism is capable of creating various coupler curves depending on the angular dimension assignment and configuration of each link. Ma and Angeles, [20], present a method for generating coupler-curves for spherical four-bar mechanisms. This method eliminates the need for linkage type classification, Grashof and non-Grashof, by unification of all types of linkages through a generalized methodology by using an index. It also eliminates the branching problem when solving the problem computationally. Lu and Hwang, [21], present three types of planar four-bar mechanisms with symmetrical coupler-curves with the equivalent spherical four-bar mechanism configuration. The number of design parameters and motion type for these spherical four-

18

bar linkages are indicated in their paper. The development of computer-aided design software for the design of spherical four-bar mechanisms is introduced by Ruth and McCarthy, [22]. The software designs spherical four-bar mechanism based on Burmester's theory. McCarthy and Bodduluri, [23], establish an approach for synthesizing a spherical four-bar mechanism to ensure that the result of a finite position synthesis does not have branching defects problem, which limit the usefulness of a linkage. A method for synthesis of function generating spherical four-bar mechanisms for five precision points was presented by Alizade and Kilit, [24]. The presented method includes introducing additional parameters that results in transforming the nonlinear equations into a set of fifteen linear equations. Triangular nomograms for symmetrical spherical non-Grashof double rockers generating symmetrical coupler curves are presented by Hwang and Chen, [25], to identify desired symmetrical coupler-curves. Four types of symmetrical spherical non-Grashof rocker-rocker mechanisms that trace symmetrical coupler curves are presented.

Using the concepts of spherical four-bar mechanism synthesis, the use of such a mechanism will be explored for designing a Figure-8 spherical motion flapping wing. The motion produced by a synthesized spherical four-bar mechanism will be discussed in detail in Chapter 3.

CHAPTER 3

SPHERICAL FOUR-BAR MECHANISM

3.1 Create Bio-Inspired Mechanism

The complexity of insect and bird flapping schemes poses design challenges that require proper analysis of the motion that any flapping wing design is to be based upon. Throughout the years, researchers have primarily focused on creating hinge joints to create flapping motion. However, this design seldom proves to be pertinent to many of nature's flying animals and limits the kinematics of that flapping pattern. Many birds and insects produce flapping motion that is concentrated around the shoulder joint which produces spherical motion. Spherical motion flapping allows them to produce various wing trajectories. This ability to create numerous wing paths may indicate the reason for immense maneuverability and mobility exhibited of these animals. Using this concept of spherical motion flapping, a superlative mechanism that can recreate these intricate flapping patterns would depict a more precise image of what is seen in nature. With this in mind, the idea of using a spherical four-bar mechanism to outline a desired wing trajectory provided a rational approach in replicating nature's flight capabilities. This mechanism would accomplish this task at ease and would mimic the function of a shoulder joint as many different trajectories could be achieved as well.

3.2 Mechanism Concept

Spherical four-bar mechanisms are spatial mechanisms that employ the same concept as planar four-bar mechanisms where the coupler traces the path determined by the configuration of the other links. Similar to a four-bar mechanism, the spherical four-bar mechanism consist of three moving links and one fixed link each apart of a great circle of a sphere with revolute joints connecting links at each end. The mechanism is driven by the input link which is connected to the fixed link (ground) at one end. The output link is connected to the other end of the fixed link (ground) and coupled to the input by a coupler link. The axis of the four joints must insect at the center of the sphere for accurate configuration and manipulation. As the input link is driven, spherical coupler-curves are drawn by the coupler link along its radial dimension. Coupler extensions can also be incorporated into the coupler link along any fixed orientation angle to generate any desired motion sought. A schematic of the spherical four-bar mechanism is shown in Figure 3.1. Table 3.1 lists the variables used to define the variable of spherical four-bar kinematics based on [26], which contains the fundamental equations based on spherical four-bar mechanism kinematics.
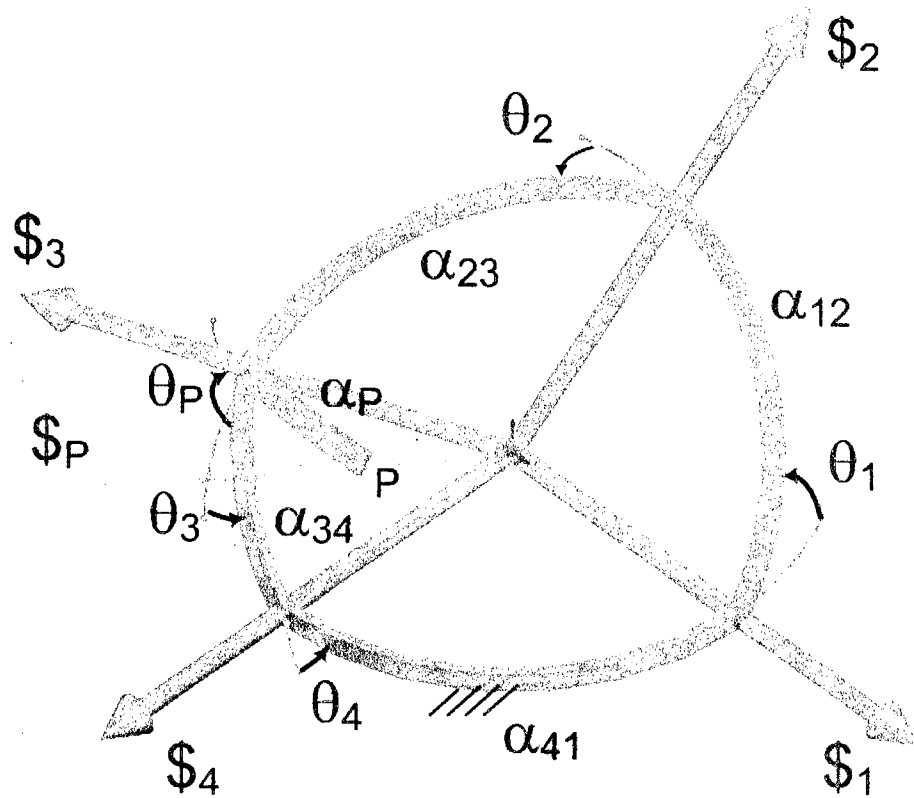
Figure 3.1   Spherical Four-Bar Mechanism

Table 3.1   Variables of Spherical Four-Bar Mechanism

Link	Link Dimensions	Link Variable
Fixed Link	α_{41}	θ_1 (output)
Output Link	α_{12}	θ_2
Coupler Link	α_{23}	θ_3
Input Link (Crank)	α_{34}	θ_4 (input)
Coupler Extension	α_P	θ_P (Coupler Orientation)

3.3 Synthesis of Figure-8 Wing Spherical Motion

With the idealistic flight characteristics of hummingbirds and some insects, Figure-8

spherical motion will be the desired wing trajectory the spherical four-bar mechanism

22

will be designed to accomplish. This motion is similar to what is exhibited by hummingbirds and some insects capable of high maneuverability and hovering. Figure 3.2 shows the desired wing trajectory the mechanism will be designed to trace. The motion can be achieved by attaching the wing to the coupler link of the mechanism where all links are connected by hinge joints. This symmetric Figure-8 requires two planes of symmetry; therefore, the spherical four-bar mechanism link dimensions and configuration must be defined accurately to outline the correct coupler path. A crank-rocker spherical mechanism will provide the suitable configuration to generate this motion.
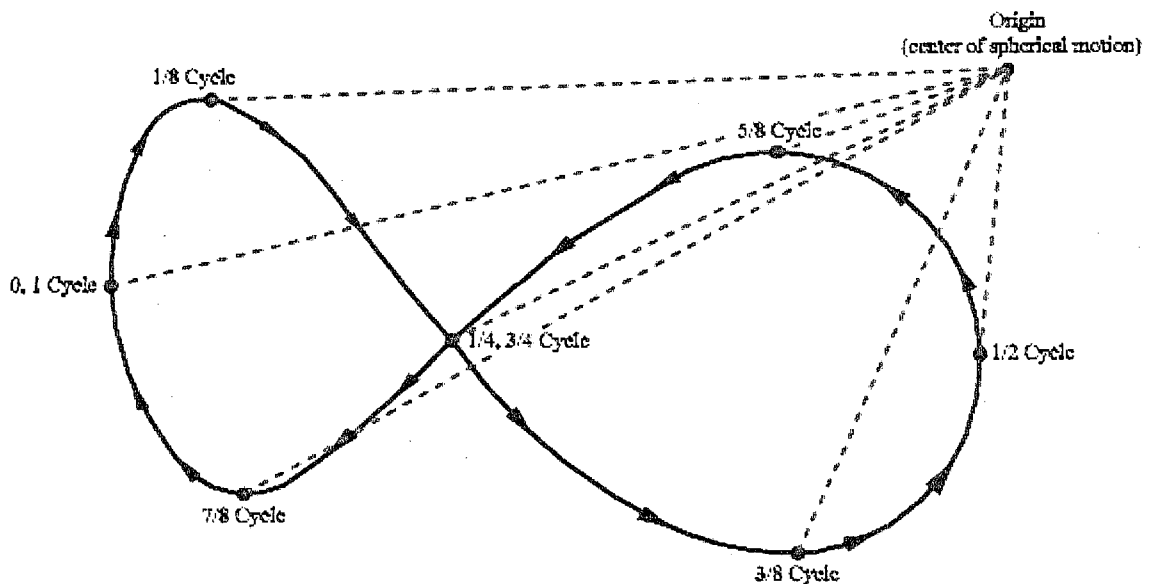
Figure 3.2   Wing Point Trajectory and Induced Velocity

3.3.1 Figure-8 Symmetry Conditions

Certain conditions are required to generate a Figure-8 coupler point curve with two planes of symmetry. The conditions are outline below.

23

- *Condition 1:* The mechanism should satisfy Grashof criterion noted in Equation 6.1, [27], to be classified as a crank-rocker four-bar mechanism.

$$s + l < p + q \tag{3.1}$$

The angular lengths of the shortest link, s, and longest link, l, must be less than the other two links. With this condition satisfied and the input as the shortest link, the input link will fully rotate and a crank-rocker spherical four-bar mechanism will be established.

- *Condition 2:* The coupler-curve must intersect only once throughout a complete cycle of the spherical four bar mechanism.

- *Condition 3:* The coupler-curve must be symmetric around two planes. The link angular dimension assignments must be assigned cautiously to verify whether the spherical mechanism is symmetric about the two planes.

- *Condition 4:* The assize of the curve is maximized.

The conditions noted above must be satisfied to outline the desire coupler-curve. Table 3.2 lists the angular dimensions that are assigned to each link to satisfy these conditions. The crank, input link, will be fully rotational as it will be driven by an electric motor. The orientation of the coupler extension, θ_P, will be fixed at -90° ($\theta_P = -90°$) from the coupler link. The angular dimension of the input link will be chosen at a later time depending the angular spacing of the coupler-curve preferred.

Table 3.2 Spherical Four-Bar Mechanism Link Angular Dimensions

Fixed Link α_{41}	Output Link α_{12}	Coupler Link α_{23}	Input Link α_{34}	Coupler Extension α_P
90°	90°	90°	$0 < \alpha_{34} < 90°$	90°

3.3.2 Motion Synthesis of Figure-8 Phases

The dimensions outlined create a symmetrical Figure-8 coupler-curve with a full rotation of input link, α_{34}. Four configurations of the spherical four-bar mechanism are identified utilizing the dimensions assigned for each link to produce the motion desired. Figures 3.3 to 3.6 show the configuration of the spherical four-bar mechanism at key positions that create Figure-8 coupler-curve and are explained in detail.
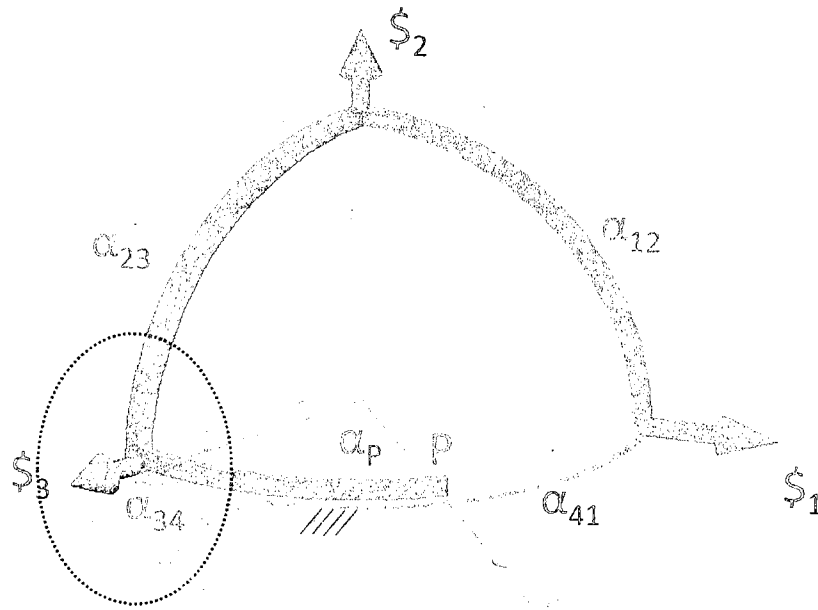
Figure 3.3   Spherical Four-Bar Mechanism, θ_4 is equal to $0°$

As shown in Figure 3.3, the mechanism forms a spherical right triangle with $\theta_4 = 0°$. Point P is in the $\$_1$ and $\$_4$ plane and is $\alpha_P - \alpha_{34}$ away from $\$_4$. The same orientation is held by α_{34} and α_P. The angle, θ_2, is equal to α_{34}, $\theta_2 = \alpha_{34}$, and $\theta_1 = \theta_3 = 0°$. This configuration of the spherical mechanism corresponds to the initial and ending position of the Figure-8 cycle as shown in Figure 3.2.

25
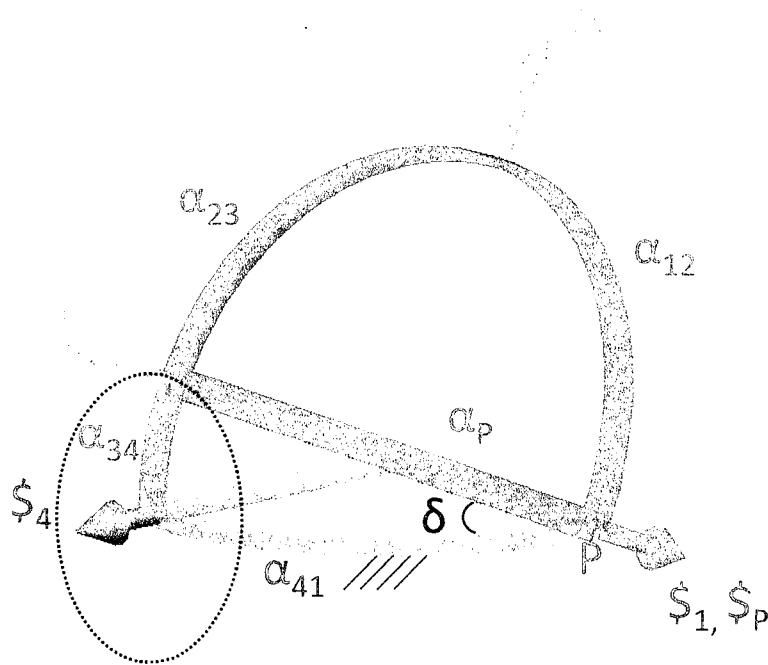
Figure 3.4   Spherical Four-Bar Mechanism, θ_4 is equal to 90°

When $\theta_4 = 90°$, point P is along $\$_1$ when $\theta_3 = 0°$ as shown in Figure 3.4. The angle, θ_1, is

equal to α_{34}, $\theta_1 = \alpha_{34}$, and $\theta_2 = 90°$. A spherical right triangle is formed by α_{34}, α_{41}, and α_P.

The orientation of P with respect to $\$_1$-$\$_4$ can be determined using law of cosines for

spherical triangles, [30], as indicated in Equations 3.2 and 3.3.

$$\cos(\delta) = \cos(\alpha_{34})\sin(90°) \hspace{5cm} (3.2)$$

$$\delta = \alpha_{34} \hspace{6cm} (3.3)$$

The angle δ is determined to be α_{34}, $\delta = \alpha_{34}$. This configuration of the spherical

mechanism corresponds to quarter-cycle position of the Figure-8 trajectory as shown in
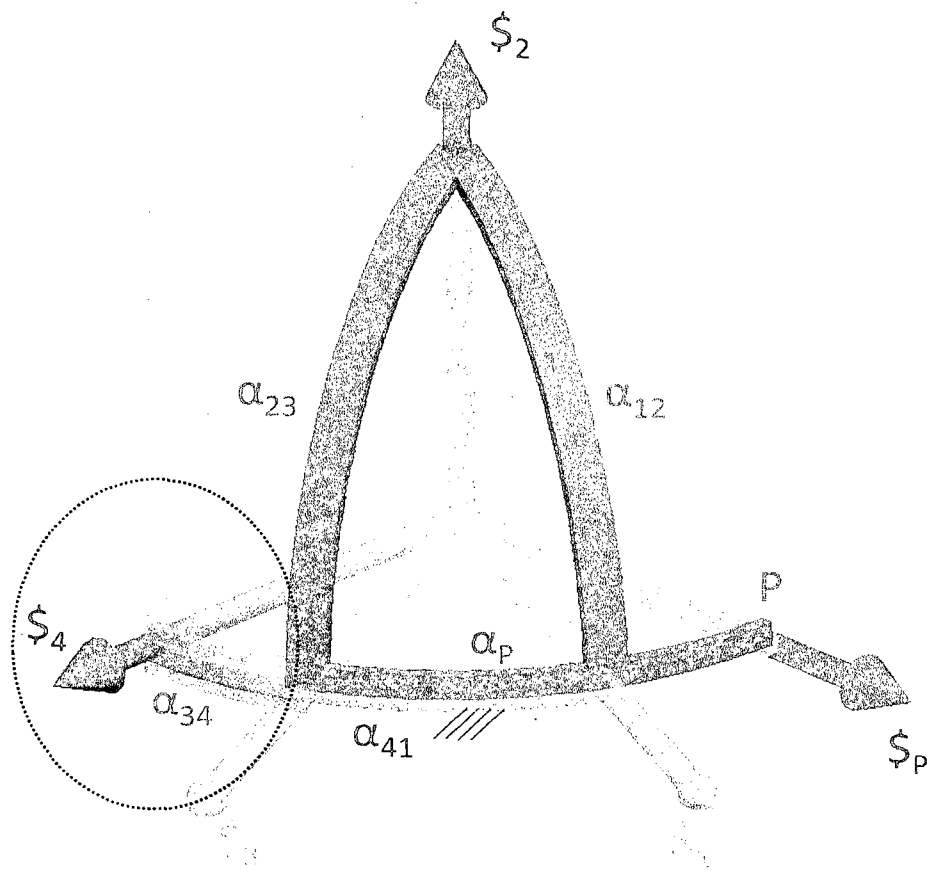
Figure 3.2

Figure 3.5   Spherical Four-Bar Mechanism, θ_4 is equal to 180°

The mechanism forms another spherical right triangle, Figure 3.5, when $\theta_4 = 180°$; therefore, point P is in the $\$_1$-$\$_4$ plane and $\alpha_P + \alpha_{34}$ away from $\$_4$. The same orientation is held by α_{34} and α_P. The angles formed are $\theta_1 = 90°$, $\theta_3 = 90°$, and $\theta_2 = 90° + \alpha_{34}$. This configuration corresponds to half-cycle position of the Figure-8 trajectory as shown in Figure 3.2.

Figure 3.6   Spherical Four-Bar Mechanism, θ_4 is equal to 270°

When the $\theta_4 = 270°$, point P is along $\$_1$ when $\theta_3 = 180°$ as shown in Figure 3.6. The angle, θ_1, is equal to α_{34} plus 90°, $\theta_1 = \alpha_{34} + 90°$, and $\theta_2 = 90°$ and $\theta_4 = 270°$. A spherical right triangle is formed by α_{34}, α_{41}, and α_P. The orientation of P with respect to $\$_1$-$\$_4$ can be determined using law of cosines for spherical triangles, as indicated in earlier in

28

Equations 3.2 and 3.3, $\delta = \alpha_{34}$. This configuration of the spherical mechanism corresponds to three-quarter cycle position of the Figure-8 trajectory as indicated in Figure 3.2.

3.4 Resulting Figure-8 Spherical Motion

The resulting coupler-curve is symmetric around the plane of fixed link and the center of the sphere. The curve is spaced α_{34} degrees from either side of $\$_1$. At these two extremities, α_P is oriented with the $\$_1$-$\$_4$ plane. Its orientation at the middle of the Figure-8 is equal to α_{34}. Figure 3.7 shows the motion of the four-bar mechanism and the path of the coupler point. By attaching the wing to point P with the same orientation of α_P, Figure-8 motion of the wing can be achieved as can be seen in Figure 3.8. The equations of motion of spherical mechanism are based on [26] and are listed in Appendix A. A value of 45° is chosen for α_{34}, which results in 90° angular spacing of the wing motion.
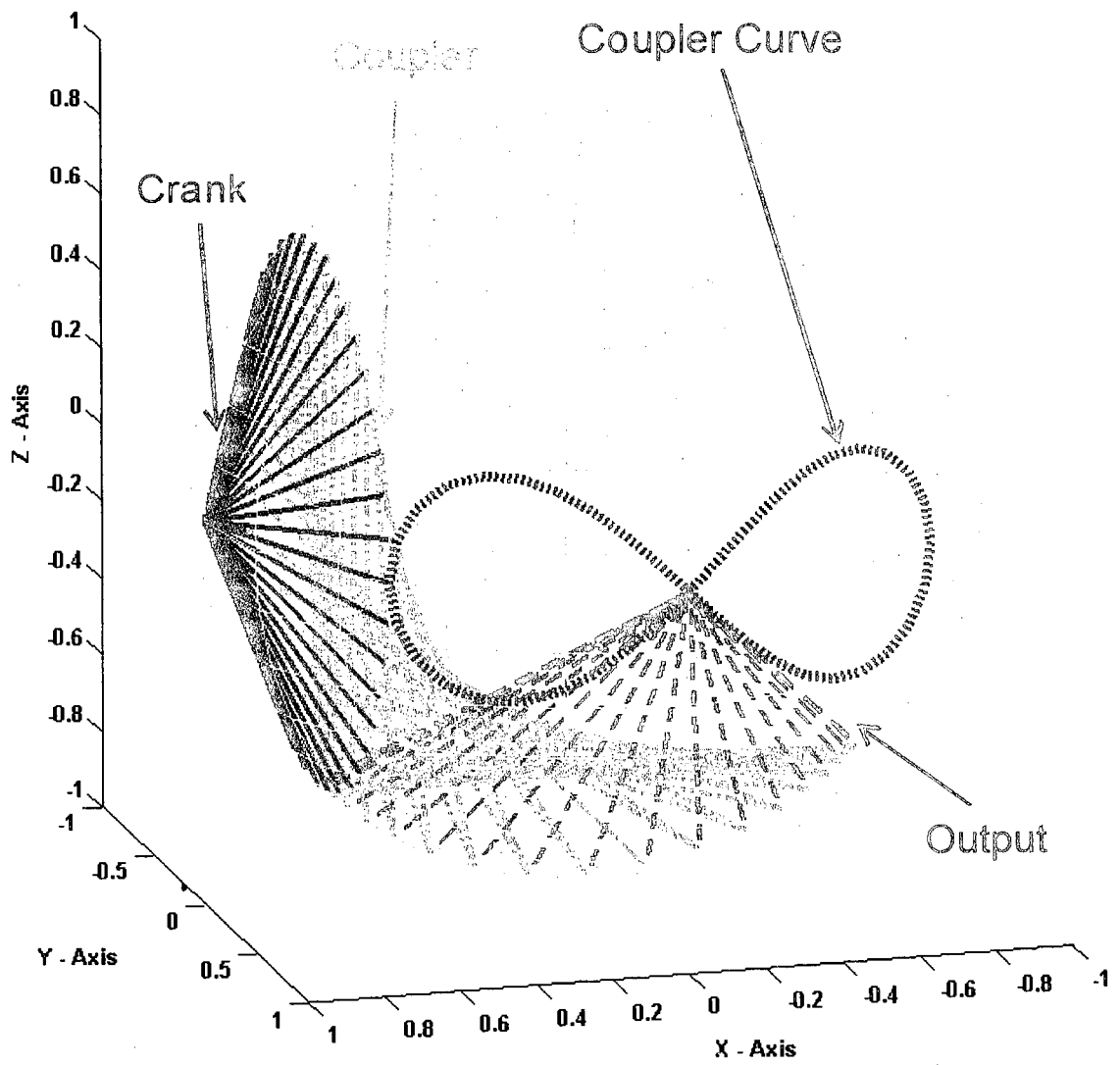
Figure 3.7   Motion of the Spherical Four-Bar Mechanism
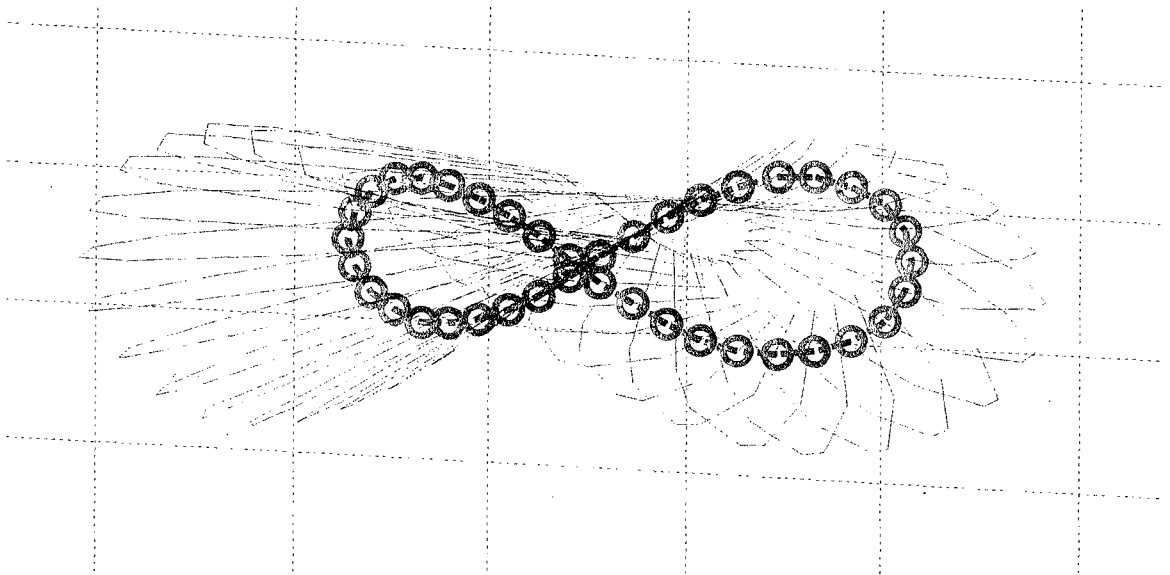
Figure 3.8   Wing Trajectory with Center of Gravity

CHAPTER 4

MECHANICAL DESIGN PROCESS

4.1 Objective

With the established idea of creating a wing mechanism using a spherical four-bar mechanism, the design and fabrication of the mechanism and wing must now be accomplished. This process begins with first identifying the requirements of the mechanism and wing for testing purposes. Requirements such as the weight, size, and flapping frequency must all be taken into account prior to any design. The design process will then begin with first designing a spherical four-bar mechanism and wing that can accomplish the required tasks. After determining the design's feasibility, the fabrication process will then enable us to construct the mechanism, wing and any other essential components to determine its practicability with testing.

4.2 Design Requirements

In order to design our wing prototype, an ideal approach would integrate weight and size limitations to determine how the design will be fashioned. The intended design purpose of the wing prototype is to utilize it for miniature unmanned air vehicles, thereby restricting it to reasonable compact space, nearly 18 − 24 cm square area with minimal weight is preferred. This will allow for it to be utilized as is in terms of weight and size, rather than optimized at a later stage. Flapping frequency must also be considered when

determining the size and weight of the wing prototype. Hummingbirds and insects flap their wings at very high frequency of 100 – 200 Hz and a design consisting of sustainable components for higher flapping frequency can further relieve enhancements that may need to be made throughout the testing process.

4.2.1 Size Requirement

As mentioned, the application of the wing prototype is for use in conceptual flapping wing miniature air vehicles (FWMAV) that are capable of high maneuverability, i.e. hover. The design is be based on the flapping of hummingbirds and small insects, hence needed to be compact in size to roughly about 18 – 24 square centimeters as mentioned. Considering this, the spherical four-bar mechanism would be design to occupy a sphere of approximately 7 – 8 cm in diameter and the wing would be designed to be about 12 – 14 long and 4 cm wide. In accordance with the size requirement noted, the actual size of the wing prototype will be determined during the design process.

4.2.2 Weight Requirement

The unknown flight characteristics that will verify the capability of using this design for practical application provides little information to help determine the weight requirements for this prototype. It would be best to limit weight as best as possible to increase the potential of producing enough residual net force, lift, that will allow the prototype to free itself from the ground and minimize power requirements to drive the mechanism and wing. Therefore, the spherical four-bar mechanism links should all have limited mass in terms of design optimization rather than material use. Ideal mass for the mechanism would be approximately 60 – 70 grams. The wing should also be limited in mass, about 5 – 7 grams, and not made of metal, but other material that will reduce

fabrication time. The minimal mass of the links and wing can further permit us to choose a lighter motor that is capable of driving the finished prototype and load cell to limit the overall mass of the prototype.

4.2.3 Flapping Frequency Requirement

The flapping wings of hummingbirds and insects yield unmatched flight ability, thus provokes the idea presented in this thesis. However, the frequency at which they flap their wings, approximately 100 – 200 Hz, complicates the design process. This frequency range seen in nature is very difficult to replicate and requires a perfected design that can recreate the motion initially. The spherical four-bar mechanism design that is proposed for our prototype will be conceptual and will attempt to verify the wing motion and flight characteristics. The design of this prototype, mechanism and wing, will seek to accomplish testing frequencies starting at 2.5 Hz and reaching the highest frequency attainable. The inertia driven by the motor will play a vital role in determining the maximum frequency reached, so limiting the mass of the mechanism and wing will be an essential guideline during the design process.

4.3 Spherical Four-Bar Mechanism Design

4.3.1 Design

Designing a spherical four-bar mechanism requires careful attention as compared to planar mechanisms as they reckon to be more challenging. The proper function of a spherical four-bar mechanism is dependent on many key issues that must be considered during the design and fabrication process. First, spherical four-bar mechanism links must be designed to avoid any interference amongst all links. All the links cannot occupy

space on the same greater sphere; otherwise they are bound to interfere. Second, in connecting all links there must be sufficient clearance between each link to allow unobstructed motion. Lastly, the four axes associated with the joints must intersect at the center of the sphere or at the same point. If these links do not have a common center point, the mechanism will lose its mobility by not be able to perform the required task.

To avoid these issues, we begin designing the spherical four-bar mechanism with each link occupying a space between two concentric spheres within the overall mechanism sphere. Additionally, spacers are used to between link connections and occupy space within a sphere similar to the mechanism links. These spacers allow for unobstructed motion of the mechanism and limit wear associated with continuous motion. Table 4.1 displays the inner and outer concentric spherical radii of each link and Figure 4.1 shows the space each link occupies within the mechanism sphere.

All of the spherical four-bar mechanism links are designed to maintain weight balance with minimal mass to provide smooth transmission of the mechanism. Weight balance is achieved by elongating the crank and output link by 15° and 30° respectively from the fixed link end. Mass optimization of the coupler and output is accomplished by reducing the outer ends of both links enough to maintain a balance between mass and structural stiffness. A base to hold the motor is designed to occupy the space of the fixed link. The coupler is designed as one piece and occupies the outermost sphere to allow unobstructed wing motion. Each link is designed to have flat surfaces instead of radial surfaces, feet, for easier connection, [31]. The proposed design of the spherical four-bar mechanism is shown in Figure 4.2. The hinge joints of the crank and output link indicate the connection to the base instead of a fixed link. Also seen in the Figure, the crank and

output links are placed on the same sphere as the chosen dimensions ensure that they do

interfere.

Table 4.1   Mechanism Links Concentric Spherical Radii

Link	Inner Radius	Outer Radius
Fixed Link	-	24 mm
Output Link	25 mm	30 mm
Crank	25 mm	30 mm
Coupler Link	31mm	36 mm
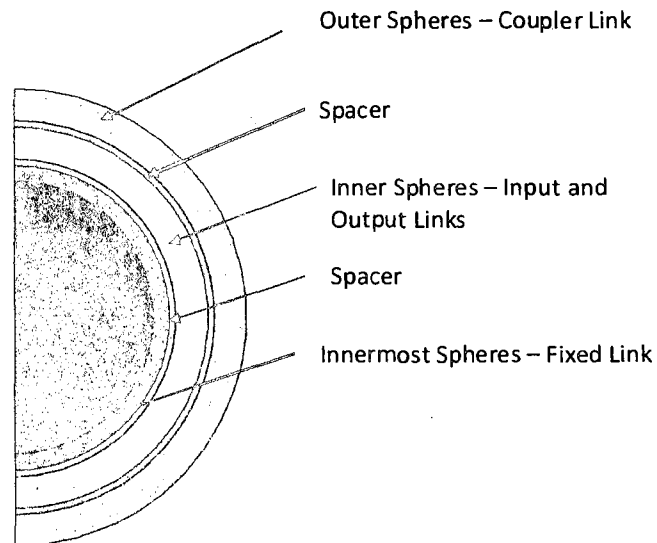
Figure 4.1   Location of Each Mechanism Link amongst the Greater Sphere
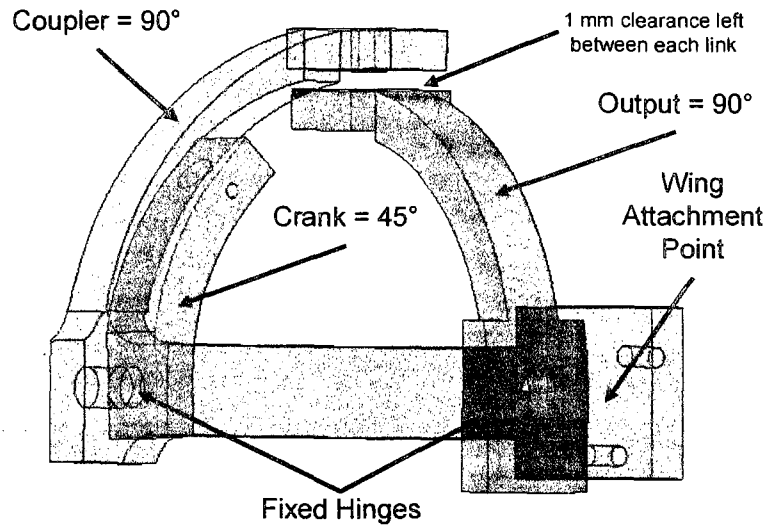
Figure 4.2 Proposed Conceptual Design of Spherical Four-Bar Mechanism

4.3.1 Fabrication

The conceptual nature of the spherical mechanism prototype did not restrict us to choose a particular metal in order to limit weight and increase strength. Utilizing metal instead of creating ABS plastic parts with a rapid prototyping machine would provide better insight on mechanism's feasibility in exploring potential flapping wing UAV application. Therefore, the links of mechanism were machined using high strength Aluminum, 7075, to provide a combination of limited mass and structural stiffness. Aluminum is an easier metal to machine and is readily available. For easier connection between all links, they are machined to have flat surfaces on both ends of the hinge locations. The coupler link is machined as one piece with filleted edges where the coupler-extension extends from the coupler link. Three counter bore holes are machined in the base to so that it may be attached to a testing platform. Figure 4.3 shows the actual machined links used for the prototype of the spherical mechanism and Table 4.2 lists the

mass of each link and base. The design and fabrication of these links is accomplished with careful inspection to limit any complications with prototype testing that would necessitate a re-design of any link.
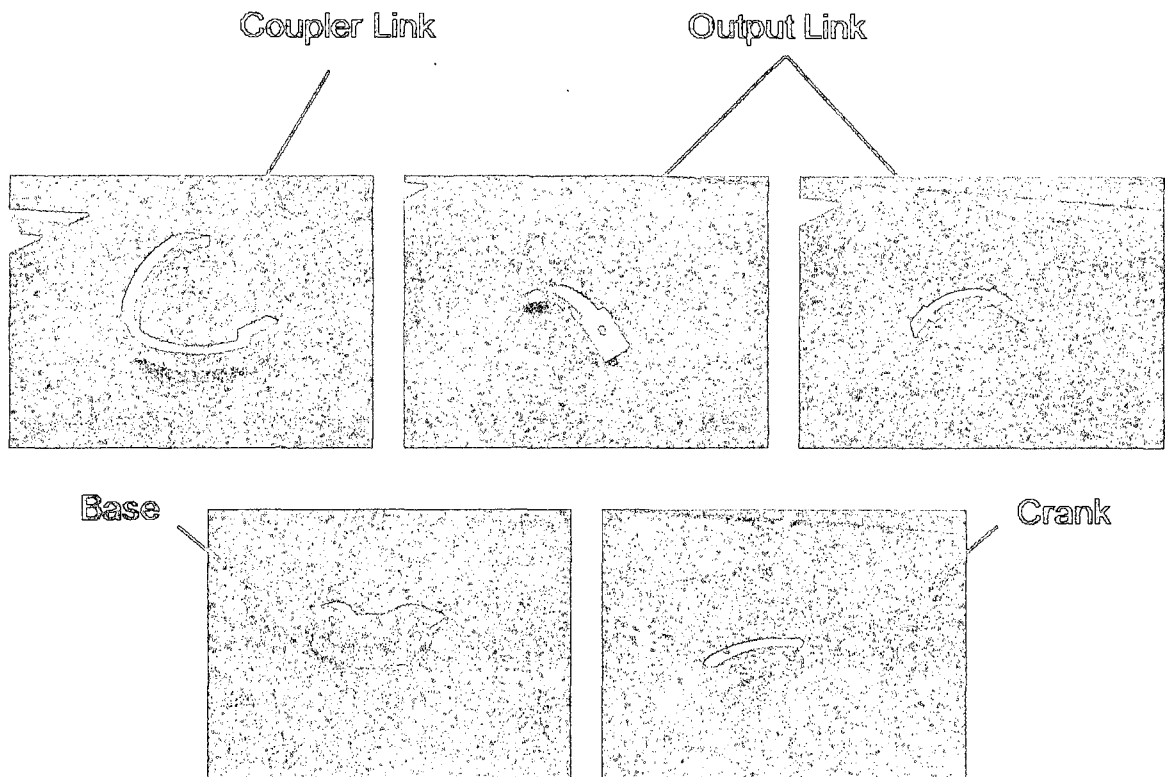
Figure 4.3   Machined Links Used to Construct Spherical Four-Bar Mechanism

Table 4.2   Mass of Links and Assembly Components for Mechanism

Part	Mass (g)
Crank	4.60
Output	5.81
Coupler	15.15
Base	31.00
Brass Sleeve	0.11
Aluminum Washer	0.13
Steel Rivet	0.62
Teflon Ring	0.15

4.4. Wing

4.4.1 Design

The ability of the wing prototype to mimic what is seen in nature, i.e. hummingbirds and insects, made it essential to implement a wing design that is bio-inspired as well. As mentioned earlier, it is desirable to have a wing approximately 12 – 14 cm long and 4 cm wide. Additionally, a load cell would be attached to the base of this wing, so a coupler piece would need to be designed to attach both components. Reviewing selected papers that employed bio-inspired wings, a scaled prototype of a dragonfly forewing, [16], was designed. The wing retained similar shape and had a tapered thickness from wing base, 4 mm, to wing tip, 1 mm, to maintain balance between limited mass and stiffness. Figure 4.4 shows the dragonfly forewing and the proposed wing design.

(A)   (B)
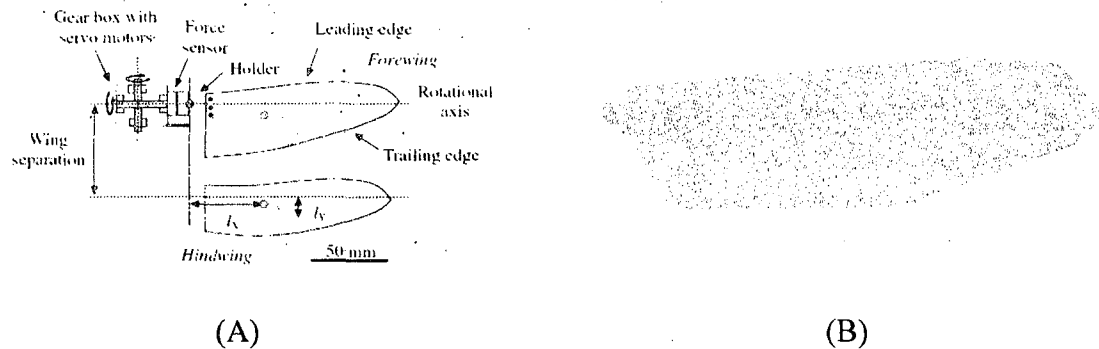
Figure 4.4   (A) Dragonfly forewing used in [16] . (B) Proposed Wing Design for

Prototype and Testing

4.4.2 Fabrication

Mass of our wing was an essential factor that played into the fabrication process. Initially it was decided to have the wing created using the rapid prototype machine with ABS plastic. The wing was designed to have cut outs to reduce mass and look similar to a wing membrane as seen in nature and covered with two Mylar sheets on both ends. However, the significant mass of this configuration of 9 grams would increase power required to drive the wing prototype and increase inertial forces acting on the load cell. The idea of using model grade balsa wood was then investigated to minimize mass. A wing was cut from a 3/16 inch thick sheet of model grade balsa and sanded on both ends for a tapered thickness similar to the conceptual design with a mass of 2 grams. It was reinforced at the shoulder where it would be attached to the wing coupler with three alternating layers of unidirectional carbon fiber. An ABS plastic coupler was printed using a rapid prototyping machine for wing and load cell attachment. Figure 4.5 is a top view drawing of the wing outlining the dimensions and center of gravity, which is located 60.4 mm from the edge of the adapter and 20.3 mm from bottom lower edge of wing. The total mass of the wings with all components is 3.2 grams.
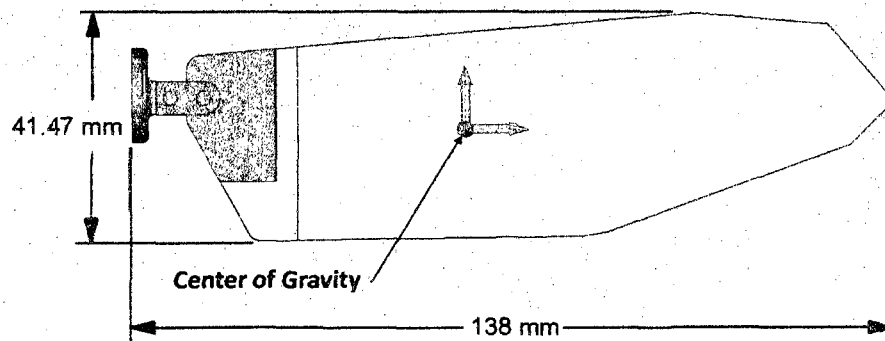
Figure 4.5   Wing Top View

4.5 Prototype

The final stage of the design and fabrication process provided the most complexity as putting together a working wing prototype required careful and proper attachment of all components. The spherical four-bar mechanism demanded significant attention in making sure all links would stay in place, provided adequate testing times, and prototype longevity. This iterative process leads through various ways of making sure a working prototype was attained. The use of pins, combination of shoulder screws and plastic nuts with nylon inserts, and aluminum rivets, were options that were tried in an attempt to make the mechanism yield the results needed. For the final prototype, steel rivets are used as pins to connect all the links of the mechanisms. To avoid wear and reduce friction, each link joint is fitted with brass sleeves and then Teflon rings are placed between the rivet head and link surface. Washers are used as spacers to separate links at hinge locations and reduce friction as well. Figure 4.6 shows the assembled spherical four-bar mechanism. As shown, a set crew is used to ensure that the motor shaft remains attached to the crank and three screws hold it to the base.

Steel Rivets, Brass Sleeves, Washers, & Teflon Rings at all Joints

Conceptual Model of Spherical Mechanism

Set Screw for Motor

Actual Prototype of Spherical Mechanism
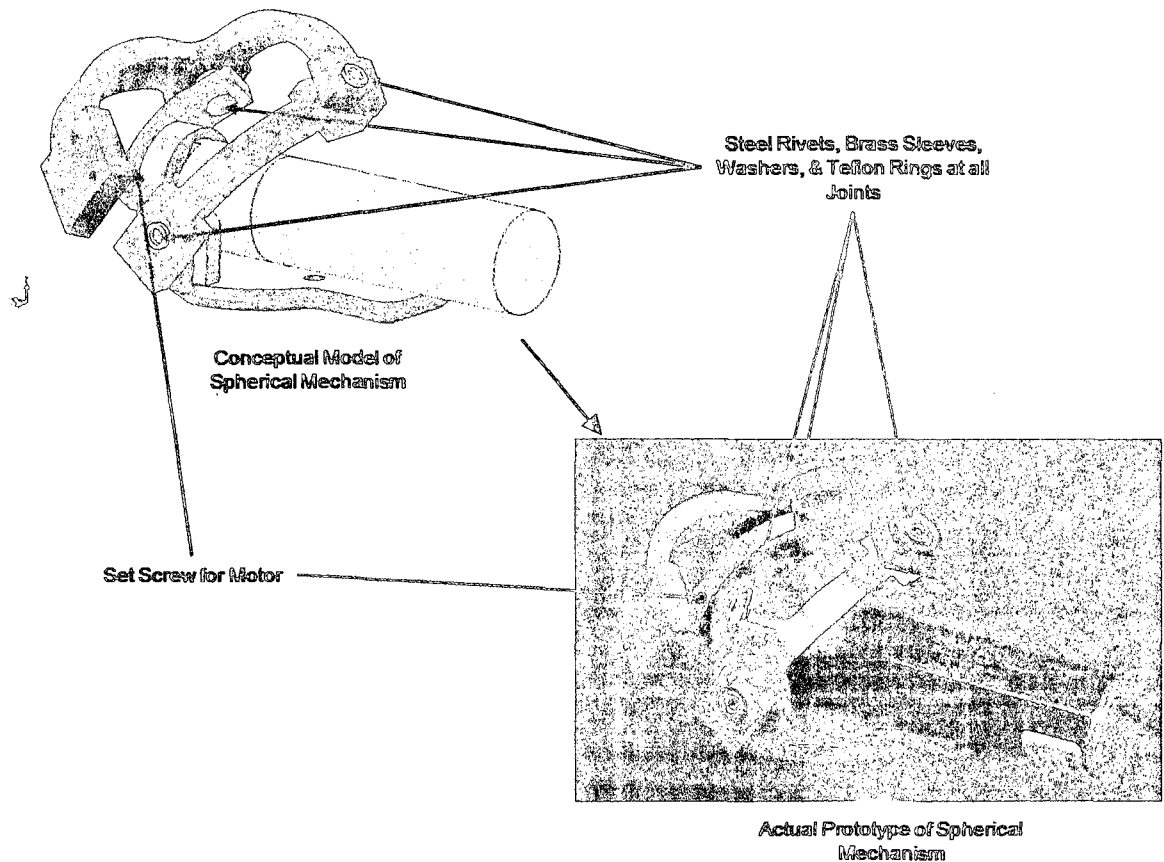
Figure 4.6   Conceptual and Actual Prototype of Spherical Four-Bar Mechanism

For the wing, the plastic wing coupler is attached to the wing shoulder using high strength epoxy. Three screws applied from both mechanism coupler and wing coupler ends to the tooling and mounting ends respectively to hold the ATI Nano 17 load cell, [32]. Figure 4.7 displays and identifies the components of the wing coupler assembly. Figure 4.8 and 4.9 show a drawing and a photo of the assembled Figure-8 Spherical Four–Bar mechanism wing prototype respectively.
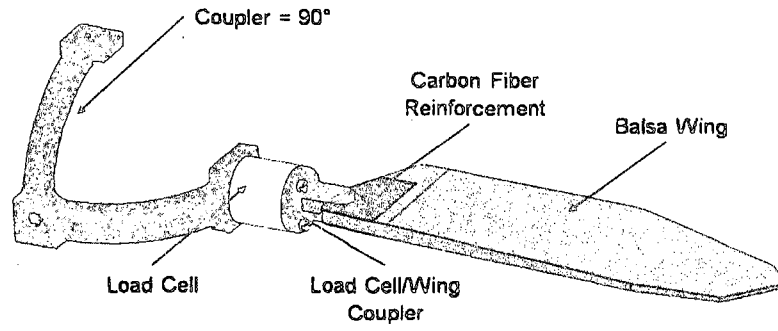
Figure 4.7   Wing Design for the FWMAV Prototype
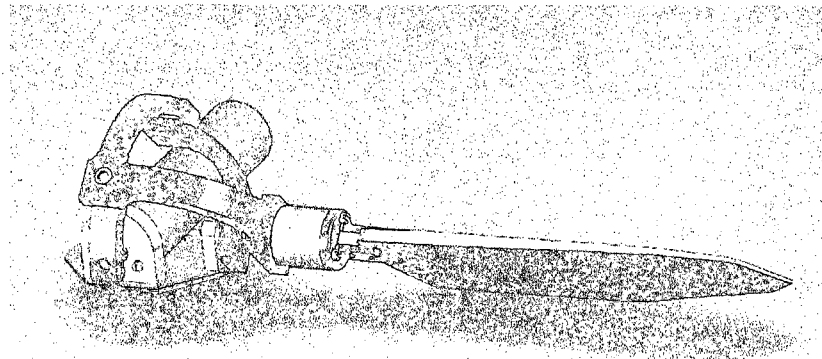
Figure 4.8   Figure-8 Spherical Four Bar Mechanism

Figure 4.9   Prototype of the Figure-8 Spherical Four Bar Mechanism

CHAPTER 5

PROTOTYPE TESTING

5.1 Objective

Wing trajectory is essentially the basis of this design process and must be verified to determine the mechanism's feasibility. To conduct experimentation for design validation, prototype testing is conducted to validate to wing motion and generate force signals that are produced at various flapping frequencies.

5.2 Prototype Test Stand/Platform

Proper placement was vital in achieving unobstructed motion of our wing prototype. In essence, a platform was needed to which we could attach our spherical four bar mechanism and conduct experimentation. The platform was designed using a quarter inch aluminum rod threaded into a three square inch aluminum plate. This aluminum plate was then attached to a larger aluminum base to hold the rod and smaller plate in position and placed onto a table. To decouple the table and prototype platform, rubber silicone pads were glued to the bottom surface corners of the large aluminum base plate to minimize any vibration associated with ambient disturbances present in the laboratory. Additionally, an aluminum column was placed over the rod to mitigate vibration produced by the flapping wing. To attach the base of the wing prototype, a threaded aluminum coupler piece was attached to the top end of the rod. The base of the UAV

prototype was secured using three screws to the coupler piece. Figure 5.1 shows the test stand platform as described. With this setup, the prototype will sit 42 cm above the main aluminum base.
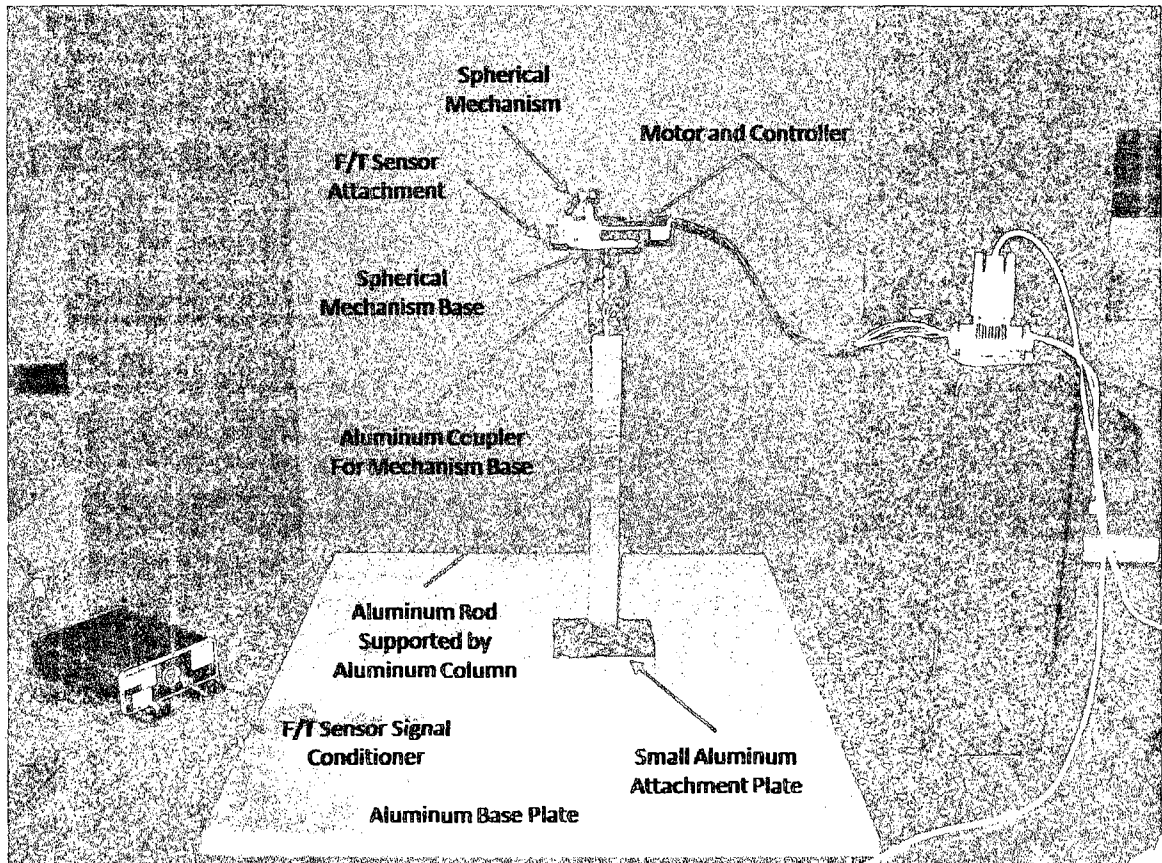
Figure 5.1   Wing Prototype Test Stand

5.3 Apparatus/Hardware

Successful experimentation of our wing prototype required proper hardware and apparatus to establish whether the wing motion could be achieved and identify the forces it produced. To drive the spherical four bar mechanism, a motor with sufficient power output was selected. Prior to the selection process, torque, power, and size requirements

were identified to understand what type of motor and its power output would be needed. The mechanism would be driven at lower to higher speeds; therefore, a sensor capable of detecting very small forces, around 0.5 – 4 N, with a reasonable resolution would provide the best results. The ATI-IA Nano 17 F/T load cell, [32], provided the best option with its compact size an ability to resolve down to 0.319 grams. A detailed description of both components is provided.

5.3.1 Six-Axis F/T Load Cell

Visualization of the forces and moments induced by the Figure-8 motion was possibly only with a Force/Torque load cell that was capable of generating the experimental force and moment signal. ATI-IA Nano 17 Force-Torque load cell, [32], is a six axis transducer with varied range depending on the calibration assignment. The load cell has a high signal to noise ratio with the use of silicon strain gages rather than conventional foil gages providing stronger signal. For our application, two calibrations were used which allowed measurement of up to 17 N and 35 N in the axial direction of the sensor, F_z, with fine resolution as low as 1/320 N. Table 5.1 list the maximum allowable force per direction and resolution with regard to the calibration. The sensor will be attached to the base of the wing to eliminate the need for force transformation.

Table 5.1   ATI-IA Nano 17 Load Cell Calibrations

Force Direction	Calibration I (FT7863, FT8964)		Calibration II (FT7862,FT8963)	
	Maximum Force/Torque	Resolution	Maximum Force/Torque	Resolution
F_x	25 N	1/160 N	12 N	1/320 N
F_y	25 N	1/160 N	12 N	1/320 N
F_z	35 N	1/160 N	17 N	1/320 N
M_x	250 N-mm	1/32 N	120 N-mm	1/64 N
M_y	250 N-mm	1/32 N	120 N-mm	1/64 N
M_z	250 N-mm	1/32 N	120 N-mm	1/64 N

For data acquisition, the ATI Nano 17 requires a NI-DAQ PCI board that is connected to the signal conditioner. It is connected to the signal conditioner interface and data is collected using a LabVIEW virtual instrumentation file that has been pre-programmed to accept the sensor outputs. The user is required to select a calibration, DAQ PCI device number, and determine if static forces applied are to be zeroed prior to any testing. Data files are generated by LabVIEW as plain text and can be can be converted to any compatible file for data analysis. Data is sampled at a default 10 kHz, but can be sampled at lower frequencies if needed. Figure 5.2 shows a screenshot of the actual LabVIEW virtual instrumentation and outlines the features described.
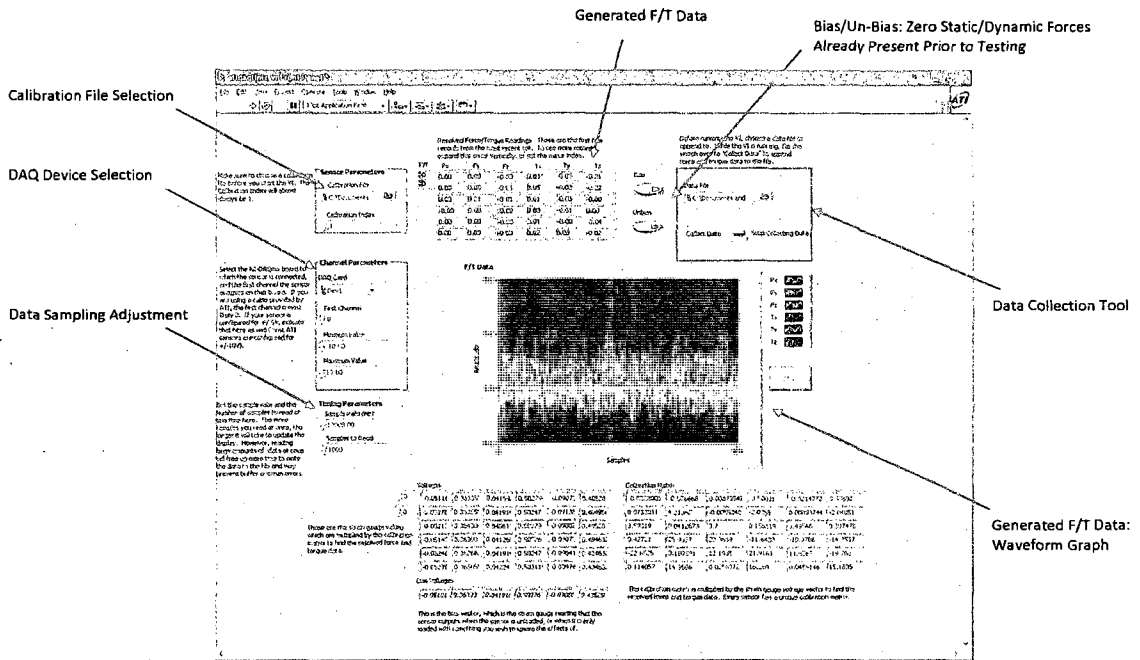
Figure 5.2   ATI-IA Nano 17 F/T Sensor LabVIEW Virtual Instrumentation

5.3.2 Motor Selection

The excess inertia created by the mass of the wing and driving mechanism required a significant amount of torque to be driven. The ideal motor for our application would be able to drive the wing at various speeds and allow for feedback control to optimize output velocity considering that the Figure-8 motion would induce varying loads. Size and weight restrictions also limited our selection since the objective was to prove adequate residual force, lift, could be generated for flight. The torque requirement of approximately 10 – 20 mN-m was would be required to drive the wing mechanism prototype. Considering this, the Faulhaber 2057, [33], brushless DC servo motor provided the desired specification required for this testing application. This compact motor provided an efficient 16 mN-m of torque and could be fitted with planetary gearheads to sustain drive of additional mass. The controller, MCBL 3006s, [34],

48

provided PI feedback control for optimization of velocity control. This 12 volt motor required a standalone power supply that can supply a constant 12 volts and current of up to 10 amperes.

5.4 Testing

5.4.1 Motor Control Optimization

The complexity of the motion profile creates varying loads throughout the wing trajectory. Variation of the angular acceleration present in the Figure-8 spherical motion also complicates motor control for proper velocity output. For optimization of the motor velocity signal, PI controller gain values for the MCBL 3006S controller are adjusted for each flapping speed prior to data collection to steady the motor speed output within a reasonable deviation of 1 – 5 % of the command input. The controller gains can be adjusted using Faulhaber Motion Manager Software. Using Motion Manager, velocity signals and current consumption of the motor can be monitored and collected for evaluation following any test. The following steps were carried out to tune the controller.

1. Set Proportional Gain to 8 and Integral Gain to 20

2. Increase Proportional Gain in increments using a step size of 5 until system to improve output signal.

3. If system becomes unstable, revert to back to the previous Proportional Gain using by the same step size.

4. Increase Proportional Gain using step size of 1 to improve output signal if desired.

5. Increase Integral Gain in increments using a step size of 5 until system becomes unstable.

6. If system becomes unstable, revert to back to the previous Integral Gain using by the same step size.

7. Increase Integral Gain using step size of 1 to improve output signal if desired.

Depending on the speed, these steps reduced deviation resulting in limited angular acceleration which may have corrupted the measured force signal data. Table 5.2 lists gain values used for the wing prototype at the testing speeds indicated.

Table 5.2 PI Controller Gains at Different Wing Flapping Frequency

Flapping Frequency (Hz)	Motor Command Velocity (RPM)	PI Controller	
		Proportional Gain	Integral Gain
2.5	150	10	60
5.0	300	10	50
7.5	450	11	50
10.0	600	11	50
12.25	735	12	50

From the current consumption of the motor and the voltage of the power supply, the relationship between the power required for each testing speed can be made using Equation 5.1.

$$P(t) = V(t) \cdot i(t) \tag{5.1}$$

The current consumption, *i(t)*, is obtained for each test during testing. The velocity signal and power required to drive the wing prototype at speeds of 2.5, 5, 7.5, 10 Hz, and 12.25 Hz, are shown in Figures 5.3, 5.4, 5.5, 5.6, and 5.7 respectively.
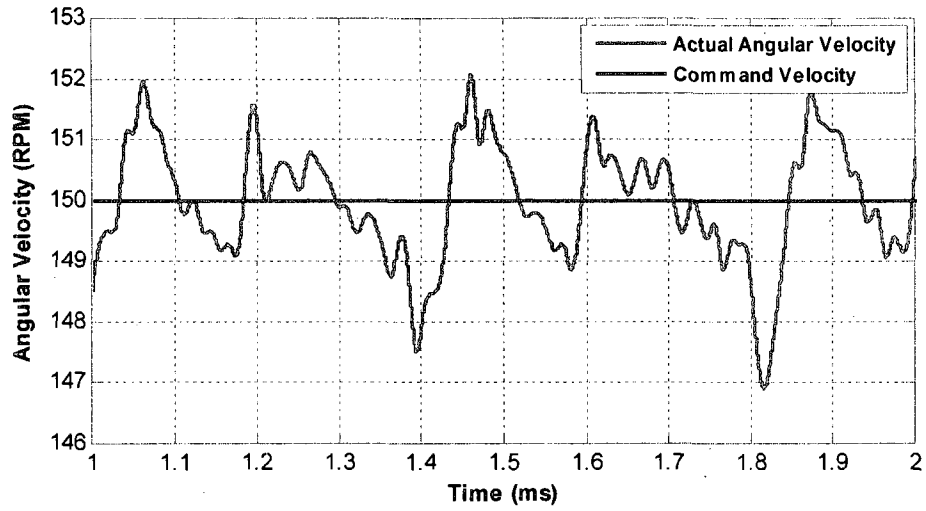
(A)
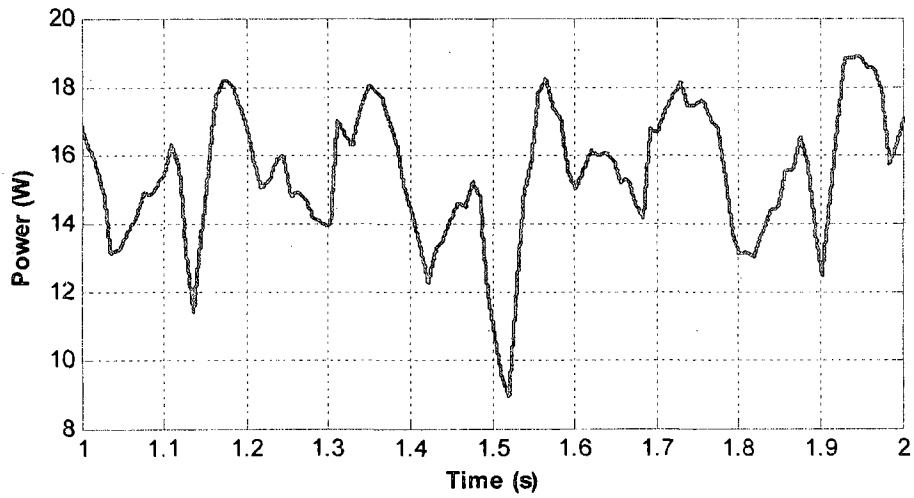
(B)

Figure 5.3   For 2.5 Hz Flapping, (A) Speed Output at 150 RPM with Tuned Controller

Gains and (B) Motor Power Consumption for This Speed
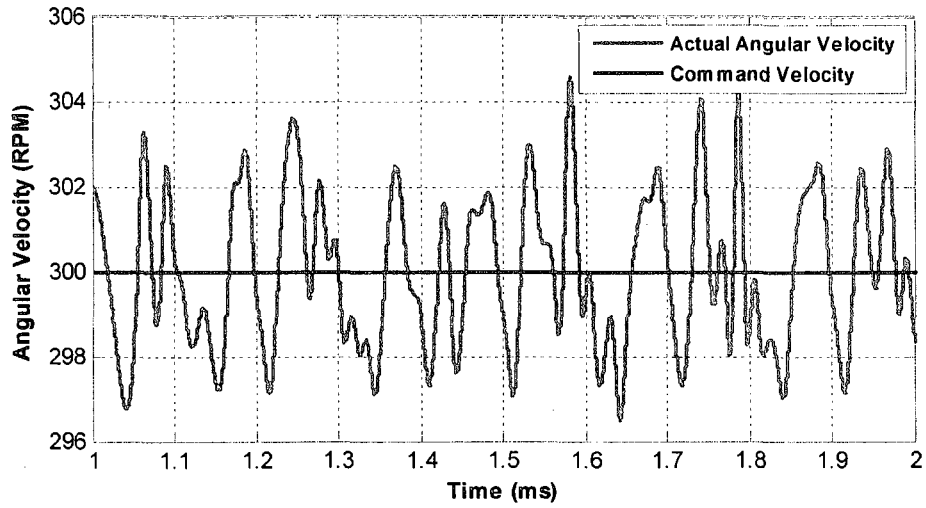
(A)
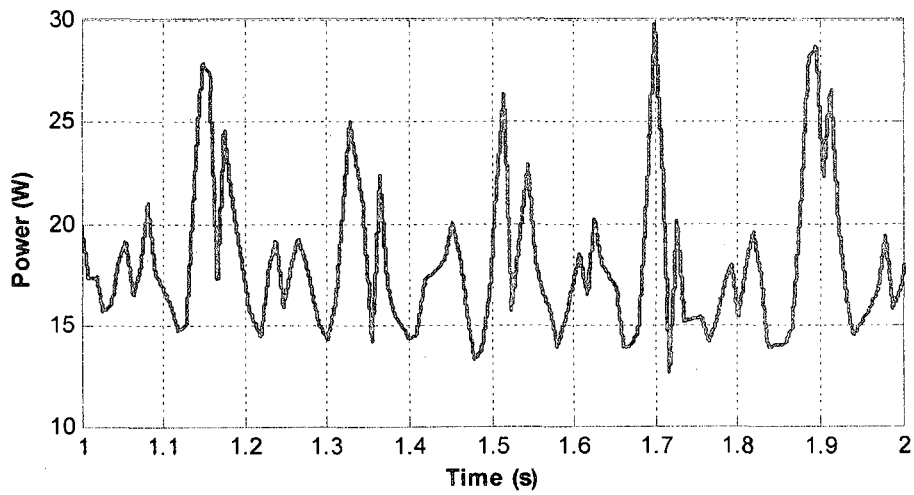
(B)

Figure 5.4   For 5 Hz Flapping, (A) Speed Output at 300 RPM with Tuned Controller

Gains and (B) Motor Power Consumption for This Speed
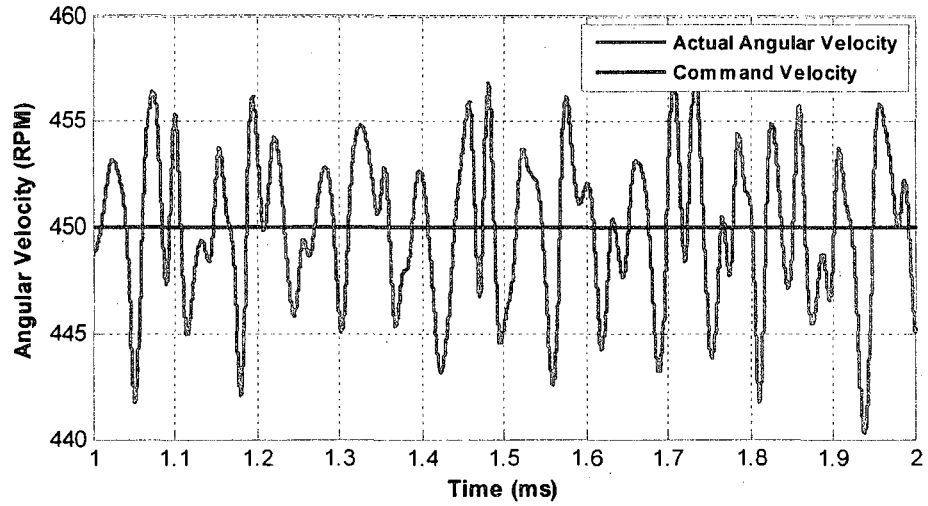
(A)
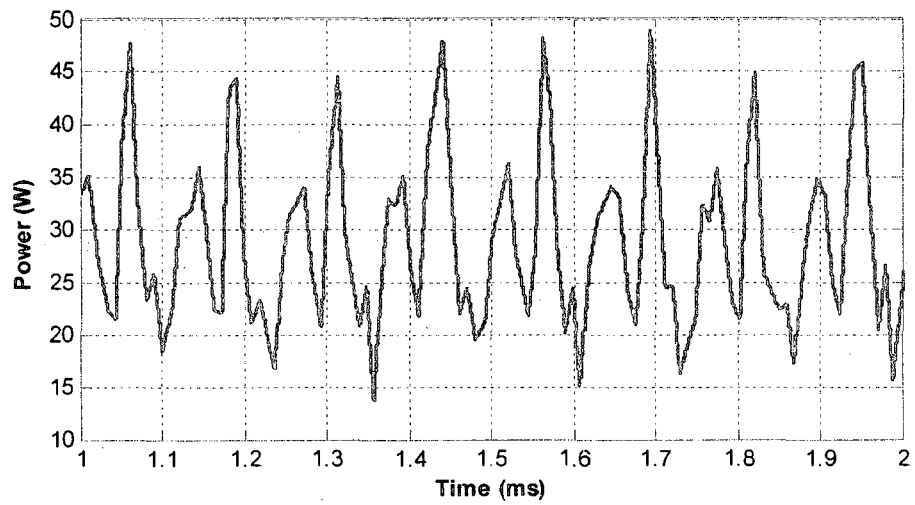
(B)

Figure 5.5 For 7.5 Hz Flapping, (A) Speed Output at 450 RPM with Tuned Controller

Gains (B) Motor Power Consumption for This Speed
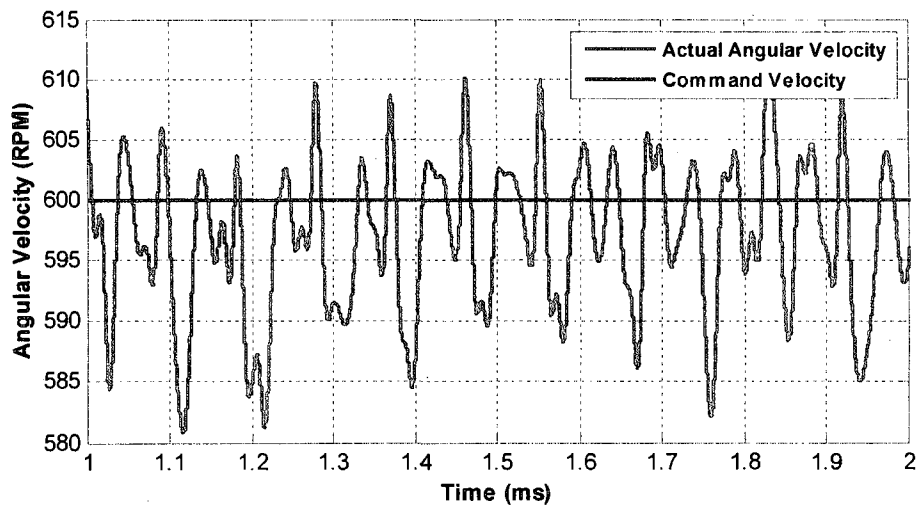
(A)
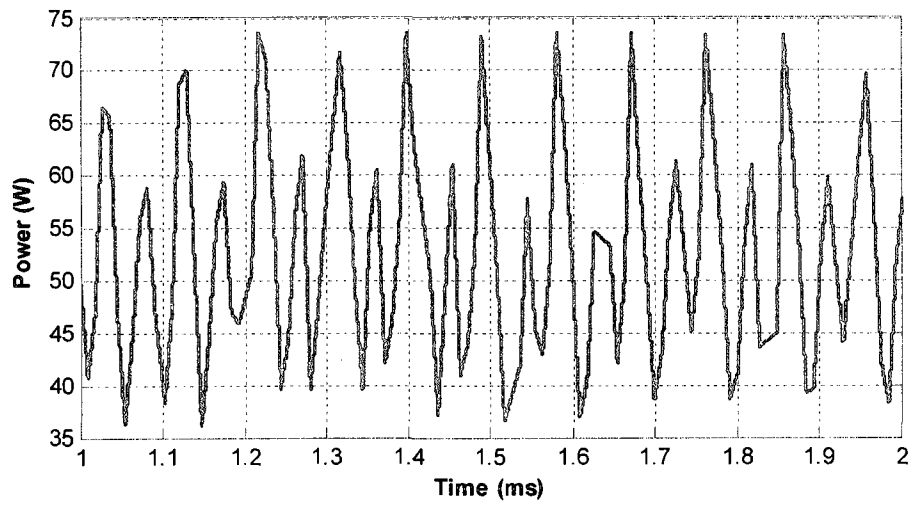
(B)

Figure 5.6   For 10 Hz Flapping, (A) Speed Output at 600 RPM with Tuned Controller

Gains and (B) Motor Power Consumption for This Speed
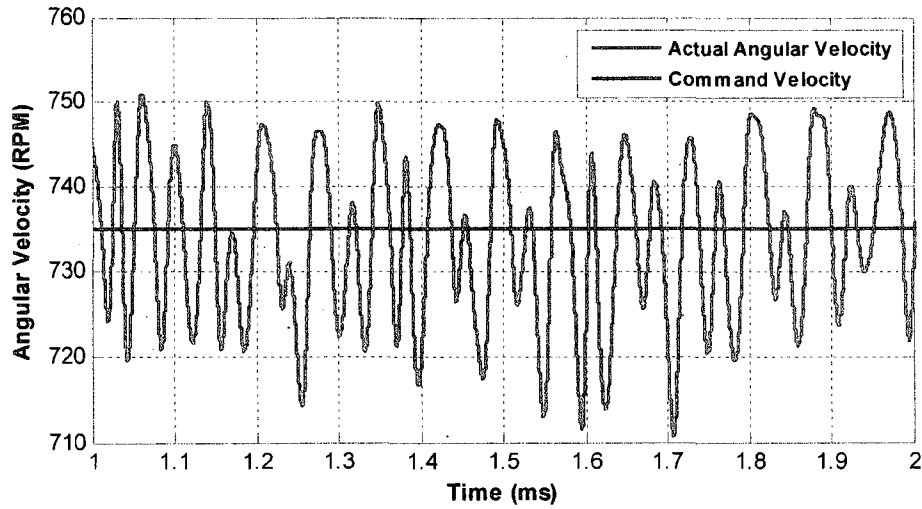
(A)
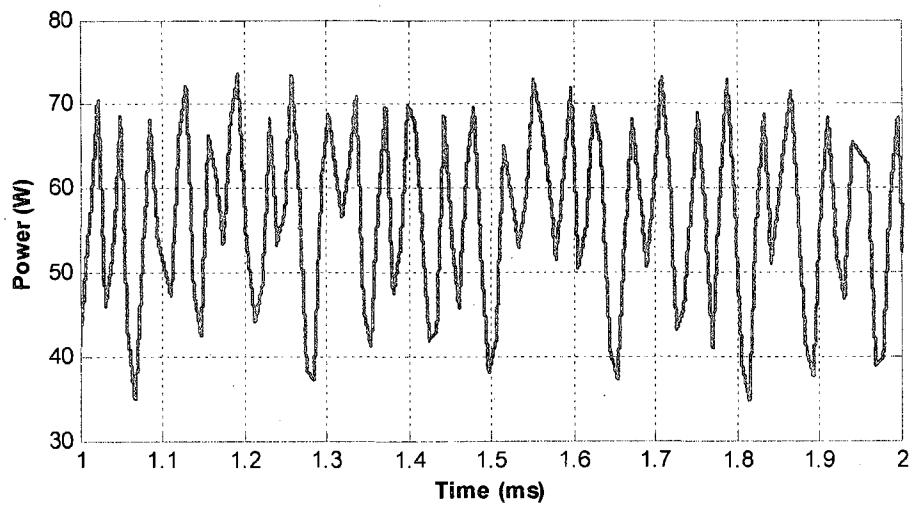
(B)

Figure 5.7   For 12.25 Hz Flapping, (A) Speed Output at 735 RPM with Tuned

Controller Gains and (B) Motor Power Consumption for This Speed

5.4.2 Pre-Testing Conditions

Once the motor has been configured to provide the adequate speed control at the

testing velocity, the wing prototype should be ready for testing. The prototype is aligned

to the initial position of the Figure-8 as indicated in Figure 5.8 and the load cell forces are zeroed to ignore any static effect present at that time. With the load cell attached to the base of the wing, the coordinate frame as shown in Figure 5.8 is assigned. The position of the load cell is set to this position to avoid interference with the load cell cord. The prototype is then set in motion and data is collected for typical testing time of about 6 – 12 seconds. Although the wing prototype is aligned to the initial position of the Figure-8, no such requirement is made for the position where it must stop. An explanation of the force signal produced during motion is examined later in this chapter.
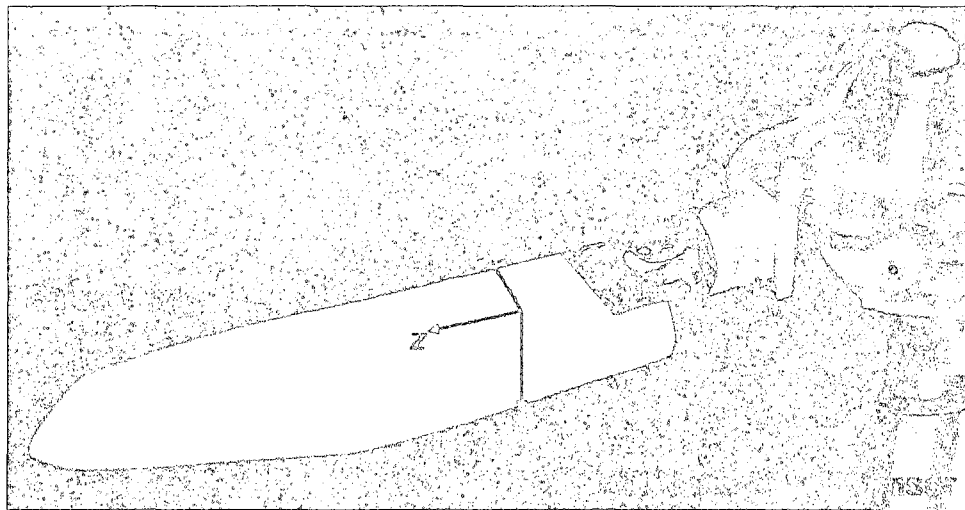
Figure 5.8   Wing Prototype at the Initial Position of Figure-8 with Load Cell Attached and Coordinate Frame Assigned

5.5 Data Analysis

5.5.1 Filtering

Acquired experimental force signals contain significant noise that contaminate the data and must be removed to interpret the forces produced during testing. Using Fast

Fourier Transform technique for digital signal processing, the dominate frequencies of the acquired data signal are classified. Higher order frequencies are eliminated from the data using a Butterworth low pass filter. Depending on the testing frequency, the cutoff is typically 25 – 50 Hz. A Butterworth filter provides the most efficient filter for this application by generating smooth curves for the given data. All six force components are filtered and verified for accuracy. The moving average of the collected data is also taken at times using 250 – 500 samples for additionally information on the values and trend of each component.. The data corresponding to prototype testing will be filtered and a more detailed analysis will be provided in Chapter 7. The results of prototype testing and comparisons with model results will be provided in Chapter 7 as well.

5.6 Force Signal Interpretation

Interpreting the measured force signal involves understanding the phase during the Figure-8 cycle a directional force is present and when it should peak. Since our data has shown consistency over all flapping frequencies, reasoning of the of the axial force, F_x, and normal force, F_y, is explained in the Figures below.

5.6.1 Chord-wise Force, F_x, Interpretation

The chord-wise force, F_x, induced by the Figure-8 wing motion represents dynamic and drag forces as the wing moves through air. The wing phases are divided into sections and reasoning for the measured force signal is provided, Figure 5.9. Since the load cell is attached the base of the wing, forces induced by the movement of the wing through its motion cycle are the only contributing factors to the signal.

Figure 5.9   Chord-wise Force, F_x, Representation for Figure-8 Cycle

A. Initial Position: Wing Prototype is aligned horizontally initially prior to testing. At this location, A, the load cell is zeroed to eliminate any static load present. Although, the load cell is zeroed, the load cell does not assume the same for dynamic forces. This position does represent the maximum position along the positive chord-wise direction according to the Figure-8 trajectory. Therefore, F_x, is reaches its max value at this position. The angle of attack during this phase is 90°.

B. Quarter Cycle: During this phase, the wing is slicing through the air with angle of attack of 0° transitioning to the other half of the Figure-8 trajectory. At this position, B, the wing is half way from its maximum and minimum along the chord-wise direction. Additionally, maximum acceleration is likely present at

section; therefore, it is zero at this location and transitioning to its opposite amplitude peak.

C. Half Cycle: The wing trajectory has reached it opposite maximum end along the chord-wise direction. This position represents the same magnitude opposite direction to the initial position.

D. Three-Quarter Cycle: Similar to position B, this wing is now moving in the opposite direction, hence F_x is zero.

E. Full Cycle: Reaches back to initial position where F_x is maximum.

5.6.2 Normal Force, F_y, Interpretation

The normal force, F_y, induced by the Figure-8 wing motion also represents dynamic and lift forces as the wing moves through air. Similarly, the wing phases are divided into sections and reasoning for the measured force signal is detailed below and shown in Figure 5.10.
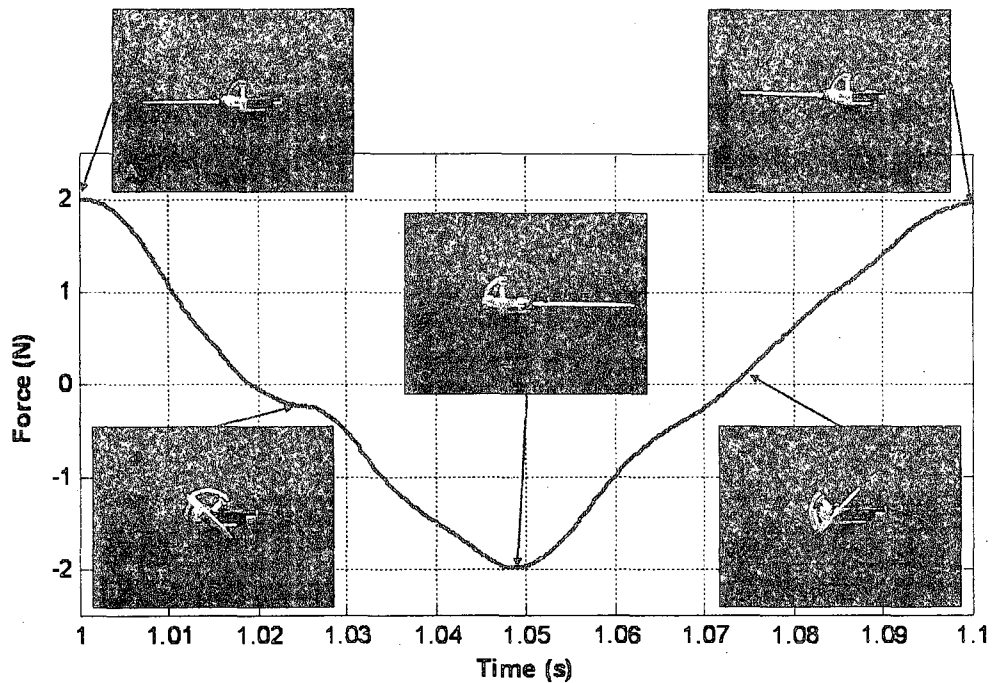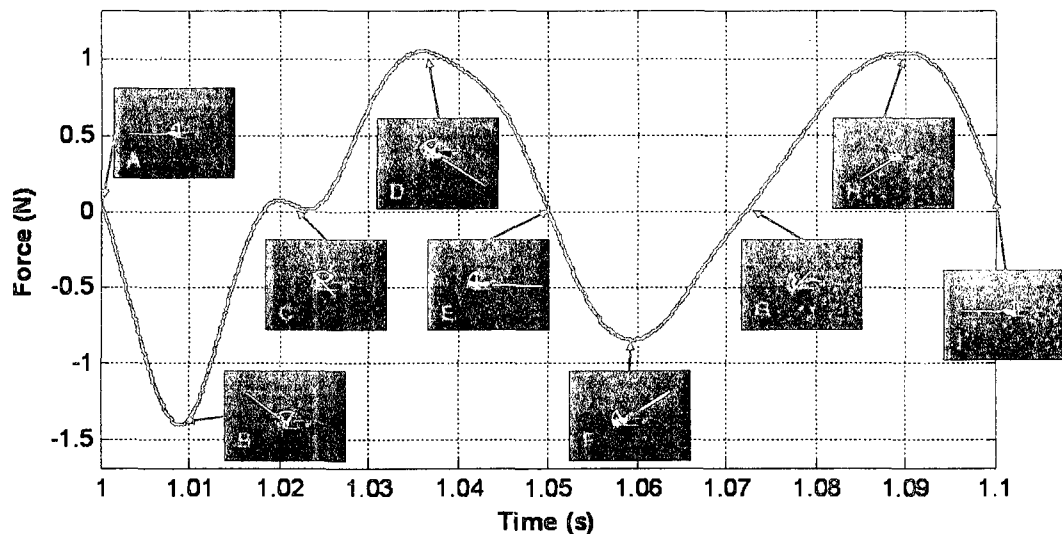

Figure 5.10 Normal Force, F_y, Representation for Figure-8 Cycle

59

A. Initial Position: Wing Prototype is aligned horizontally initially prior to testing. At this location the normal force, F_y, is zero.

B. Eighth Cycle: During this phase, the wing is up-stroking stroking as the angle of attack is decreasing from 90°. F_y reaches is first peak at this position.

C. Quarter Cycle: The wing is half way from transitioning from its first and second peak. As it reaches 0° angle of attack and is coincident with the stroke-plane or axis of symmetry along the Figure-8, F_y is zero.

D. Three-Eighth Cycle: F_y is again maximum as it reaches its opposite amplitude peak during the first half of the Figure-8 cycle. During this phase it is transitioning from 0° to 90° angle of attack.

E. Half Cycle: F_y is zero similar to initial position, it is coincident and parallel to the Figure-8 stroke plane and axis of symmetry.

As shown in the figure and indicated in the Figure-8 trajectory, double peaks are present in the F_y force. From position E, F_y will again oscillate from maximum to minimum during the second half of the Figure-8 cycle until it reaches its initial position.

5.6 Motion Verification

The validity of the design and collected force signal is dependent on whether proper motion trajectory is achieved by the wing prototype. The use of the spherical four-bar mechanism with the angular dimensions assigned to each link will allow the coupler to outline a two plane symmetrical Figure-8 coupler curve. However, it is essential to verify the motion trajectory of the prototype for surety of test results and that the design objective as outline in Chapter 3 is met. Still and high speed video imagery is used to

establish the accuracy of the motion trajectory. Figure 5.11 is a still image taken during experimental testing at 10 Hz which indicates the Figure-8 motion of the wing. High speed video imagery was used to track selected points on marked on the wing in motion at 7.5 Hz as detailed in Appendix B. With motion tracking, we can plot the trajectory of any marked point to verify the wing motion and classify any deviations in the wing trajectory as a result of wing flexibility. Figure 5.12 shows the plot of point 22 on the wing as it cycles through the Figure-8 motion. As shown, the wing generally follows the desired wing trajectory with any deviation most likely a result of torsional and bending deformation.
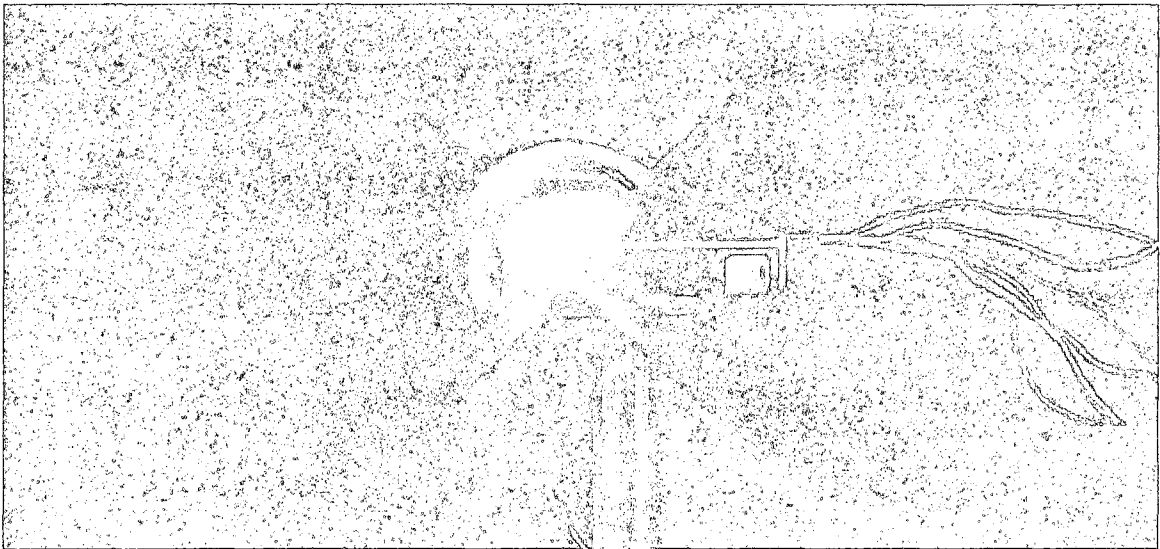
Figure 5.11   Figure-8 Motion Trajectory Generated at 10 Hz
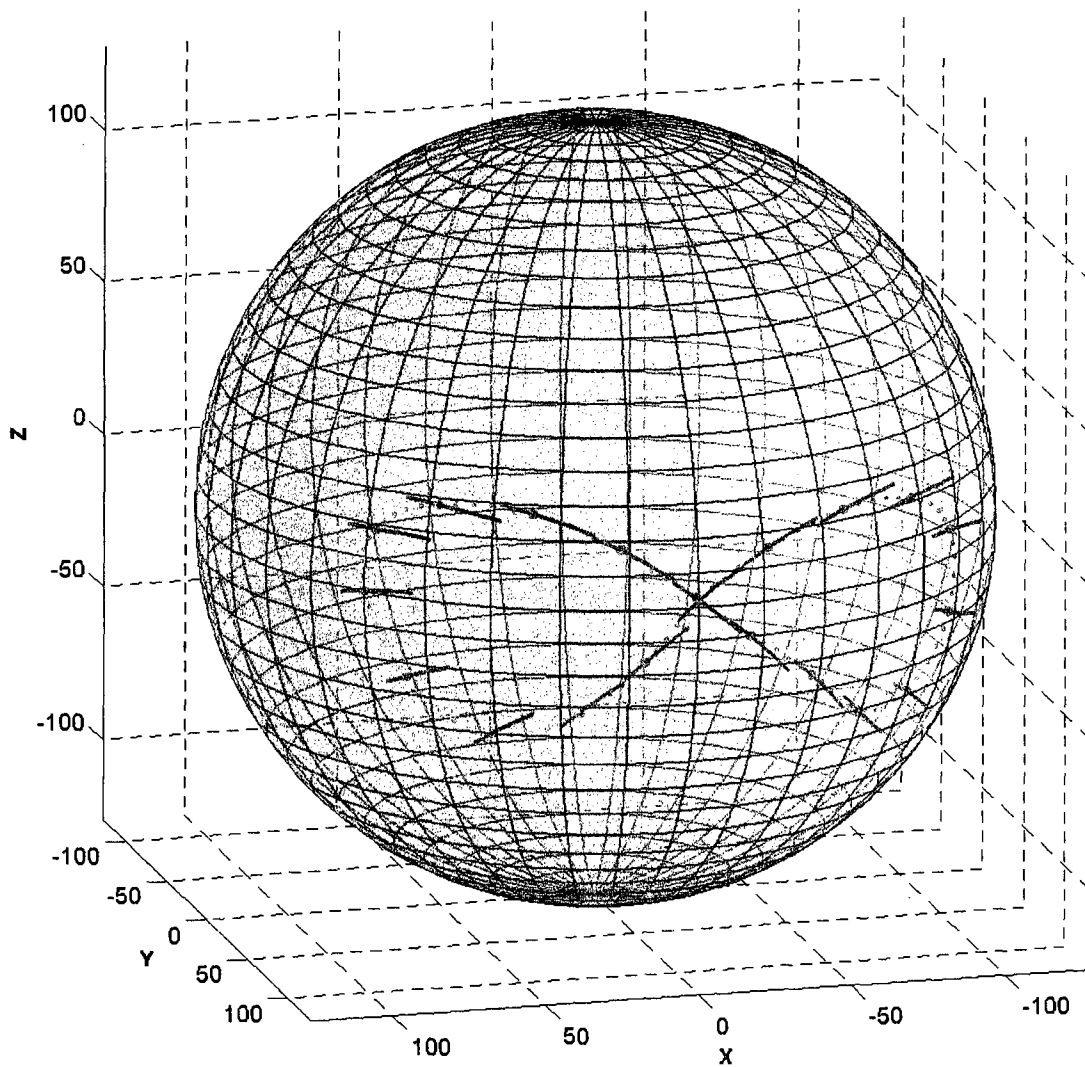
Figure 5.12   Figure-8 of High Speed Motion Capture of Point 22 of Figure A.2

CHAPTER 6

WIND TUNNEL TESTING

6.1 Objective

To realize the potential flight capabilities of Figure-8 spherical motion, the flight characteristics must be quantified. To achieve this, the lift and drag effects associated with this wing motion must be identified. As the wing prototype cycles through Figure-8 spherical motion, high angles of attack are reached making it difficult to predict the behavior of air flow around the wing. The wing is initially positioned 90° angle of attack, and cycles between 0° to 90° angle of attack throughout the wing trajectory. To determine the lift and drag experienced by the wing prototype, wind tunnel experimentation is conducted. The wing is rotated in the wind tunnel at quasi-static and dynamic conditions. Data is collected as the wing is rotated for a half and full cycle depending on the type of test, at a wind speed equivalent to the free stream velocity at about 10 – 12.25 Hz. Using the data collected; we can calculate the coefficients of lift, C_l, and drag, C_d, for the complete cycle. Since our wing motion only reaches 90° angle of attack, data corresponding to this portion of the cycle, 0 – 90° angle of attack, is interpreted.

6.2 Free Stream Velocity and Angle of Attack

During the cycle of Figure-8 motion, the wing is subjected to changes in angle of attack that needs to be identified to interpret lift and drag variation. For prototype testing, the wing is stationary, so airflow is assumed to be zero and any fluid movement is a result of wing motion. Accordingly, we define the free stream velocity, V, of the Figure-8 motion as the velocity induced over the wing acting tangent to the wing trajectory, Figure 6.1. Moreover, the velocity component in the direction of the wing edge is defined as U. Figure 6.2 displays the velocity interpretation over the wing profile.
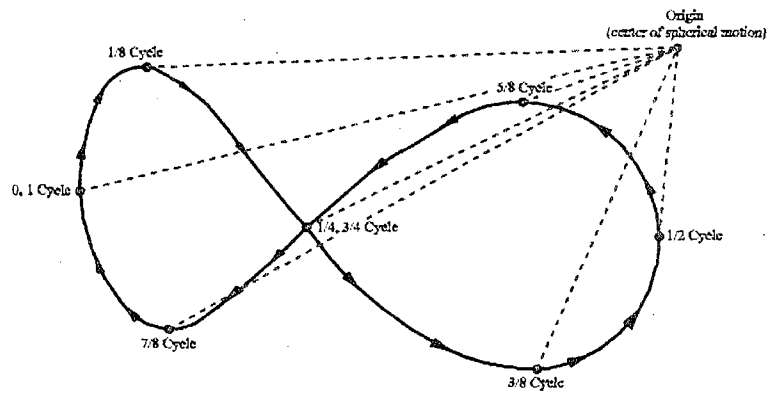
Figure 6.1   Wing Point Trajectory and Induced Velocity
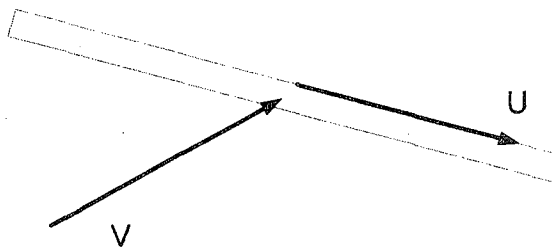
Figure 6.2   Free Stream Velocity, V, and Velocity along the Wing Edge, U

The angle of attack for the duration of a complete cycle is defined by the orientation of the wing with respect to the direction of two velocity vectors. Equation 6.1 indicates how the angle of attack was defined for the Figure-8 motion. Figure 6.3 displays the angle of attack over the complete cycle of the Figure-8 motion.

$$\alpha = \cos^{-1}\left(\frac{U}{V}\right) \qquad\qquad 6.1$$
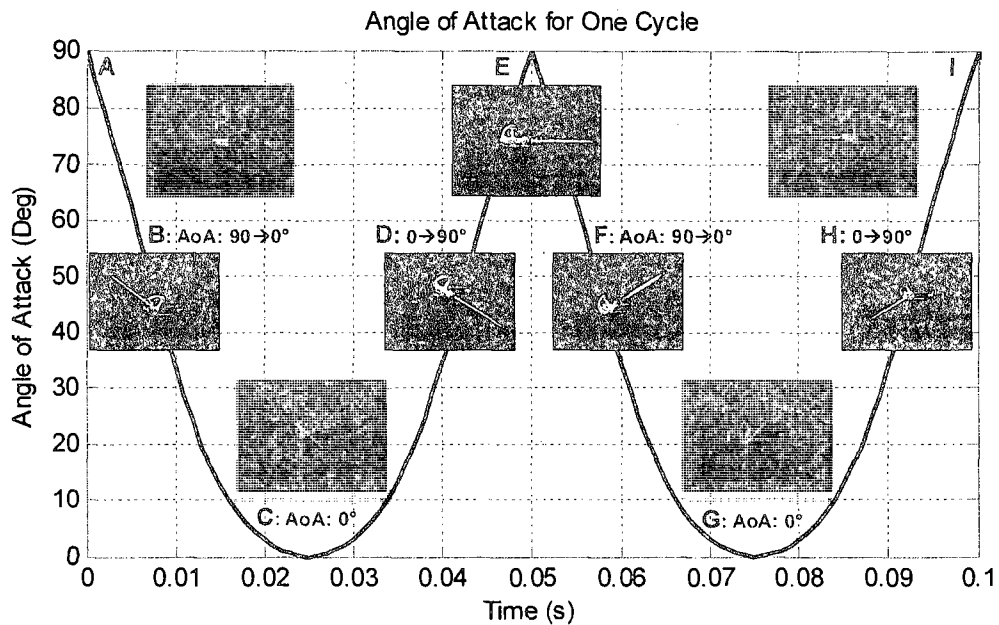
Figure 6.3   Variation in Angle of Attack in the Figure-8 Cycle

In addition to the coefficient of lift, C_l, and drag, C_d, the center of pressure, C_p, can also be determined. The ATI-IA Nano 17 F/T load cell will be used to measure the force signal which will include moments produced by the wind speed. Therefore, the center of pressure, C_p, can be calculated by manipulating the force and moment signal. This will determine any shift in C_P as the wing reaches higher angle of attack. Better insight on modeling this motion will be possible by determining the C_p location rather than

assuming the convention quarter-chord location in accordance with thin air foil theory. Figure 6.4 shows the assumed location of C_P and the acting aerodynamic forces.
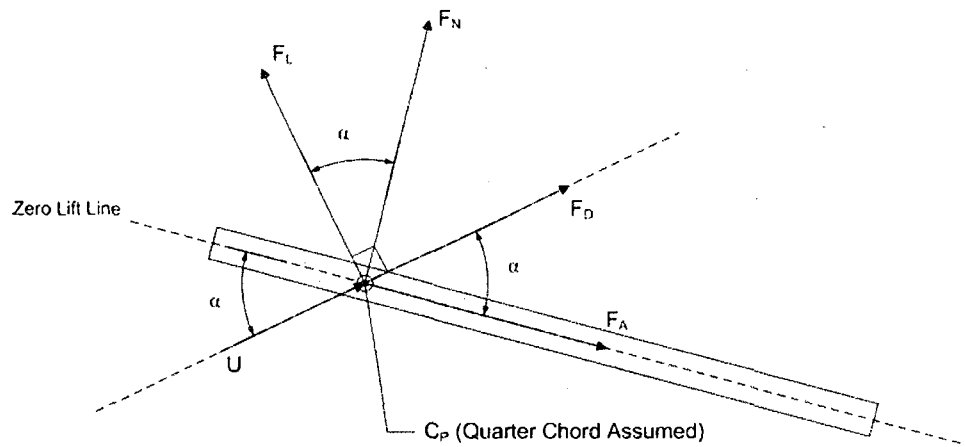
Figure 6.4   Cross-sectional View of Airfoil with C_P and Aerodynamic Forces

6.3 Setup and Apparatus

To simulate proper wing movement of the wing in the wind tunnel, a setup consisting of a force/torque load cell, motor, and wing is required. It was desired to have the wing setup near the center of the wind tunnel mounting area along with the motor and sensor to rotate the wing and collect data. First a base mount that can be attached to the bottom of the wind tunnel and support the motor was machined. The DC servo motor, Faulhaber V2057S0012 with gear reduction of 9.7:1 used for prototype testing and capable of stepper functions, was attached to the base mount. The load cell was attached to the base of the wing retaining the coordinate frame as used for prototype testing. The load cell will rotate with the wing; thereby, eliminating the need force transformation. A coupler piece is machined to attach the wing and sensor to the motor. Lastly, to limit and disturbances created by the wind speed which may incorporate erroneous data to the measured force

signal, a symmetrical airfoil is placed over the base mount to cover the motor. Figure 6.5 shows a conceptual model of the wind tunnel and Figure 6.6 shows the actual setup. Figure 6.7 indicates the initial position of the wing the change in angle of attack as it rotates.
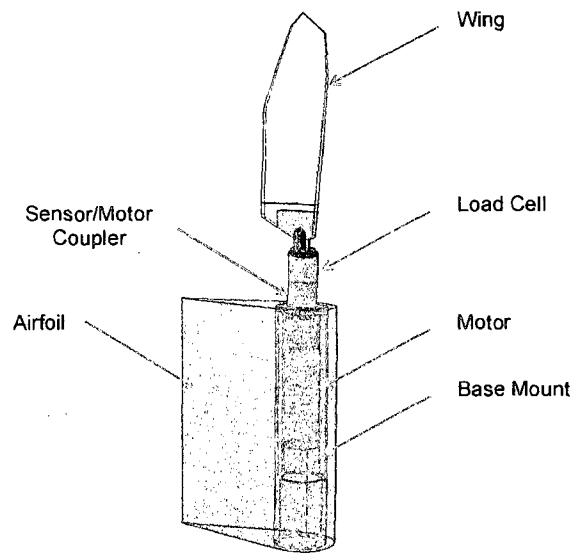
Figure 6.5   Conceptual Rendering of Wind Tunnel Experimentation
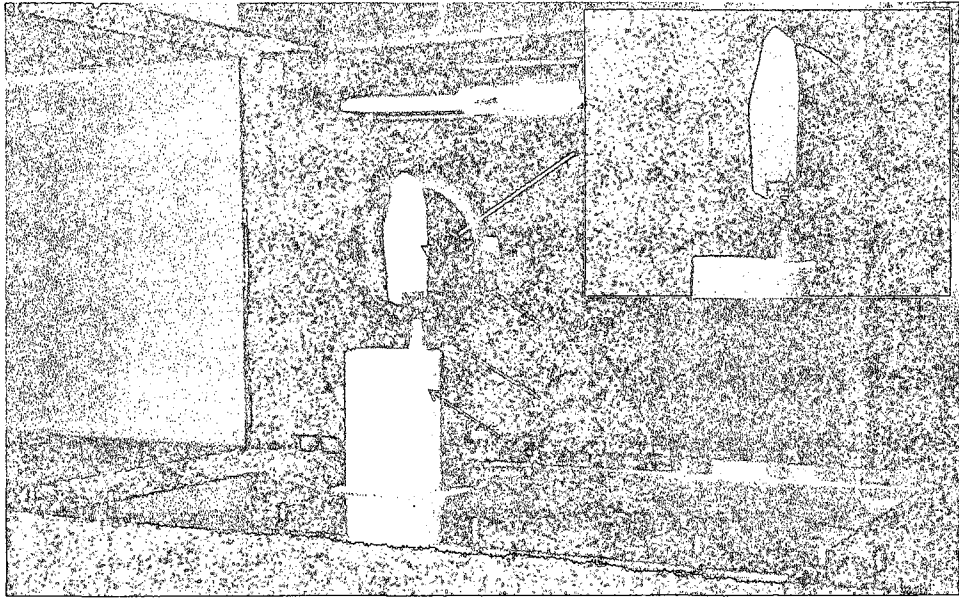
Figure 6.6   Wind Tunnel Experimentation Setup
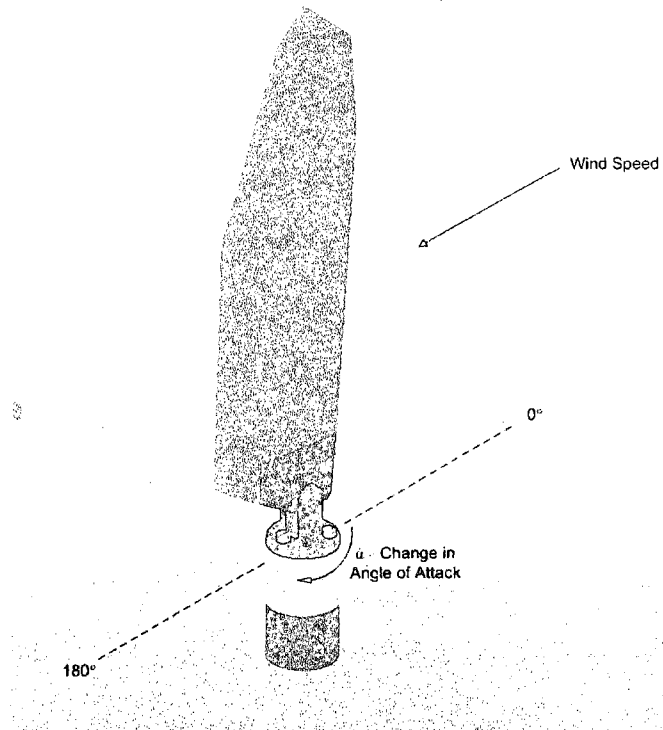
Figure 6.7   Wing Rotation in Wind Tunnel With Respect to Angle of Attack

6.3.1 Setup Conditions

In calculating the coefficients of flight for any given test, certain testing conditions need to be identified prior to testing. Working with an open circuit wind tunnel, constant air flow and air properties of the testing environment are essential in obtaining accurate results. Ambient pressure and temperature readings are needed to calculate the air density before and during testing. A log of the pressure and temperature was kept for every half hour starting about two hours before testing to classify any dramatic changes in ambient conditions. This data was used to calculate the air density using Equation 6.2.

$$\rho = \frac{p}{R \cdot T} \qquad (6.2)$$

In the equation, R is the gas constant, p is the measured pressure, and T is the measured temperature. The ambient relative humidity was not considered in pressure calculations with the assumption of only dry air present.

6.3.2 Motor Control in Stepper Mode

The Faulhaber DC servo motor was to be driven in stepper mode to control the speed and position of the wing. Using a function generator virtual instrumen0ptation program created in LabVIEW, analog pulse inputs were supplied to the MCBL 30906s controller from an NI Elvis station to allow rotation as needed. The steps per revolution are freely programmable by setting two parameters on the motor controller, *STW*, step width or number of steps per encoder pulse, and *STN*, step number or number of steps per revolution. Both values could be set from 0 to 65,535 depending on the application.

6.4 Quasi-Static Analysis

Initial wind tunnel testing was conducted using quasi-static conditions by rotating the wing slowly at 1.2887 revolutions per minute or about 0.2 Hz. The slow change in angle of attack provided insight on how airflow affected the wing during static changes in angle of attack rather than dynamic. The gearhead on the motor made it mechanically difficult for it to driven at constant angular velocity of 1 RPM; therefore, the motor was configured to rotate at slightly higher angular velocity of 1.2887 RPM. The step width, STW, and step number, STN, were set to one and 60,000 respectively enabling the motor to step 1/60,000 of a revolution or $[1.67 \ 10^{-5}]°$ per pulse input. Table 6.1 lists motor parameters for this experiment. The wing is rotated from 0 to 180° angle of attack, but data for only 0 to 90° will be examined since Figure-8 wing motion reaches a maximum of 90° angle of attack.

Table 6.1   Motor Testing Parameters for Quasi-Static Testing

STN	STW	Frequency (Hz)	No. of Revolutions	No. of Pulses	Motor Output (RPM)	Time Elapsed (s)
1	60,000	250	0.5	30,000	1.2887	23.28

6.4.1 Coefficients of Axial and Normal Force

The measured force signal represents the aerodynamic forces induced by the wind speed as the wing is rotating in the wind tunnel. Since the load cell is rotating with the wing, alignment of the x and y axis along the chord-wise and normal direction is maintained. The coefficients of axial force, C_a, and normal force, C_n, can be calculated

using F_x and F_y data respectively. First the force signal is filtered at 1 Hz in accordance with the signal's FFT and then Equations 6.3 and 6.4 are used to calculate C_a and C_n.

$$C_a = \frac{F_x}{\frac{1}{2}\rho_{air} v^2 \cdot S} \tag{6.3}$$

$$C_n = \frac{F_y}{\frac{1}{2}\rho_{air} v^2 \cdot S} \tag{6.4}$$

The density of air, ρ, is calculated by the ambient pressure and temperature during the time of testing. The wing surface area, S, is determined using the solid model as designed in SolidWorks. Table 6.2 list the testing and wing parameters needed for these calculations. The filtered force signals F_x, Figure 6.8, and F_y, Figure 6.9, are displayed for this testing. Figures 6.10 and 6.11 display the coefficient of axial force, C_a, and normal forces, C_n, from 0 - 90° for this test respectively. These coefficients are used to determine the aerodynamic model as outlined in Appendix C.

Table 6.2 Testing Conditions and Parameters for Quasi-Static Testing

Wind Speed (MPH)	Wind Speed (m/s)	Air Density (ρ, kg/m^3)	Wing Surface Area (S, m^2)
10	4.4704	1.103867483	0.0040639434
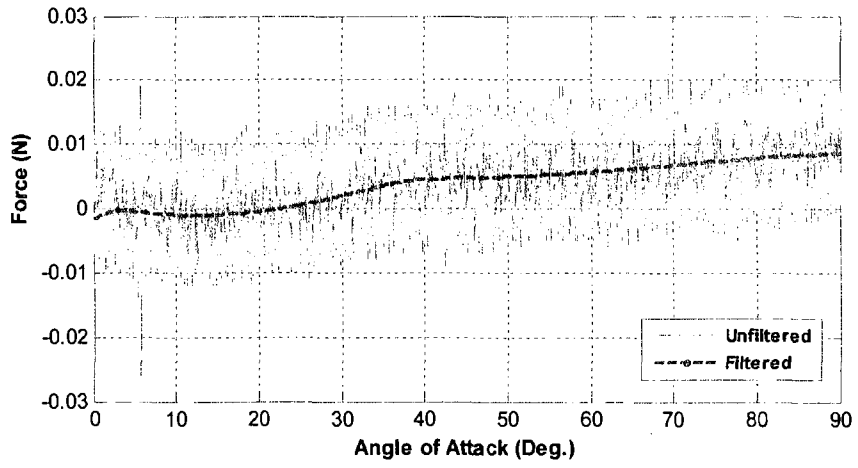
Figure 6.8 Force Signal, F_x, for Quasi-Static Wind Tunnel Testing
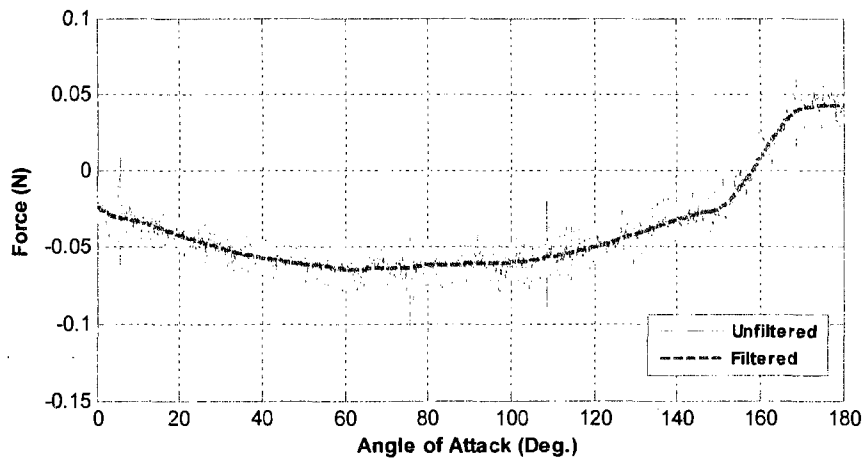
Figure 6.9 Force Signal, F_y, for Quasi-Static Wind Tunnel Testing
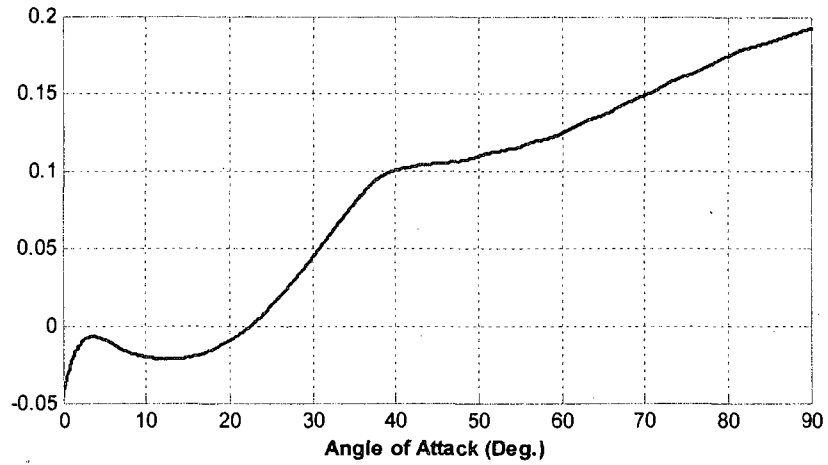
Figure 6.10   Coefficient of Axial Force, C_a, from 0-90° Angle of Attack for Quasi-Static

Wind Tunnel Simulation
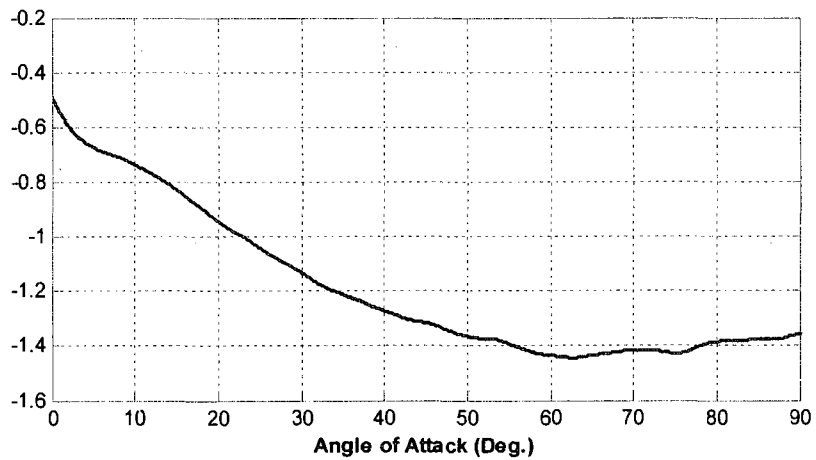
Figure 6.11   Coefficient of Normal Force, C_n, from 0-90° Angle of Attack for Quasi-

Static Wind Tunnel Simulation

6.4.2 Coefficients of Lift and Drag

The coefficients of lift, C_l, and drag, C_d, are defined by the lift and drag force induced

on the wing by the wind speed. The lift force, F_L, is perpendicular to the direction of

velocity and the drag force, F_D, is parallel to the direction of velocity, Figure 6.4. Therefore, at any angle of attack, α, C_l and C_d can be calculated by using transformations of C_a and C_n with respect to the angle of attack as shown in Equations 6.5 and 6.6.

$$C_l = C_n \cos(\alpha) - C_a \sin(\alpha) \tag{6.5}$$

$$C_d = C_n \sin(\alpha) + C_a \cos(\alpha) \tag{6.6}$$

The change in lift and drag can be seen in Figures 6.12, which displays C_l and C_d over 0 – 90° angle of attack.
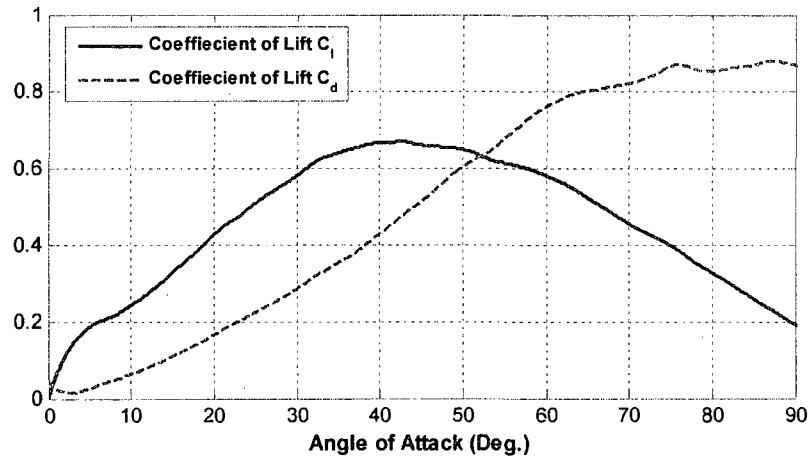
Figure 6.12   Coefficient of Lift, C_l, and Drag, C_d, for 0-90° Angle of Attack for Quasi-Static Wind Tunnel Simulation

From the change in lift and drag, the following analysis can be made about the aerodynamic coefficients for the wing at varying angle of attack under quasi-static conditions.

- Both C_l and C_d start from close to zero at 0° angle of attack. There should not be any lift or drag when the wing is slicing through at the Figure-8 trajectory as

74

indicated in Figure 6.3 with the free stream velocity along the trajectory. The minimal drag present is induced by the free-stream velocity induced on the wing thickness.

- Increase in both lift and drag is noticed a we transition to 40° angle of attack. The lift and drag forces should increase as the angle of attack increases producing more significant aerodynamic forces.

- The lift starts to decline at about 40° angle of attack indicating the stall angle, or angle at which airflow is no longer attached to the upper surface of the wing. Although the stall angle is predicted to be higher, 45°, the lower stall angle is due to quasi-static simulation. The stall angle under dynamic conditions should be higher or closer to a predicted value of 45°.

- The drag continues to increase and becomes the dominant aerodynamic component as the wing transitions past 40° angle of attack. The increased surface area exposure to the free stream velocity is responsible for the increase drag as it progresses to 90° angle of attack as indicated in Figure 6.3.

- Theoretically, there should be no lift present at 90° angle of attack as otherwise shown in the plot. This discrepancy in the measurement can be interpreted by a slight misalignment of the ending position of the wing, which induces a lift force.

- Since a finite wing is used in the wind tunnel, vortices may have little influence on the results and cannot be avoided. This effect may be more apparent when results are compared to those obtained from CFD modeling.

6.4.3 Center of Pressure

The continuous variation in angle of attack during the course of a cycle in Figure-8 spherical motion is likely to shift the location of the center of pressure, C_p, along the chord and span length of the wing. With the net aerodynamic forces acting at the C_p, any aerodynamic moments at this point are zero. Since the load cell is not aligned along the C_p axis of the wing, a moment signal is incorporated into the data collected. The moment data can be used to determine the location of C_p with respect to the load cell tooling surface. Figure 6.13 shows the distance vector, R, defined to calculate the moments induced by the forces acting on the wing in the wind tunnel. Equations 6.7 and 6.8 indicate the moments acting on the wing.
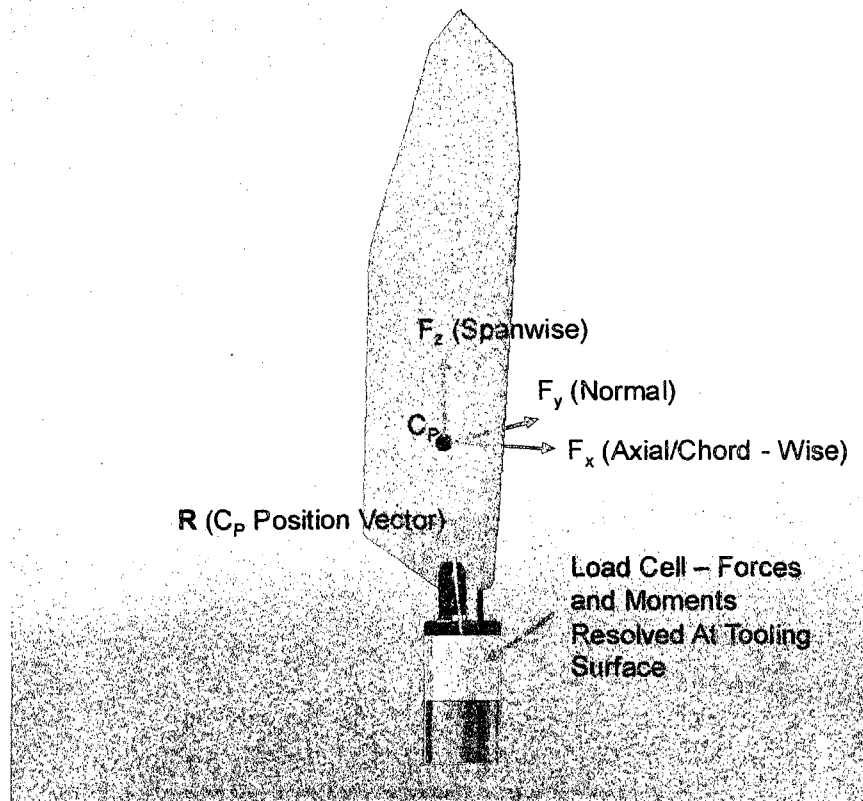
Figure 6.13 C_p Position Vector, R, Definition

76

$$M_x = F_z R_y - F_y R_z$$
$$M_y = F_x R_z + F_z R_x \tag{6.7}$$
$$M_z = F_y R_x - F_x R_y$$

$$
\begin{bmatrix} 0 & F_z & -F_y \\ F_z & 0 & F_x \\ F_y & -F_x & 0 \end{bmatrix}
\begin{Bmatrix} R_x \\ R_y \\ R_z \end{Bmatrix} =
\begin{bmatrix} M_x \\ M_y \\ M_z \end{bmatrix} \tag{6.8}
$$

With the tapered wing thickness, 4 mm at the base to 1 mm at the tip, the change in C_p along the y axis is negligible, thus R_y is zero. Ideally, the span-wise force, F_z, should be zero given that wind speed will not induce force in that direction; however, this force may be present in the signal since a finite wing is used for experimentation with effects of vortices unknown. For C_p calculation purposes, F_z is assumed to be zero. Lastly, M_y is also assumed to be zero because of the relatively small wing thickness the forces producing this moment are applied to. Updating Equation 6.7 with the assumptions outlined yields Equation 6.9 used to determine the change in C_p along the wing chord-wise and span-wise direction. Figure 6.14 shows the change in C_p over the angle of attack for quasi-static testing.

$$
\begin{bmatrix} 0 & -F_y \\ F_y & 0 \end{bmatrix}
\begin{Bmatrix} R_x \\ R_z \end{Bmatrix} =
\begin{bmatrix} M_x \\ M_z \end{bmatrix} \tag{6.9}
$$
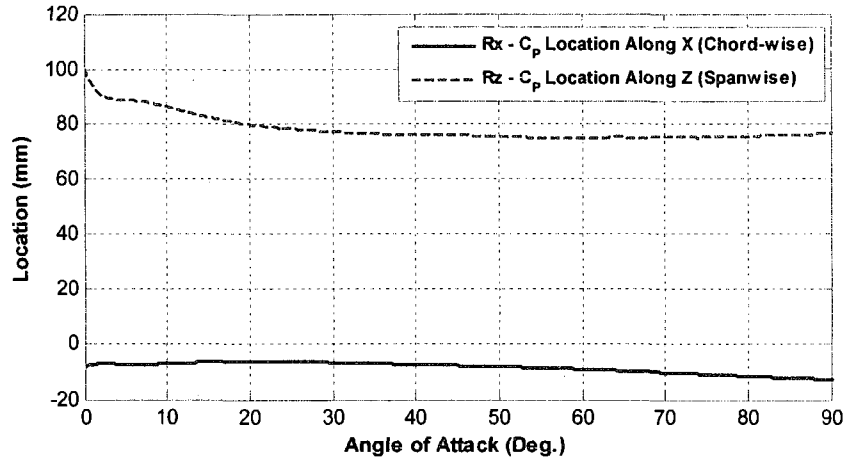
Figure 6.14   Change in Center of Pressure, C_P, in Chord-wise and Span-wise Direction

for 0-90° Angle of Attack

The location of center of pressure, C_P can assist in modeling the aerodynamic forces rather than assuming a conventional quarter-chord location for thin plate airfoil. From the plot above, the location of C_P shifts along the span-wise direction by initially starting at 100 mm from the load cell tooling surface. The span-wise location steadies after 30° angle of attack. The chord-wise shift in C_P signifies that quarter chord location is assumed initially, but deviates to near half chord location at higher angle of attack.

6.5 Dynamic Analysis

Another round of wind tunnel testing was conducted to simulate dynamic change in angle of attack more accurately representing our prototype testing scenario. Similar to quasi-static analysis, the wing is rotated in the wing tunnel, full revolution for this test, and the force signal is examined. The force signal will be used to determine the coefficients of axial and normal force, C_a and C_n, and for coefficients of lift and drag, C_l

and C_d. For this test, the wing is rotated for a full revolution, 0 - 360° angle of attack, at 1 Hz. The rotation of a complete cycle will eliminate any deceleration force required to stop the attached wing and load cell assembly which may be incurred if rotated for half a revolution. This force would distort the data with erroneous information not pertaining to the actual testing. The DC motor was again configured for use in stepper mode and provided a step of 0.0005° per pulse input. Table 6.3 lists the motor parameters assigned for this test and Table 6.4 lists the testing conditions.

Table 6.3   Motor Testing Parameters for Dynamic Testing

STN	STW	Frequency (Hz)	No. of Revolutions	No. of Pulses	Motor Output (RPM)	Time Elapsed (s)
1	2,000	250	1	2,000	60	1

Table 6.4   Testing Conditions and Parameters for Dynamic Testing

Wind Speed (MPH)	Wind Speed (m/s)	Air Density (ρ, kg/m^3)	Wing Surface Area (S, m^2)
10	4.4704	1.118301672	0.0040639434

6.5.1 Coefficients of Axial and Normal Force

The coefficient of axial, C_a, and normal force, C_n, are calculated for dynamic wind tunnel simulation similar to quasi-static using Equations 6.3 and 6.4. These coefficients are incorporated into the model outlined in Appendix C. Figures 6.15 and 6.16 represent the force signal F_x and F_y for dynamic wind tunnel testing, which is filtered at 10 Hz in accordance with the FFT. The coefficient of axial force, C_a, and coefficient of normal force, C_n, from 0 – 90° angle of attack are plotted in Figure 6.17 and 6.18 respectively.
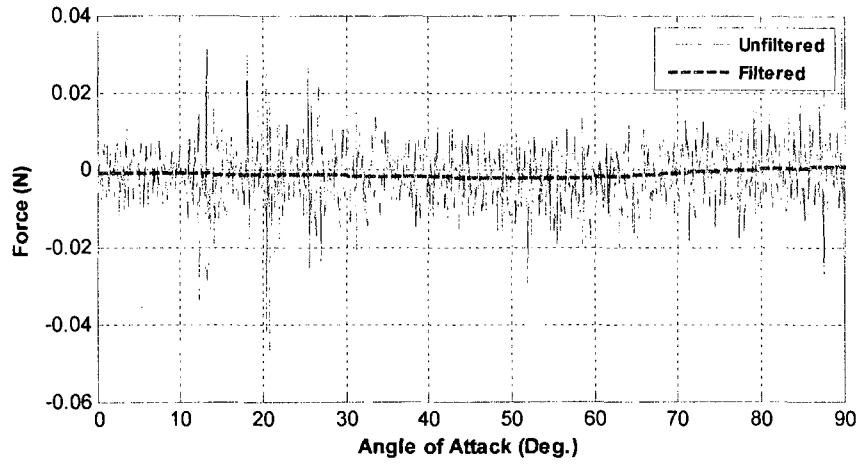
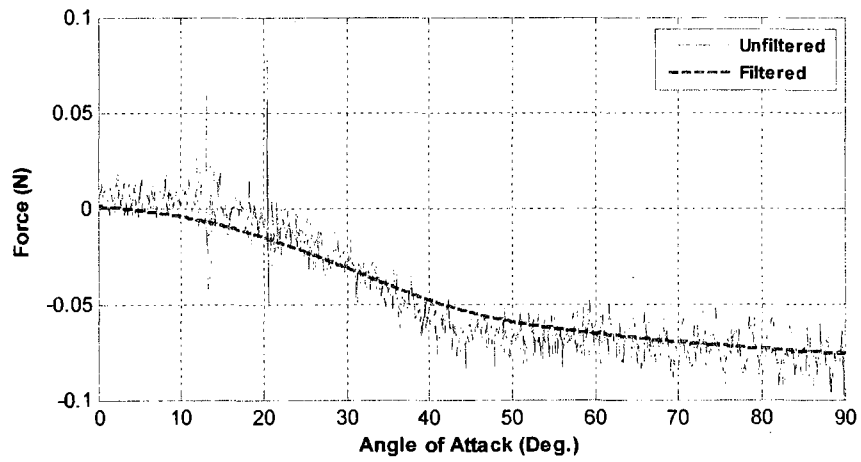Figure 6.15   Force Signal, F_x, for Dynamic Wind Tunnel Testing

Figure 6.16   Force Signal, F_y, for Dynamic Wind Tunnel Testing
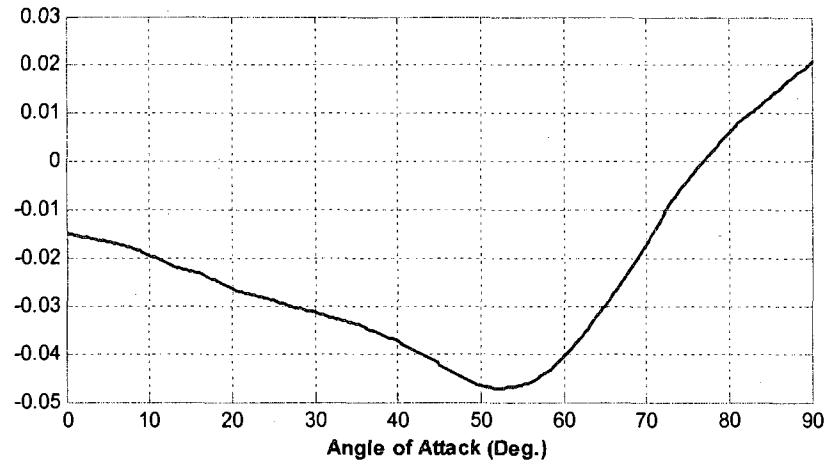
Figure 6.17   Coefficient of Axial Force, C_a, from 0-90° Angle of Attack for Dynamic

Wind Tunnel Simulation
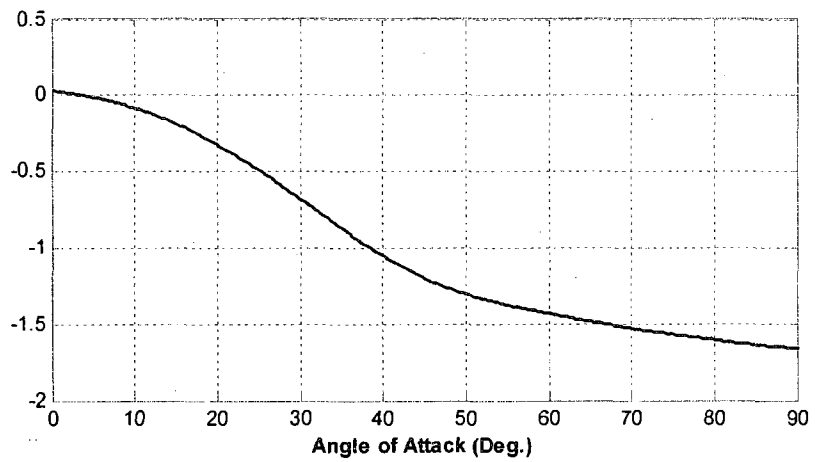
Figure 6.18   Coefficient of Normal Force, C_n, from 0-90° Angle of Attack Dynamic

Wind Tunnel Simulation

6.5.2 Coefficients of Lift and Drag

The coefficients of axial, C_a, and normal force, C_n, can be transformed into the lift and drag coefficient, C_l and C_d, for dynamic testing as computed previously using Equations 6.5 and 6.6. Figure 6.19 shows the coefficient of lift, C_l, and drag, C_d, for dynamic wind tunnel simulation.
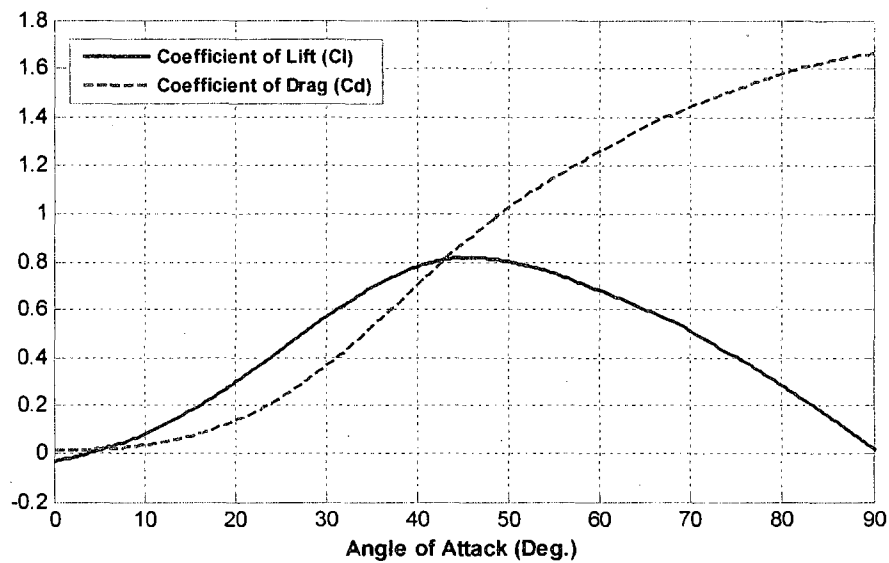
Figure 6.19   Coefficient of Lift, C_l, and Drag, C_d, for 0-90° Angle of Attack

The following analysis can be made about the aerodynamic coefficients for the wing at varying angle of attack under dynamic conditions.

- Both C_l and C_d start from near zero at 0° angle of attack. There should be no lift and minimal drag at this wing position as detailed previously.

- Increase in both lift and drag is seen with transition to 45° angle of attack. The lift and drag forces should increase as the angle of attack increases producing more significant aerodynamic forces.

- The lift starts to plunge into decline at about 45° angle of attack as compared to 40° for quasti-static testing indicating a greater stall angle. The stall angle under these conditions should is higher as expected because of delayed stall induced by dynamic change in angle of attack.

- The drag continues to increase and becomes the dominant aerodynamic component as the wing transitions past 45° angle of attack. The increased surface area exposure to the free stream velocity is responsible for the increase drag as it progresses to 90° angle of attack as indicated in Figure 6.3.

- The coefficient range is higher for drag and almost similar for lift for dynamic testing. Differences in magnitude can be a result of vortices, which are unavoidable with wind tunnel testing of a finite wing.

6.5.3 Center of Pressure

The calculation of center of pressure, C_P, is made using the same assumptions as made for quasi-static testing. Using Equation 6.9, the location of C_P along the wing span-wise and chord-wise direction is plotted in Figure 6.20. A discontinuity is noticed in the location of C_P along both directions at 0 to 15° angle of attack, as explained in Figure 6.21. This discontinuity may be result of moment forces not accounted for in calculating C_P along both directions. Following the discontinuity, a similar trend is seen as compared to quasi-static testing, Figure 6.12, with shift from quarter-chord to near half-chord location of C_P.

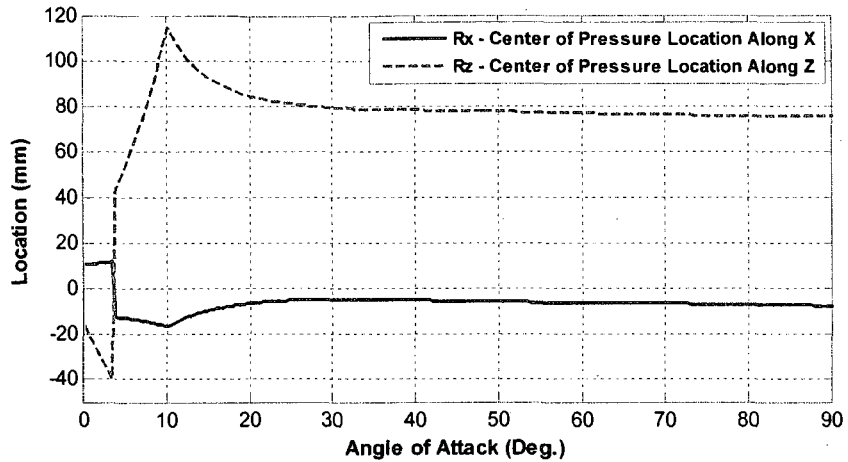Figure 6.20   Change in Center of Pressure, C_P, in Chord-wise and Span-wise Direction

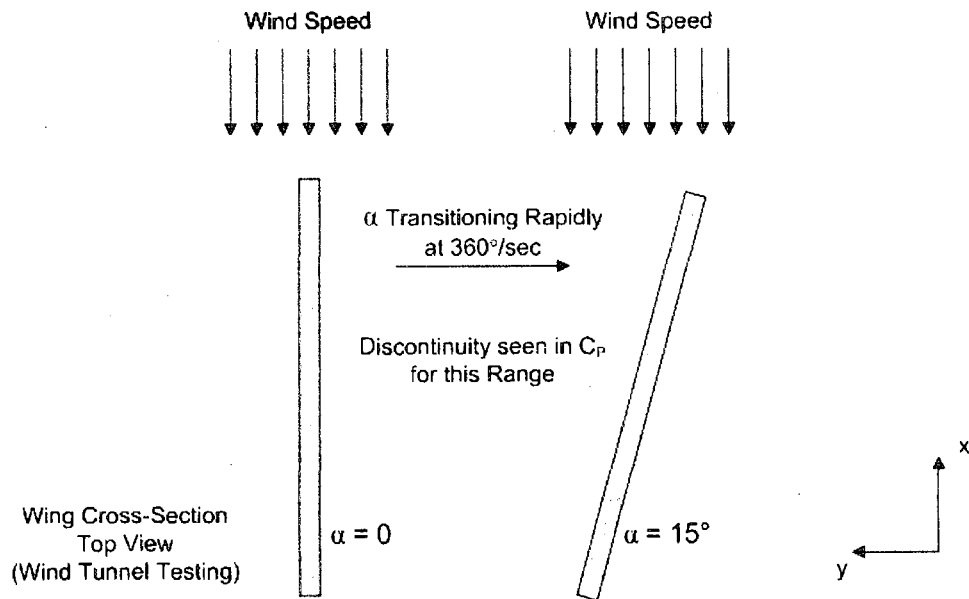for 0-90° Angle of Attack, Dynamic Testing

Figure 6.21   Discontinuity in C_P for Dynamic Change in Angle of Attack

6.6 CFD Comparison

A comparison of wind tunnel testing results can be made with those obtained from

CFD testing to determine the validity of both. Similar trends in C_l and C_D can signify

whether results obtained from wind tunnel testing and CFD modeling can be integrating into an aerodynamic model to better predict the aerodynamic performance of Figure-8 flapping motion. The development of a 2D static CFD model is discussed in Appendix D. Figure 6.22 and 6.23 displays the results pertaining to CFD and wind tunnel testing.

Figure 6.22   Coefficient of Drag, C_d, Determined by CFD Modeling, Appendix D, and

Wind Tunnel Testing

The following assessment can be made with comparing C_d obtained from wind tunnel testing results to CFD results.

- Coefficient of Drag, C_d

    o   Good correlation is seen with dynamic and quasi-static wind tunnel testing with CFD as both start and peak at the same angle of attack.

    o   The magnitude of CFD is peaks at 1.3 as compared to 1.6 and 0.9 for dynamic and quasi-static testing.

    o   Generally, the same trend is seen with all testing results.
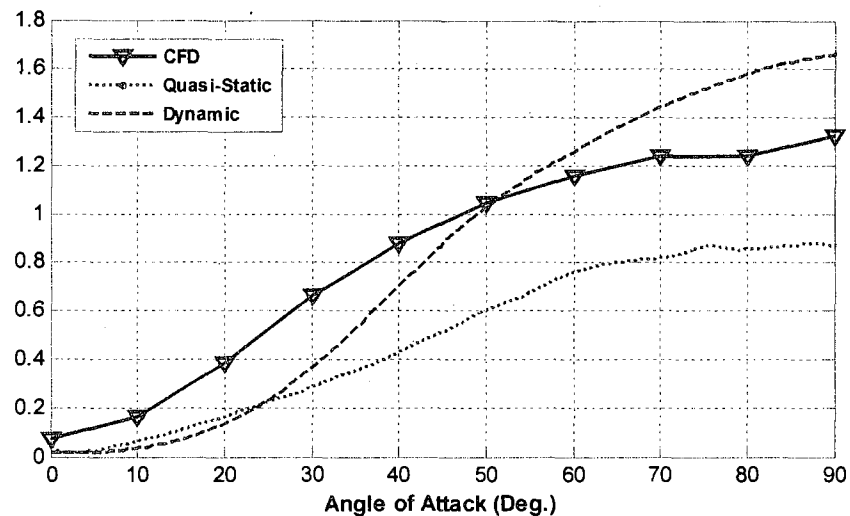
85
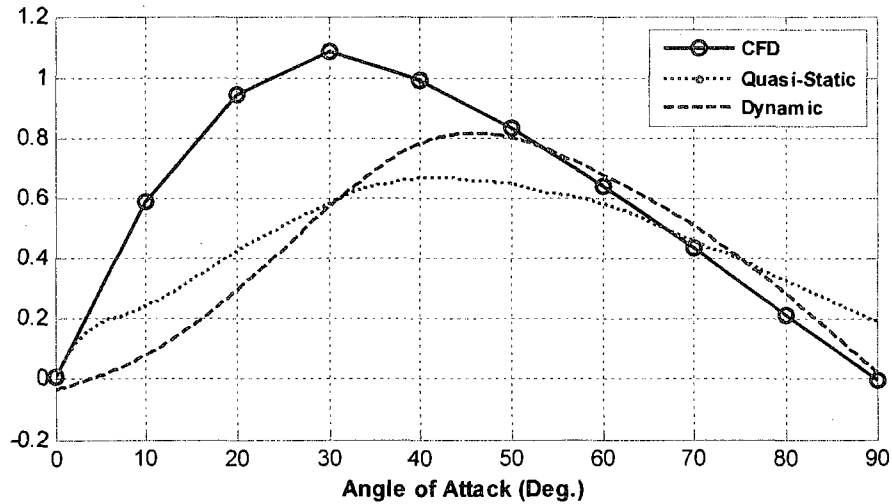
Figure 6.23   Coefficient of Lift, C_l, Determined by CFD Modeling, Appendix D, and

Wind Tunnel Testing

The following assessment can be made with comparing C_l obtained from wind tunnel

testing results to CFD results.

- Coefficient of Lift, C_l

    o From all testing, C_l, is initially zero and increases until the stall angle.

    o A stall angle of 30° is indicated by CFD, 40° by quasi-static testing, and

    45° by dynamic testing. The steady increase in stall angles with testing

    type exhibits that air flow detachment at the upper surface steadily

    increases by increasing the rate of change in angle of attack.

    o The lift is higher in CFD testing as compared to wind tunnel testing. The

    use of an infinite wing in CFD provides ideal results which cannot be

    reproduced in wind tunnel testing because of airflow around or above the

    wing tip of a finite wing.

CHAPTER 7

PROTOTYPE TESTING RESULTS

7.1 Force Signal Analysis

To access the total induced forces, inertial and aerodynamic, by Figure-8 spherical motion, an analysis of each force component will be presented. The results in this chapter pertain to 12.25 Hz testing. The experimental data collected data is filtered as outlined in Chapter 5. These results will be presented as a comparison to those of a model created in SIMULINK® SimMechanics, which account for the dynamic and predicted aerodynamic forces generated at this flapping frequency, Appendix C. To avoid any discrepancy in comparing experimental and model results, the actual output velocity for each prototype test is integrated into the model.

7.2 Signal Filtering at 12.25 Hz

The experimental force signal has excessive noise that needs to be filtered for proper analysis and interpretation. Dominant frequencies present are classified using Fast Fourier Transform technique, FFT, for digital signal processing. The force signal is then filtered using a Butterworth filter low pass filter applied at a cutoff frequency. For experimentation at 12.25 Hz, a cutoff frequency of 50 Hz determined by the FFT, which indicated minimal magnitude for frequencies beyond 50 Hz, Appendix E. The filtering eliminated noise that would distort the overall results. A sample of the filtered and

unfiltered force signal for the chord-wise direction, F_x, and the normal direction, F_y, is shown in Figures 7.1 and 7.2 respectively. Following the signal filtering process, each force component is compared to that generated by a model for Figure-8 spherical motion flapping. The main components of interest are the chord-wise force, F_x, and normal force, F_y, which have both inertial and aerodynamic components present.
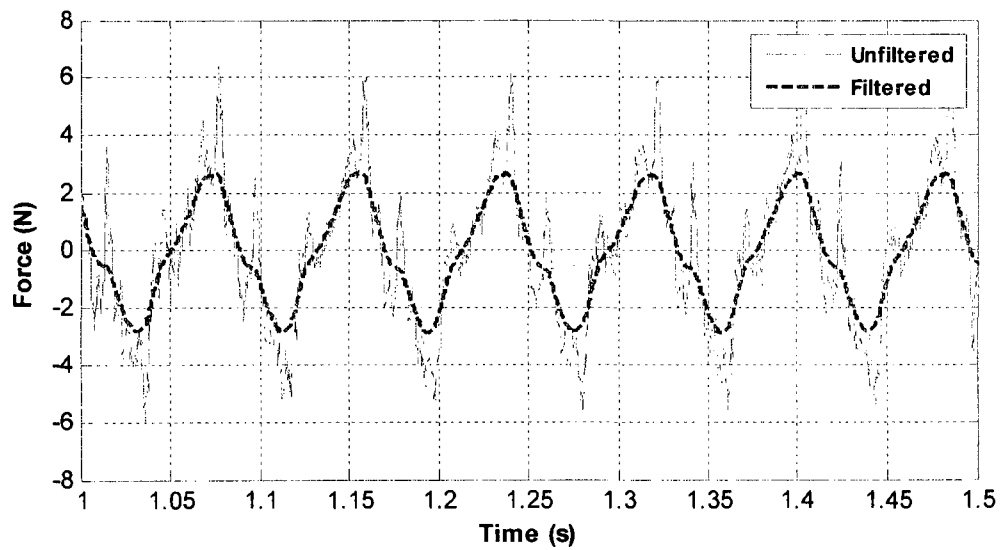

Figure 7.1   Unfiltered and Filtered Force Signal for Chord-wise Force, F_x, at 12.25 Hz
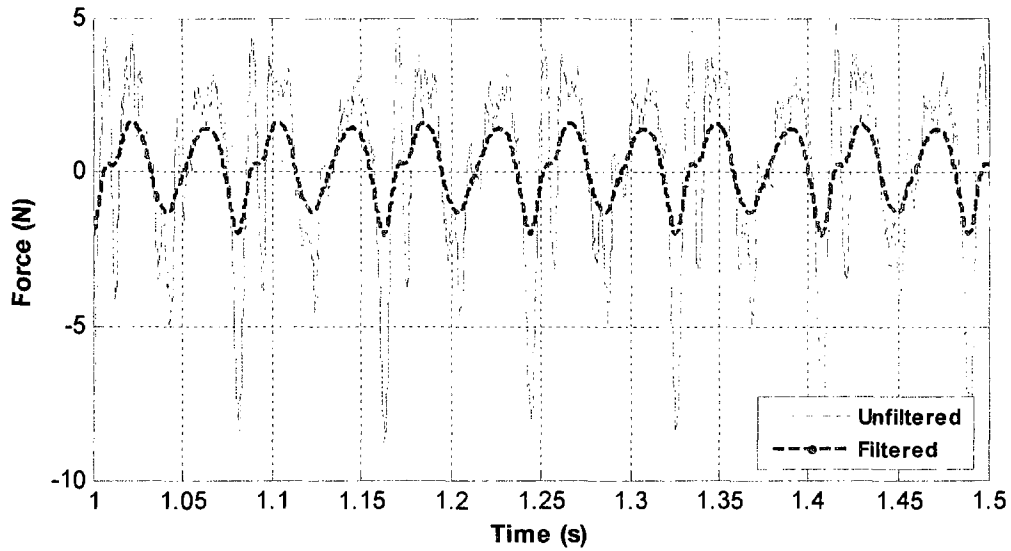
Figure 7.2   Unfiltered and Filtered Force Signal for Normal Force, F_y, at 12.25 Hz

7.3 Force Plots at 12.25 Hz

7.3.1 Chord-wise Force, F_x, at 12.25 Hz

The chord-wise component of the force signal, F_x, represents inertial forces generated with the wing cycling through the Figure-8 trajectory and aerodynamic components induced by drag. In addition, wing deformation can also be present in the signal at this frequency. The absence of airflow velocity with the wing fixed in air induces drag parallel to the free stream velocity induced by wing motion. Therefore, aerodynamic presence in F_x is simply due to drag and limited to approximately 10% of the signal.
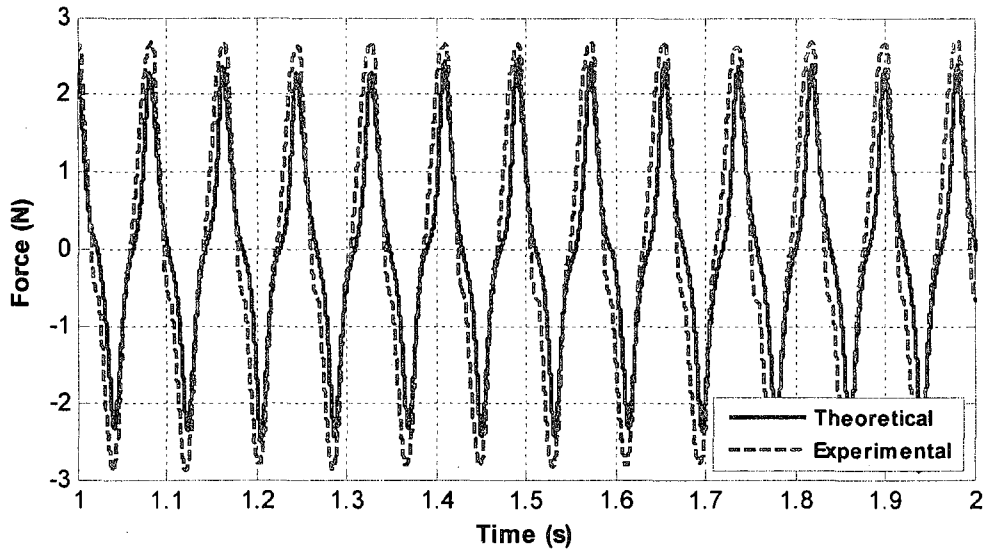
Figure 7.3 Chord-wise Force, F_x, at 12.25 Hz

The following analysis can be made from Figure 7.3 which shows a comparison of F_x for experiment and model.

- Experimental Signal shows higher force magnitude. The higher force magnitude could be a result of wing deformation. Although the balsa wood wing is fairly rigid, bending and torsional affects can be present.

- Filtering of the experimental signal may not have completely mitigated the affect of frequencies that do not correspond to wing testing. However, a lower filtering frequency cutoff would also create a flattened signal that may eliminate the some of the aerodynamic and inertial forces.

- As the wing cycles to and from 0° angle of attack where it crosses zero, a deviation from the model and experiment is noticed. A sharper transition is seen in the experimental signal as compared the model. This may indicate an incorrect predication of the aerodynamic force near minimal angle of attack in the model.

90

7.3.2 Normal Force, F_y, at 12.25 Hz

Similar to the chord-wise force, the normal force, F_y, is an essential component of the for signal that indicates inertial forces and the aerodynamic performance of this motion as well. The inertial load dominates the signal and limits the aerodynamics to approximately 10%. Deformation is a contributing factor in this force component as a deviation in the Figure-8 trajectory, widened trajectory along with reference to the symmetry axis along the stroke plane, can create higher forces unlike the model. The absence of air flow induces aerodynamic lift present in the normal force signal as the lift force is perpendicular free stream velocity induced by wing. Figure 7.4 shows the resulting force signal of both the experimental prototype and model.
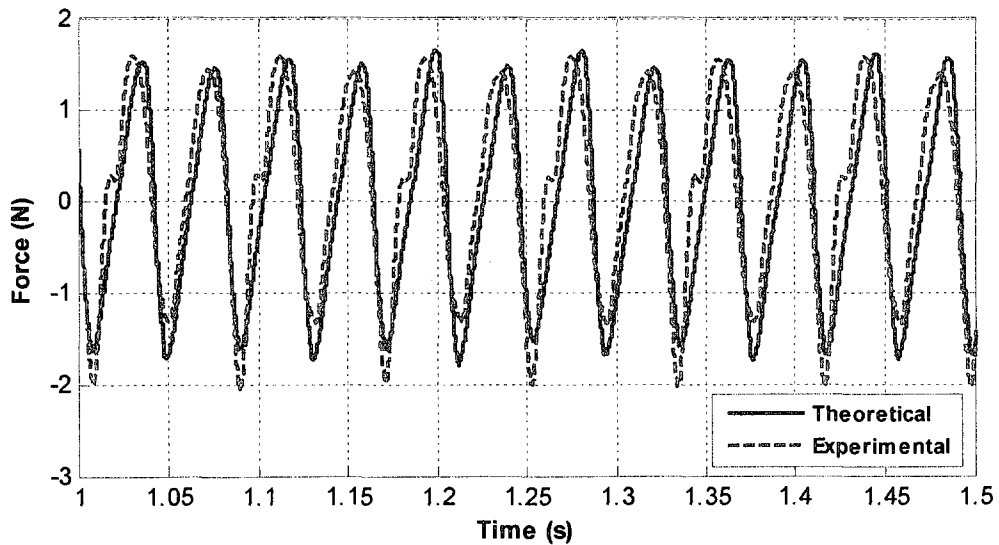

Figure 7.4   Normal Force, F_y, at 12.25 Hz

The following analysis can be made from Figure 7.4 which shows a comparison of F_y for experiment and model.

- Similar to the chord-wise force a deviation between both signals is seen as the force peaks in the negative y-direction. The higher magnitude during the initial upstroke can be a result of deformation in the Figure-8 trajectory. Factors contributing to deformation may include higher testing frequency, wing flexibility, and any joint looseness particular in the output and coupler hinge joint.

- The higher magnitude along the in the negative y-direction may also indicate the greater angular acceleration required to drive the mechanism during up-stroking motion. Little power and angular acceleration is required to transition from 0 – 90° angle of attack; however, the angular acceleration required once the wing has reached 90° angle of attack may have resulted in the higher force magnitude in the experimental signal.

- The predicted lift production accounted for in the model may have a limited contribution as compared to the experimental results.

- Similar to the chord-wise force, the filtering frequency cutoff may have not completed eliminated noise from the overall signal.

- Overall, aside from the minor difference between the experimental and model normal force, F_y, indicates matching signals

7.3.3 Span-wise Force, F_z, and the other Force Components

Span-wise force, F_z, induced by Figure-8 spherical motion is generated purely due to dynamics. The force represents centrifugal effects created with the wing in motion. With the wing fixed in air, no airflow, aerodynamic forces are not present in the span-wise force, F_z, as no association with the lift and drag forces can be made. However, the onset of airflow may present aerodynamic contribution to this force component. Figure 7.5

shows the span-wise force, F_z, at 12.25 Hz. As shown, although both results of the model and experimentation oscillate about an offset value, a much larger force is present during experimentation. The deviation in F_z is present due to any looseness or movement in the joints that induces a force in the span-wise during experimentation that cannot be reproduced in the model. On occasion, collected data for prototype that have been used extensively, has shown major force contributions in F_z force component further explaining the reason why it does not match with results of the model. A factor of noise that is present in all force components may also be indicated by experimental F_z. Nevertheless, this force component is given little significance as it does not affect the aerodynamic performance Figure-8 spherical motion flapping. In addition to Figure 7.5, the remaining force signal components for this testing are shown in the subsequent Figures. Overall, good correlation is seen in force magnitude, moments, moment magnitude with any divergence a reciprocal of the difference in the experimental and model span-wise force, F_z, and slight differences in F_x and F_y.
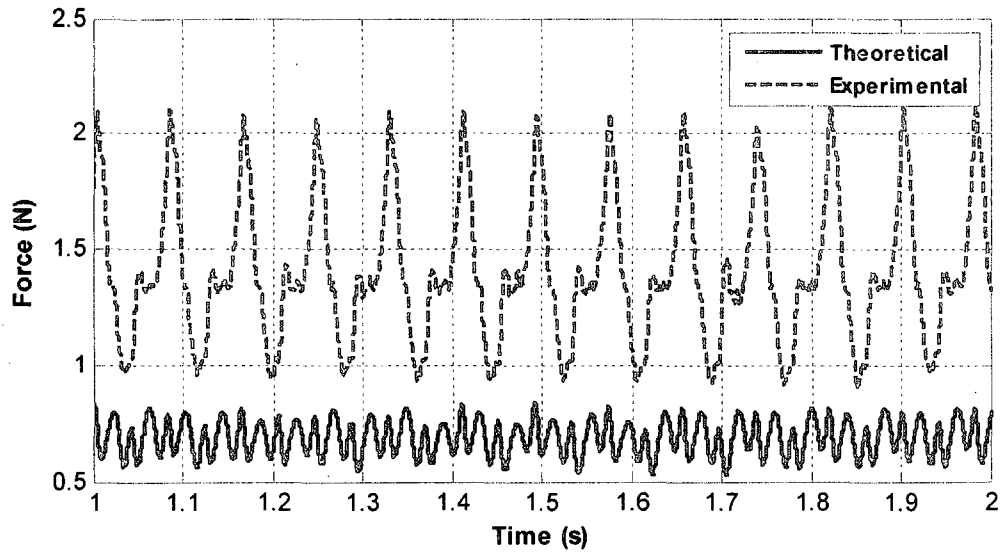
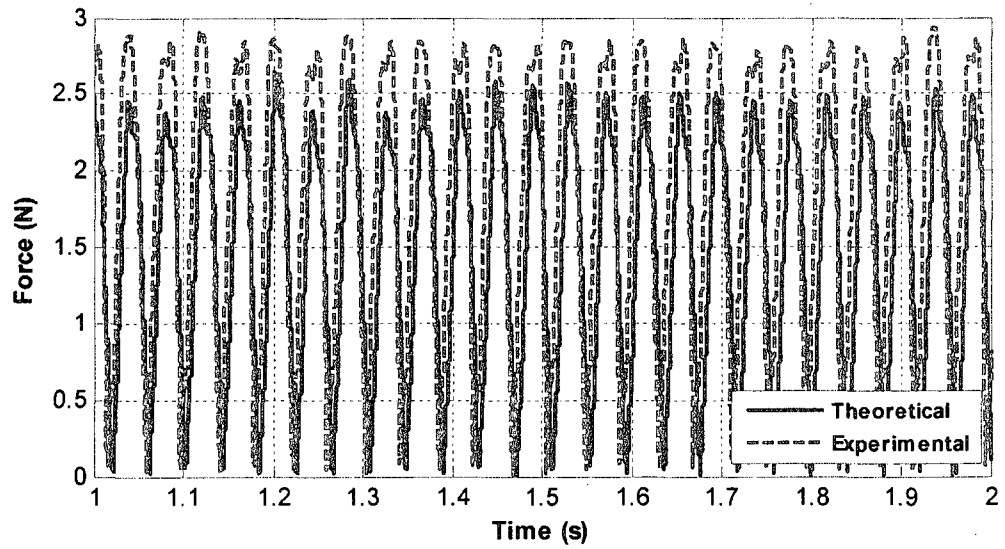Figure 7.5   Span-wise Force, F_z, at 12.25 Hz

Figure 7.6   Force Magnitude of Chord-wise, F_x, and Normal Force, F_y, at 12.25 Hz
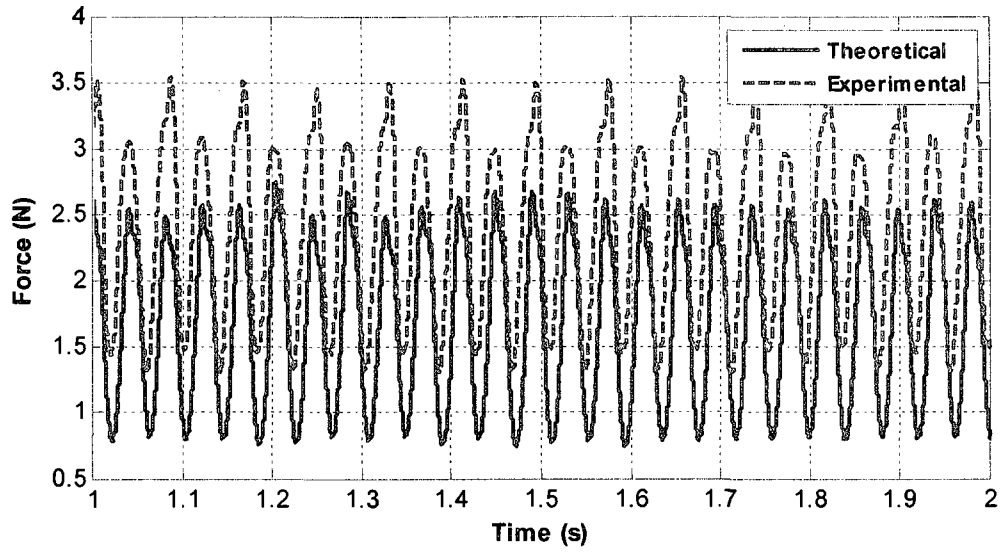
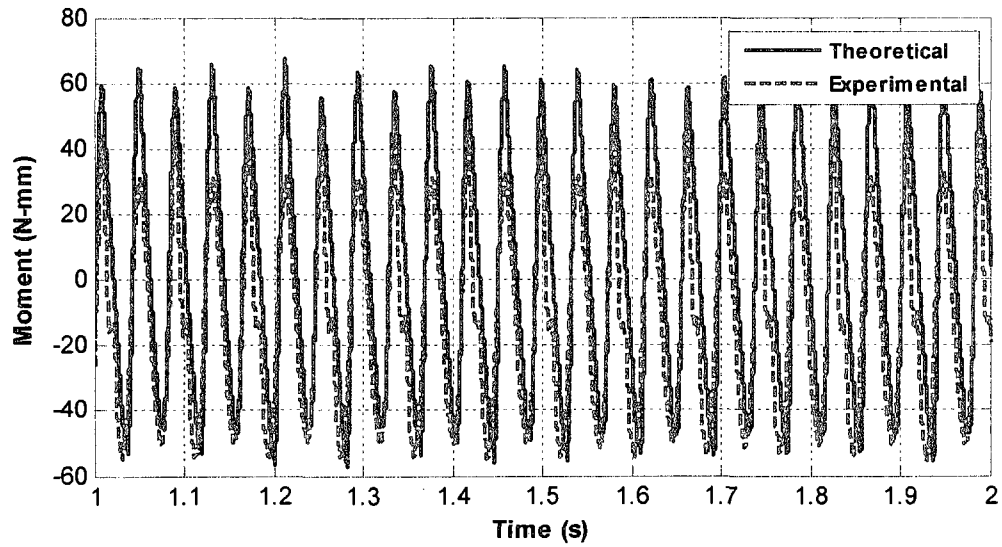Figure 7.7   Force Magnitude, *F*, at 12.25 Hz
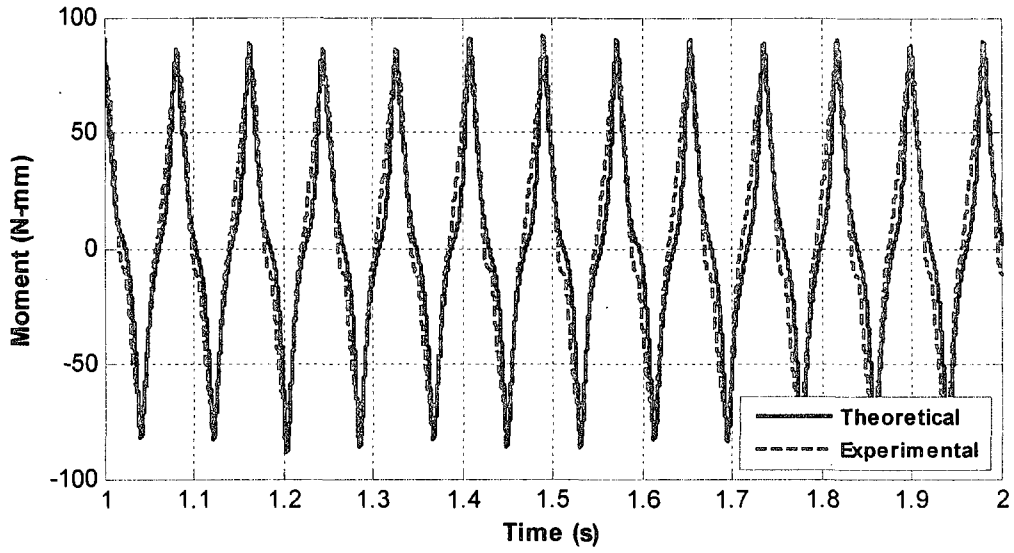

Figure 7.8   Moment, M_x, at 12.25 Hz

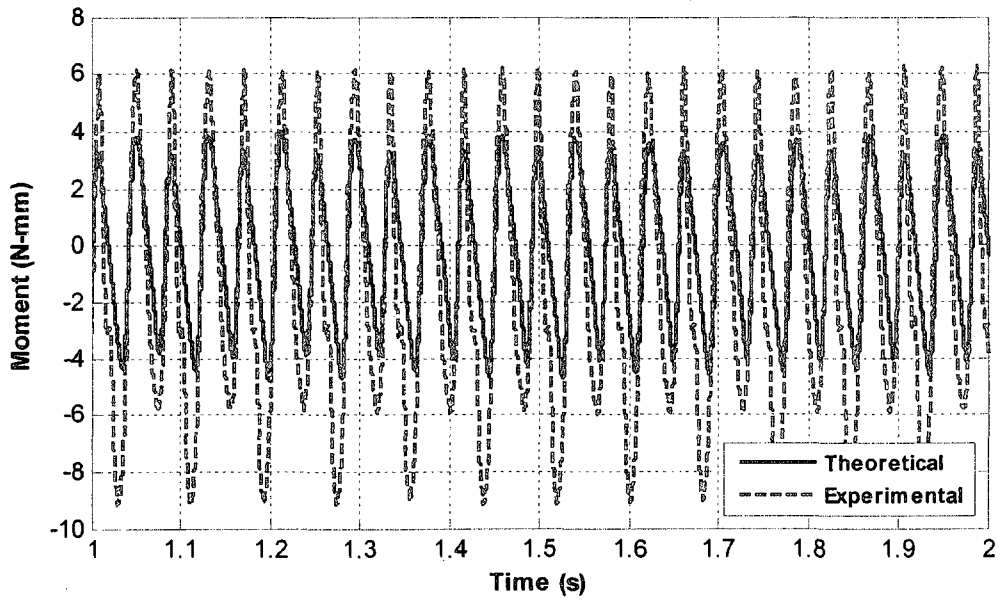Figure 7.9   Moment, M_y, at 12.25 Hz
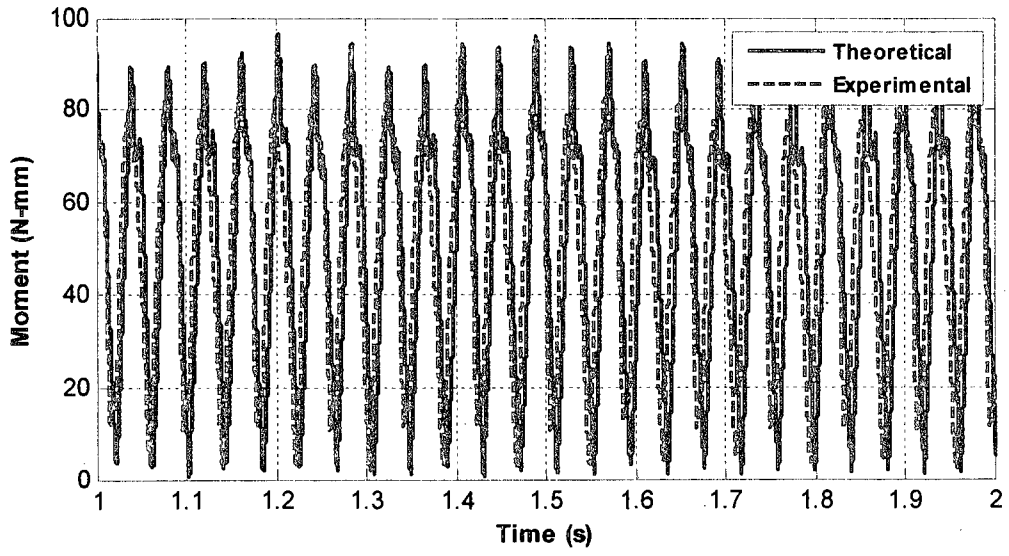

Figure 7.10   Moment, M_z, at 12.25 Hz

Figure 7.11   Moment Magnitude, *M*, at 12.25 Hz

CHAPTER 8

CONCLUSIONS

Figure-8 spherical motion accurately outlines a wing pattern commonly seen in nature particularly in hovering birds and insects. The integration of such a wing motion offers promising flight capabilities with potential application to future FWMAV design. The Figure-8 wing motion was achieved using a spherical four-bar mechanism which outlined the desired trajectory by attaching the wing to the coupler point. With this mechanism concept, a prototype was fabricated for testing at varying frequencies of 2.5 – 12.25 Hz to determine the induced forces by this motion pattern. The acquired force signal was compared to results of a model to determine the accuracy of both.

8.1 Spherical Four-Bar Mechanism Assessment

Flapping motion as seen in nature is generated by the shoulder joints of many birds and insects making them capable of creating various wing motions. In this research, a spherical four-bar mechanism that can mimic the function of a shoulder is successfully created. A spherical four-bar mechanism was synthesized to create Figure-8 spherical motion with two planes of symmetry. The synthesized spherical four bar mechanism can accomplish the desired wing trajectory with precise angular dimension assignment to each link. The mechanism provided a simple solution to reproducing this complex motion

exhibited in nature. The potential benefits of using a spherical four-bar mechanism for UAV design are outlined.

- The spherical four-bar mechanism can generate various wing trajectories with manipulation of the link angular dimensions. A distorted or asymmetrical Figure-8 is attainable to more precisely model in accordance with hummingbird flight. The various coupler-curves created with assignment of different angular dimensions gives leeway in manipulation of the mechanism.

- Ability of this mechanism to be used in various class sizes for UAV integration. The coupler-curve generated is not dependent on the size of the greater sphere the mechanism occupies; therefore, the size of the overall sphere can be enlarged or designed for micro application with meticulous manufacturing practices. The only requirement is that for symmetrical Figure-8 trajectory, for which conditions specified in Chapter 3 must be satisfied.

8.2 Design and Motion Verification

The conceptual spherical four-bar mechanism was designed and fabricated such that a wing could be attached to the coupler point. The wing attachment to the mechanism would ensure feasibility of the design and verify the motion pattern. The fabricated prototype was tested at various frequencies to determine accurate motion trajectory and acquire force signals induced by this motion. From the prototype testing conducted, the motion pattern was verified using still imagery and motion tracking. The motion pattern resembled the desired wing motion desired and indicated that a spherical four-bar

mechanism could be used to generate motion about a shoulder joint as seen in nature. Advantages of the prototype fabricated included the following.

- Links were designed to have minimal mass. The design of each link ensured the mass is likely to be limited regardless of the material use. This will minimize power requirements to drive this mechanism. In this case, the purpose was to prove concept of the mechanism and its applications; therefore, aluminum was used.

- Flat surfaces were incorporated into the design of the links for easy connection and no interference between links. Additionally, space allocation between each link and permanent hinge joints created with rivets, brass sleeves, and Teflon rings ensured longevity with limited friction.

- A base was used in place of an input link to enable prototype testing. The base was attached to an aluminum rod to collect force signals and conduct motion verification experiments.

- A light weight balsa wood wing was used for prototype testing. The balsa wing had a limited mass of 3.2 grams further reducing the load on the drive motor. The minimal mass of the wing also reduced inertial force contribution in the acquired force signal.

- The minimal mass enabled testing speeds of up to 12.25 Hz. Considering the conceptual nature of this research, the speeds reached provided valuable insight on the forces produced by this motion.

8.3 Potential Flight Characteristics of Figure-8 Motion

Any practical application is meaningless without a grasp of the potential flight capability of the designed flapping motion pattern. The aerodynamic performance is dependent primarily on the lift and drag forces associated with the motion and the location along the chord length where they are present, C_P. Wind tunnel testing provided significant information on the lift and drag variation at quasi-static and dynamic change of angle of attack. The results obtained can be incorporated into a model to better predict the aerodynamic forces induced by this motion. Furthermore, results were compared to CFD data that ensured proper analysis of the wind tunnel testing results. The results indicated a reasonable correlation between wind tunnel testing results with any difference created by the unknown effect of vortices encountered in the wind tunnel unverifiable by CFD. Overall, both methods provided a clear indication of how airflow around the wing behaves when cycling through its Figure-8 spherical motion pattern.

8.4 Prototype Testing Evaluation

Force signal analysis of the extensive experimentation conducted on the fabricated prototype at various frequencies provided the forces induced by Figure-8 spherical flapping motion. The results of each test were compared to that of a model and at each testing frequency showed good correlation. Any deviation in the force signal comparisons may be a result of factors that are explained in Chapter 7. The good correlation between both model and experimental prototype also accomplishes a validation of the model through prototype testing experimentation. Nevertheless, this testing technique can serve as a verification method to create a more accurate model.

8.5 Future Work

Integrating a spherical four-bar mechanism in FWMAV design requires additional techniques to create a more applicable design and prototype. An appropriate design that encompasses two wings, more advanced manufacturing process for a more feasible prototype, and sufficient power production for sustainable flight are primary design objectives that need to be addressed.

Design of a mechanism that uses two spherical four-bar mechanisms to drive two wings is essential component that needs to be accomplished prior to FWMAV application. An ideal design would incorporate both mechanisms using some sort of shoulder connection and be capable of being driven by a single motor. The use of a single motor would limit the overall mass of such a prototype and more net lift can be generated. Limiting mass must also be accomplished by lighter links. The use of material is vital is minimizing the mass and power requirement. These design enhancements increase the prospective of more efficient use of aerodynamic forces for more a probable flight and hover. Mass reduction of the links and wing can be accomplished with the use of composite materials. The minimal power requirement will establish more practical designs. Additionally, the minimal mass of the wing can yield enhanced experimentation by allowing the extraction of aerodynamic forces from acquired load cell data quantifying the actual aerodynamic forces.

Other work that would institute a perfected design includes developing a 3D dynamic CFD model, a full dynamic model based on a double wing FWMAV prototype, and generate control algorithms that would accomplish basic flight tasks. A 3D CFD model

would precisely predict the aerodynamic characteristics of Figure-8 spherical flapping motion. A full dynamic model would help determine the forces generated with the inclusion of two wings, the results of which could be compared to an actual double wing prototype. Lastly, a controller design to allow hovering, maneuverability, and feasibility with respect to nature and application purposes will perfect this design.

REFERENCES

[1]   Ellington, C., "The Aerodynamics of Hovering Insect Flight. I. The Quasi-Steady Analysis," Philosophical Transactions of the Royal Society of London. Series B, Biological Sciences, Vol. 305, No. 1122, pp. 1-15, 1984.

[2]   Shyy, W., Berg, M., and Ljungqvist, D., "Flapping and flexible wings for biological and micro air vehicles," Progress in Aerospace Sciences, Vol. 35, pp.455-505, 1999.

[3]   Ellington, C., "The novel aerodynamics of insect flight: applications to micro-air vehicles," The Journal of Experimental Biology, Vol. 202, pp. 3439–3448, 1999.

[4]   Zibikowski, R., Knowles, K., Pedersen, C., and Galinski, C., "Some aeromechanical aspects of insect-like flapping wings in hover," Proc. Institute of Mechanical Engineers Vol. 218 Part G: J. Aerospace Engineering, pp. 389-398, 2004.

[5]   Zibikowski, R., Galinski, C., and Pedersen, C., "Four-Bar Linkage Mechanism for Insectlike Flapping Wings in Hover: Concept and an Outline of Its Realization," Journal of Mechanical Design. Vol. 127, pp 817-824, 2005.

[6]   Galinski, C. and Zibikowski, R., "Insect-like flapping wing mechanism based on a double spherical Scotch yoke," J. R. Soc. Interface, No. 2, pp. 223–235, 2005.

[7]   Banala, S. K. and Agrawal, S. K., "Design and optimization of a mechanism for out-of-plane insect winglike motion with twist," Journal of Mechanical Design. Vol. 127, pp 841-844. 2005.

[8]   McIntosh, S. H., Agrawal S. K., Khan, Z. A., "Design of a mechanism for biaxial rotation of a wing for a hovering vehicle," IEEE/ASME Transactions on Mechatronics. Vol. 11, pp. 145-153. 2006.

[9]   Madangopal, R., Khan, Z. A., and Agrawal, S. K., "Energetics-based design of small flapping-wing micro air vehicles," IEEE/ASME Transactions on Mechatronics, Vol. 11, pp. 433-438. 2006.

[10] Conn., A., Burgess, S., Hyde, R., and Ling, C., "From Natural Flyers to the Mechanical Realization of a Flapping Wing Micro Air Vehicle," Proceedings of the 2006 IEEE International Conference on Robotics and Biomimetics, pp. 439-444, 2006.

[11] Conn., A., Burgess, S., and Ling, C., "Design of a parallel crank-rocker flapping mechanism for insect-inspired micro air vehicles," Proc. IMechE Vol. 221, Part C: J. Mechanical Engineering Science, pp. 1211-1222, 2007.

[12] Khan, Z. A., and Agrawal, S. K., "Design and Optimization of a Biologically Inspired Flapping for Flapping Wing Micro Air Vehicles," IEEE Conference on Robotics and Automation, pp. 373-378, 2007.

[13] Dickinson, M. H., and Lehmann, F-O., Sane, S.P., "Wing rotation and the aerodynamic basis of insect flight," Science, Vol.284, pp.1954-1960, 1999.

[14] Sane, S. P., and Dickinson, M. H., "The aerodynamic effects of wing rotation and a revised quasi-steady model of flapping flight," Journal of Experimental Biology, Vol. 205, pp. 1087-1096, 2002.

[15] Singh, B., Ramasamy, M., Chopra I., and Leishman, J.G., "Insect-based flapping wings for micro hovering air vehicles: Experimental investigations," American Helicopters Society International Specialists Meeting on Unmanned Rotorcraft, 2004.

[16] Maybury, W. and Lehmann, F., "The fluid dynamic of flight control by kinematic phase lag variation between two robotic insect wings," The Journal of Experimental Biology, Vol. 207, pp. 4707-4726, 2004.

[17] Khan, Z. A., and Agrawal, S.K., "Force and moment characterization of flapping wings for micro air vehicle applications," American Control Conference, pp. 1515-1520, 2005.

[18] Khan, Z. A., and Agrawal, S. K., "Modeling and simulation of flapping wing micro air vehicles," ASME International Design Engineering Technical Conferences and Computers and Information in Engineering, pp. 1-9, 2005.

[19] Lehmann, F. and Pick, S., "The aerodynamic benefit of wing-wing interaction depends on the stroke trajectory in flapping insects," The Journal of Experimental Biology, Vol. 210, pp. 1362-1377, 2007.

[20] O., and Angeles, J., "Performance evaluation of path-generating planar, spherical and spatial four-bar linkages," Mechanism and Machine Theory, Vol. 23, pp. 257-268, 1988.

[21] Lu, D., and Hwang, W., "Spherical four-bar linkages with symmetrical coupler curves," Mechanism and Machine Theory, Vol. 31, pp. 1-10, 1996.

[22] Ruth, D., and McCarthy, J., "The design of spherical 4R linkages for four specified orientations," Mechanism and Machine Theory, Vol. 34, pp. 677-692, 1999.

[23] McCarthy, J., and Bodduluri, R., "Avoiding singular configurations in finite position synthesis of spherical 4R linkages," Mechanism and Machine Theory, Vol. 35, pp. 451-462, 2000.

[24] Alizade, R., and Kilit, O., "Analytical synthesis of function generating spherical four-bar mechanism for the five precision points," Mechanism and Machine Theory, Vol. 40, pp. 863–878, 2005.

[25] Hwang, W., and Chen, K., "Triangular nomograms for symmetrical spherical non-Grashof double-rockers generating symmetrical coupler curves," Mechanism and Machine Theory, Vol. 42, pp. 871–888, 2007.

[26] Duffy, J., "Analysis of mechanisms and robot manipulators," Wiley, New York, 1980.

[27] McCarthy, J., "Geometric Design of Linkages," Springer, Berlin, 2000.

[28] Erdman, A. G., and Sandor, G. N., "Mechanism design analysis and synthesis," Prentice Hall, New Jersey, 1997.

[29] Shigley, J. E., "Kinematic analysis of mechanisms," McGraw Hill, New York, 1969.

[30] "CRC Standard Mathematical Tables, 26th Edition," CRC Press, Boca Raton, 2000.

[31] Ketchel, J., and Larochelle, P., "Computer-aided manufacturing of spherical mechanisms," Mechanism and Machine Theory, Vol. 42, pp. 131–146, 2007.

[32] http://www.ati-ia.com/products/ft/ft_models.aspx?id=Nano17

[33] http://www.faulhaber-group.com/uploadpk/EN_2057B_MIN.pdf

[34] http://www.micromo.com/nl12782/i364354.html

[35] Larijani, R. F., and DeLaurier, J. D., "A nonlinear aeroelastic model for the study of flapping wing flight," AIAA Progress in Aeronautics and Astronautics, Vol.195, chap 18, pp. 399-428, 2001.

APPENDIX A

EQUATIONS OF MOTION FOR FIGURE-8 SPHERICAL MOTION

Duffy [26] presented the equations for a general spherical four-bar mechanism by splitting the quadrilateral into two spherical triangles. As mentioned earlier, Figure-8 motion of a coupler point can be achieved by creating a spherical four bar-mechanism with the following angular dimensions:

$$\alpha_{41} = \alpha_{12} = \alpha_{23} = \alpha_P = 90°$$

$$\theta_P = -90°$$

In this case, the generalized equations of can be reduced to:

$$\theta_1 = 2 \tan^{-1} \left(\frac{-\sin(\alpha_{34}) \sin(\theta_4) \pm \sqrt{1 - \sin^2(\alpha_{34}) \cos^2(\theta_4)}}{\cos(\alpha_{34})} \right) \tag{A.1}$$

The above equation produces two values of θ_1, each for one of the closures of the mechanism. Each value of θ_1 can be used to calculate the corresponding values of θ_2 and θ_3.

$$\theta_2 = 2 \tan^{-1} \left(\frac{\sin(\alpha_{34}) \sin(\theta_4) \cos(\theta_1) + \cos(\alpha_{34}) \sin(\theta_1)}{\sin(\alpha_{34}) \cos(\theta_4) + 1} \right) \tag{A.2}$$

$$\theta_3 = 2 \tan^{-1} \left(\frac{\cos(\theta_4) \sin(\theta_1)}{\cos(\alpha_{34}) \sin(\theta_4) \sin(\theta_1) + \sin(\alpha_{34}) \cos(\theta_1) + 1} \right) \tag{A.3}$$

APPENDIX B

HIGH SPEED CAMERA TESTING

To validate the simulation result of the dynamics of the Figure-8 motion pattern, video of the motion is captured using high speed stereo camera system and analyzed. Table B.1 shows the specification of the two high speed cameras. Figure B.1 shows the stereo vision setup to capture the wing motion.

Table B.1   Specifications of High Speed Camera

Item	Value
Maker	Vision Research Inc.
Model	Phantom v4.3
Resolution	800 x 600 pixels
Rate	1,000 frames per second

Figure B.1   High Speed Camera Stereo Vision Setup

The stereo camera calibration is performed to measure the intrinsic and extrinsic parameters of stereo camera. A total of seven left and right images of a planar checkerboard with 10 mm black and white squares were used. Figure B.2 is a snapshot of both the left and right calibration images. Table B.2 and Table B.3 shows the intrinsic and extrinsic parameters of left and right camera that indicate the position of right camera with respect to left camera. Actual designed distance between centers of lens is 120 mm and calibrated baseline distance is a reasonable value of 119.423 mm with 0.245 mm error. Forty-four light reflecting marks are placed on the wing. The marks are placed 10 mm apart as shown in Figure B.3. Figure B.4 shows the left and right image of stereo camera system which captures the Figure-8 wing motion.
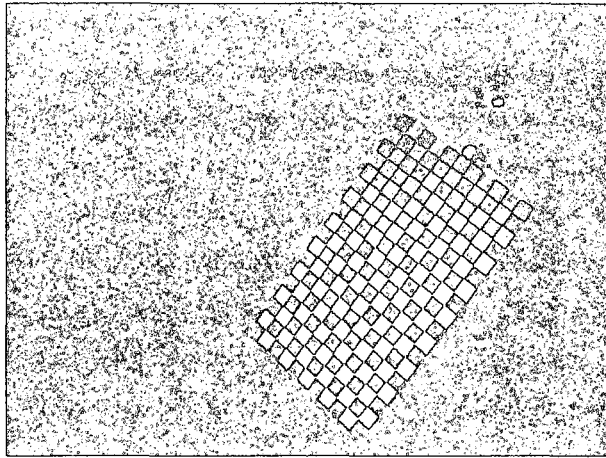
(A)
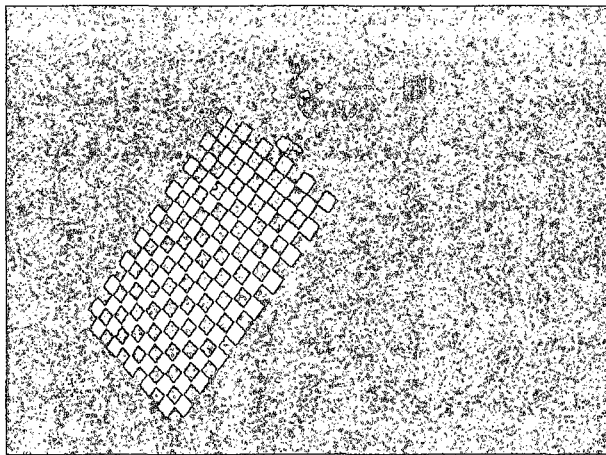
(B)

Figure B.2   Stereo calibration images (A) left camera image (B) right camera image

Table B.2   Stereo Camera Intrinsic Parameters

Parameters	Value
Left Camera Focal Length	[1173.634, 1172.916]+/-[3.870, 3.630] pixels
Left Camera Principal point	[373.847, 321.243]+/-[6.183, 6.205] pixels
Left Camera Distortion	[-0.324, 0.1317, -0.000, -0.005, 0.000]
Right Camera Focal Length	[1165.211, 1170.397]+/-[3.790, 3.206] pixels
Right Camera Principal point	[377.151, 322.301]+/-[6.218, 7.204] pixels
Right Camera Distortion	[-0.332, -0.025, 0.001, -0.001, 0.000]

Table B.3   Stereo Camera Extrinsic Parameters

Parameters	Value
Rotation Vector	[0.011, 0.002, 0.002]+/-[0.007, 0.007, 0.001] rad.
Translation vector	[-119.423, -0.699, 4.119]+/-[0.245, 0.151, 1.562] mm
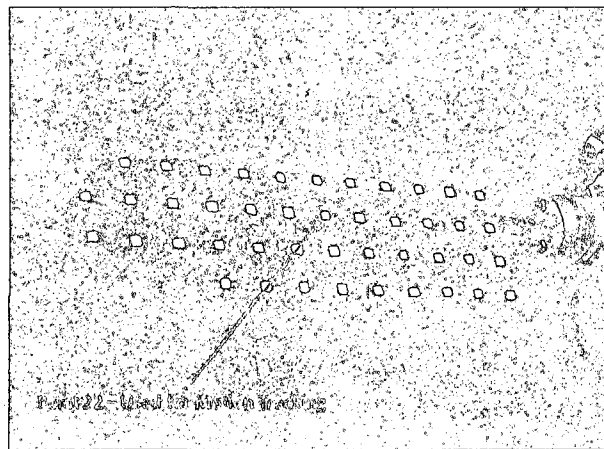
Figure B.3   Wing with Designated Points for Motion Tracking
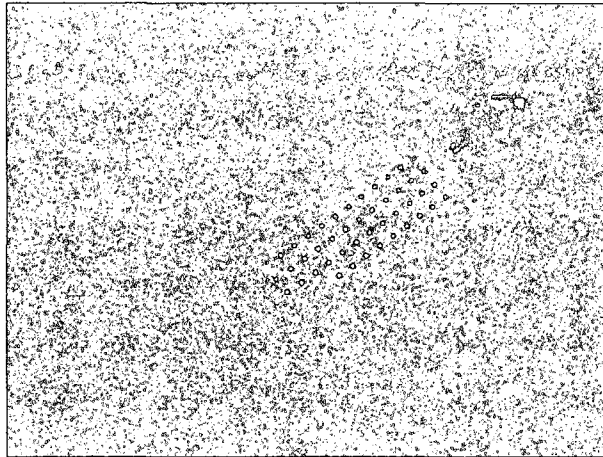
(A)

(B)

Figure B.4   Stereo wing motion images. (A) Left camera image, (B) right camera image

APPENDIX C

AERODYNAMIC MODELING

Defining the aerodynamics associated with Figure-8 flapping spherical motion required a thorough understanding of how the movement of air over the surface of the wing would act. As compared to fixed wing flight which has fixed angle of attack and uses propulsion to generate movement across the air, flapping motion exhibited by hummingbirds and insects, produce flight with its flapping wings. Therefore, rapid changes in direction, velocity induced by the wings, angle of attack, and phase of the motion are all distinct aerodynamic features that accomplish flight. In determining the aerodynamic model, [35] allows us to comprehend certain characteristics to account for in flapping wing flight. With modifications made for spherical motion, theory discussed in [35] is employed into to our model to determine the aerodynamics produced by this motion.

C.1 Defining Induced Free-stream Velocity

The free stream velocity generated by Figure-8 flapping motion is defined as the velocity induced over on the wing acting tangent to the wing trajectory as shown in Figure C.1. This definition holds for any flapping motion as long as the system's position is held constant or fixed at a single location. Therefore, the induced velocity for any point on the subdivided section on the wing, P_i, is defined in Equation C.1.
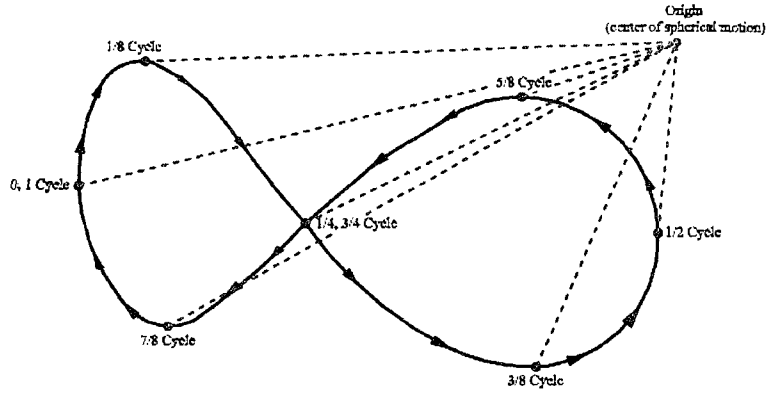
Figure C.1   Wing Point Trajectory & induced velocity

$$\bar{U}_i = \frac{d\bar{P}_i}{dt} \tag{C.1}$$

Components of the free-stream velocity vector U_i, exist in x, y, and z coordinates due to the wing's arched trajectory generated by the spherical mechanism driving the wing's motion.

$$\bar{U}_i = (U_{x,i}, U_{y,i}, U_{z,i}) \tag{C.2}$$

The free-stream velocity is defined as the magnitude of this vector.

$$|U_i| = \sqrt{U_{x,i}^2 + U_{y,i}^2 + U_{z,i}^2} \tag{C.3}$$

$$U_i = |U_i| \tag{C.4}$$

C.2 Projection of the Free-stream Velocity onto the Wing,(V_n & V_a)

An edge vector, R_i, is then defined along the chord-wise direction of the wing.

$$\bar{R}_i = [R_{x,i}, R_{y,i}, R_{z,i}] \tag{C.5}$$

This edge vector was normalized by dividing the vector components by the magnitude.

$$|R_i| = \sqrt{R_{x,i}^2 + R_{y,i}^2 + R_{z,i}^2} \tag{C.6}$$

$$\vec{R}_{N,i} = \frac{\vec{R}_i}{|R_i|} \tag{C.7}$$

The free-stream velocity, U_i, was then projected into the surface of the wing by taking the dot-product of the normalized edge vector, $R_{N,i}$, along the wing and the free-stream velocity vector, U_i, as shown in Figure C.2.

$$V_{a,i} = \vec{U}_i \cdot \vec{R}_{N,i} = (R_{x,i} \cdot U_{x,i}) + (R_{y,i} \cdot U_{y,i}) + (R_{z,i} \cdot U_{z,i}) \tag{C.8}$$
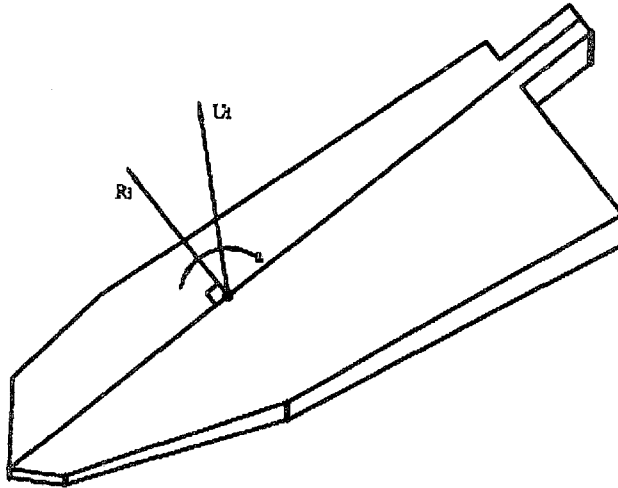
Figure C.2   Induced wing velocity projection

This dot-product projection of the free-stream velocity was used to determine the velocity acting normal to the wing, $V_{n,i}$.

$$V_{n,i} = |Ui|\sin(\alpha') \tag{C.9}$$

The work presented here is based on the assumption that the wing acts as a perfectly rigid body. This assumption was made as a simplification to the experimental model. The wing used on this study is based on scaling the forewing of a dragonfly as presented in

[16], has a slightly tapered thickness. The irregular shape associated with the wing profile used in the model makes it particularly difficult to integrate the aerodynamic forces that act upon it. Therefore, it is approximated by i rectangular sections of uniform thicknesses. To eliminate the wing's shape complexity, the wing span area was subdivided into six equal span length areas. In order to approximately represent the wing's actual area at the locally subdivided span length, L_i, the chord length, c_i, of these rectangular sections were chosen. As shown in Figure C.3, this approximation holds that the subdivided span area of each subdivided rectangle equals that of the actual models span area over the locally subdivided span length.
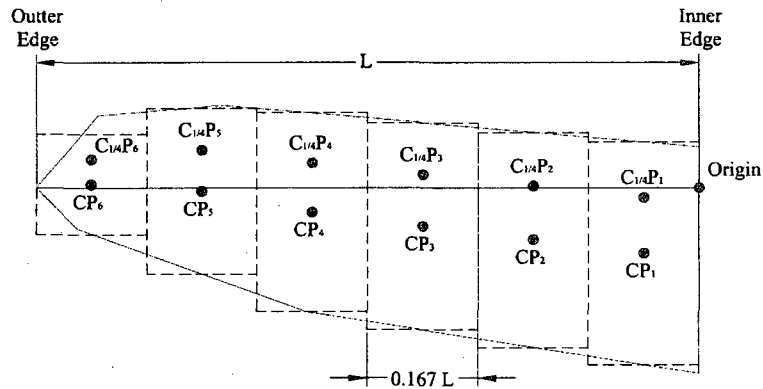
Figure C.3   Approximate Wing-Sub Area Divisions

The centers of these rectangles, used as the point of measurement for the induced velocity on the local wing subdivided area, were chosen to be at the mid-chord length and the mid-span length of each subdivided rectangular section. With the wings coordinate system being defined at the inner edge of the wing and center to the mounting point.

$$CP_i(x,y) = \left(\frac{L_i}{2}, \frac{c_i}{2}\right) \qquad\qquad (C.10)$$

116

In a similar fashion, the quarter chord point of these rectangles, used as the point of application of the aerodynamic resultant force on the local wing subdivided area, were chosen to be at the quarter-chord length from the leading edge and the mid-span length of each subdivided rectangle.

$$C_{1/4}P_i(x,y) = \left(\frac{L_i}{2}, \frac{c_i}{4}\right)$$ (C.11)

It is assumed that the resultant of the aerodynamic forces acts at the quarter-chord length of each sub-divisional area. This assumption was based on the center of pressure, C_P, being approximately located at the quarter chord location as understood in thin airfoil theory.

C.3 Derivation of Aerodynamic Forces

For the model, partial leading-edge suction, vortex wake effects, and post-stall behavior were accounted for along the wing's sectional profile. The resultant forces obtained from this model were then applied to the quarter-chord point of each subdivided area and measured at the same point of reference as the experimental model. To begin the study of the aerodynamic forces, a division was made to separate the forces occurring during attached and detached flow. Figure C.4 shows all the aerodynamics forces with respect to the wing cross-section.
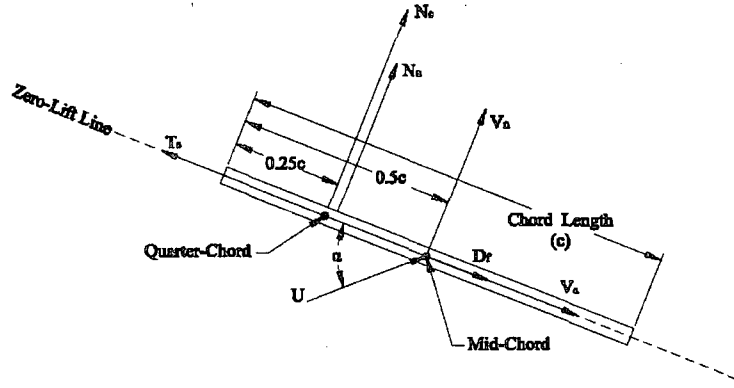
Figure C.4   Wing Section Aerodynamics forces and motion variables

C.4 Attached Flow

The aerodynamic resultant force acting at the quarter chord point is given by,

$$R_{A,i} = R_{n,i} + R_{a,i} \qquad (C.12)$$

where $R_{n,i}$ is the resultant force normal to the wing profile and $R_{a,i}$ is the resultant force in the chord-wise direction of the wing. The resultant force normal to the wing profile is given by,

$$R_{n,i} = N_{c,i} + N_{a,i} \qquad (C.13)$$

where $N_{c,i}$ is the circulatory normal force and $N_{a,i}$ is the apparent-mass normal force. The resultant force in the chord-wise direction is given by,

$$R_{a,i} = T_{s,i} - D_{f,i} \qquad (C.14)$$

where $D_{f,i}$ is the viscous drag force due to skin friction and $T_{s,i}$ is the leading-edge suction force. The circulatory normal force is given by,

$$N_{c,i} = \frac{1}{2} \rho U_i V_{a,i} C_n c_i l_i \qquad (C.15)$$

where, ρ is the density of air at standard pressure,

U_i is the free-stream velocity,

118

$V_{a,i}$ is the free-stream velocity component in the chord-wise direction of the wing,

C_n is the normal force coefficient,

c_i is the chord length, and

l_i is the span length of the particular subdivided rectangle.

The apparent-mass effect normal force is given by,

$$N_{a,i} = \frac{1}{4}\rho\pi c_i^2 U_i \dot{\alpha}' l_i \tag{C.16}$$

where $\dot{\alpha}'$ is the change in the angle of attack with respect to the change in time. The viscous drag force is given by

$$D_{f,i} = C_a \frac{\rho V_{a,i}^2}{2} c_i l_i \tag{C.17}$$

where C_a is the force coefficient in the chord-wise direction of the wing profile. The leading-edge suction force is given by

$$T_{s,i} = \eta_s 2\pi \left(\alpha'\right)^2 \frac{\rho U_i V_{a,i}}{2} c_i l_i \tag{C.18}$$

where η_s is the leading-edge suction efficiency which is assumed to be 0.5.

C.5 Detached (Stalled) Flow

The wing profile transitions into a stall condition when the angle of attack increases between the free stream velocity and the wing's sectional profile, thus causing the flow to detach from the upper surface of the wing creating turbulent vortices. This flow detachment will progress until it has reached the leading edge of the wing at which point stall occurs. The aerodynamic resultant force is given by,

$$\left(R_{A,i}\right)_{stall} = \left(R_{n,i}\right)_{stall} + \left(R_{a,i}\right)_{stall} \tag{C.19}$$

where $(R_{n,i})_{stall}$ is the resultant force normal to the wing profile and $(R_{a,i})_{stall}$ is the resultant force in the chord-wise direction of the wing. The resultant force normal to the wing profile is given by,

$$(R_{n,i})_{stall} = (N_{c,i})_{stall} + (N_{a,i})_{stall} \qquad (C.20)$$

where $(N_{c,i})_{stall}$ is the circulatory normal force during stall conditions and $(N_{a,i})_{stall}$ is the apparent-mass normal force during stall conditions. The resultant force in the chord-wise direction is given by,

$$(R_{a,i})_{stall} = (T_{s,i})_{stall} - (D_{f,i})_{stall} \qquad (C.21)$$

where $(D_{c,i})_{stall}$ is the viscous drag force due to skin friction and $(T_{s,i})_{stall}$ is the leading-edge suction force. The circulatory normal force is given by,

$$\left(N_{c,i}\right)_{stall} = \left(C_a\right)\frac{\rho U_i V_{n,i}}{2} c_i l_i \qquad (C.22)$$

where $V_{n,i}$ is the free-stream velocity in normal to the wing profile. The apparent-mass effect normal force is given by,

$$\left(N_{a,i}\right)_{stall} = \frac{N_{a,i}}{2} = \frac{1}{8}\rho\pi c_i^2 \left(U_i \dot{\alpha}'\right)l_i \qquad (C.23)$$

The viscous drag force is given by,

$$D_{f,i} = C_a \frac{\rho V_{a,i}^2}{2} c_i l_i \qquad (C.24)$$

The leading-edge suction force is given by,

$$T_{s,i} = \eta_s 2\pi\left(\alpha'\right)^2 \frac{\rho U_i V_{a,i}}{2} c_i l_i \qquad (C.25)$$

C.6 Dynamic Stall Condition

The angle of the attack at which full flow separation occurs over the upper surface of the wing changes as the angle of attack is changed dynamically. Dynamic stall occurs at higher angles of attack due to delayed flow separation and the suction force created by the opposed turbulent vortices at the leading and trailing edge. In [35], this is modeled as the angular difference between static and effective (dynamic) stall as,

$$\left(\alpha_{stall}\right)_{ef} - \left(\alpha_{stall}\right)_{st} = \Delta\alpha = \xi\sqrt{\frac{c\dot{\alpha}}{2U}} \tag{C.26}$$

where ξ is determined experimentally and is dependent on the local Mach number.

$$\Delta\alpha = 0.51\left(\frac{\dot{\alpha}}{\dot{\alpha}_{mag}}\right)\sqrt{\frac{c\dot{\alpha}_{mag}}{2U}} \tag{C.27}$$

$$\dot{\alpha}_{mag} = \left|\dot{\alpha}\right|$$

APPENDIX D

CFD MODELING

A CFD model to determine the aerodynamic performance of the wing as it reaches high angle of attack is developed as part of another subtask for this research. A 2D static model is developed for a thin plate with equivalent dimensions to that of the wing used for prototype testing. The wing is subjected to wind and pressure conditions similar to that of wind tunnel testing. To vary the angle of attack, the direction of the velocity vector towards the horizontally aligned wing cross sectional geometry is incrementally changed with results analyzed. Initially the velocity vector is parallel to the wing and then increased at 10° increments until 90° angle of attack is reached. Using CFD modeling, the coefficient of lift, C_l, and drag, C_d, are calculated. The results of CFD modeling are compared to wind tunnel testing results to ensure validity of the modeling and provide insight of the flight characteristics with an infinite wing. As mentioned in Chapter 6, although the results vary in magnitude, a similar trend indicates acceptable correlation between CFD modeling and wind tunnel testing. These results also provide information about the aerodynamic performance of the wing at high angle of attack.

APPENDIX E

PROTOTYPE TESTING PLOTS

Prototype testing is conducted at various testing speeds to interpret the forces produced by Figure-8 wing motion. Additionally, a comparison of results is made with the force model created in SIMULINK® SimMechanics. The experimental testing of the prototype is conducted at 2.5 Hz, 5 Hz, 7.5 Hz, 10 Hz, and 12.25 Hz. With a discussion of the results for 12.25 Hz presented in Chapter 7, the remaining testing results will be discussed in this section.

To determine the filtering frequency, the FFT of chord-wise force, F_x, and normal force, F_y, is examined. For the data plotted in Chapter 7 for 12.25 Hz flapping frequency, the cutoff frequency was determined to be 50 Hz. From the FFT of the F_x, Figure E.1, maximum amplitude of 1.4 is at 12.21 Hz, which indicates the testing frequency of the prototype. Frequencies beyond 12.21 Hz have lower amplitudes and at 49 Hz, lower order amplitude of 0.2 is reached. The FFT of F_y, Figure E.2, shows maximum amplitude of 1.3 at 21.41 Hz. The double cycle in the y direction during the Figure-8 motion corresponds to the double testing frequency displayed for F_y. Similarly, frequencies beyond the testing frequency begin to diminish and amplitude of 0.59 is reached at 49 Hz. Therefore, the cutoff frequency for 12.25 Hz prototype testing is determined to be 50 Hz.
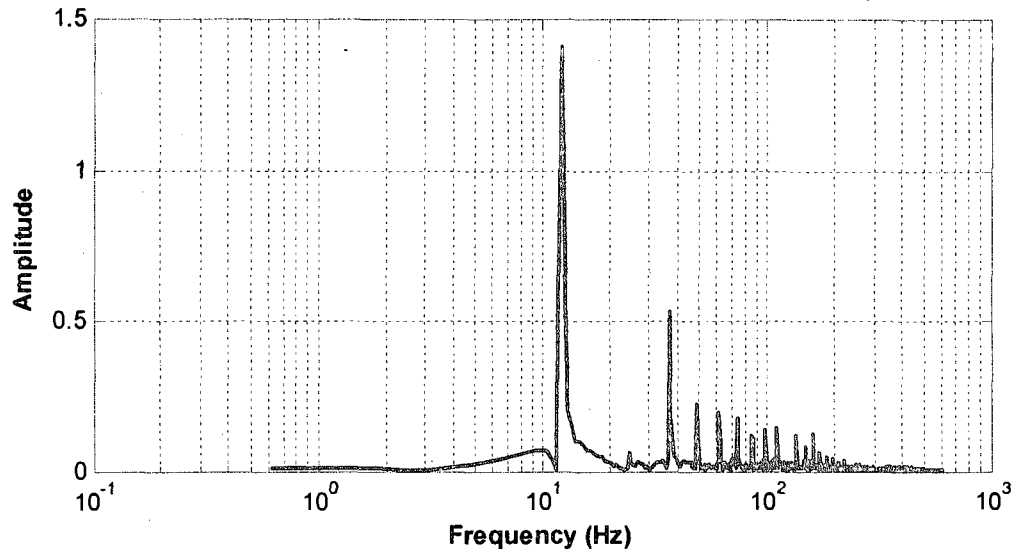
Figure E.1   Unfiltered Data FFT for Chord-wise Force, F_x, at 12.25 Hz
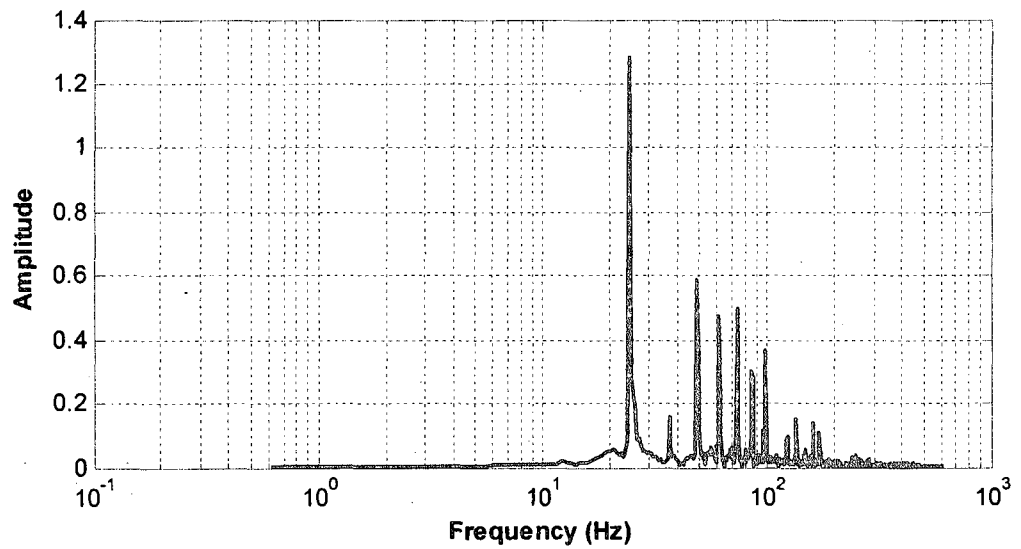
Figure E.2   Unfiltered Data FFT for Normal Force, F_y, at 12.25 Hz

For filtering at 2.5 Hz testing, an analysis of the FFT for both F_x and F_y is used to locate the cutoff filtering frequency. From the FFT of F_x, Figure E.3, we notice maximum amplitude for the testing frequency and lower amplitude thereafter. Twice the testing frequency is indicated for F_y, Figure E.4, because of the double cycle and frequencies beyond 20 Hz indicate the noise in the signal. Therefore, for prototype testing results at 2.5 Hz flapping, 20 Hz is determined to be the cutoff frequency. This FFT analysis methodology is applied to all testing frequencies to determine the most adequate cutoff frequency.
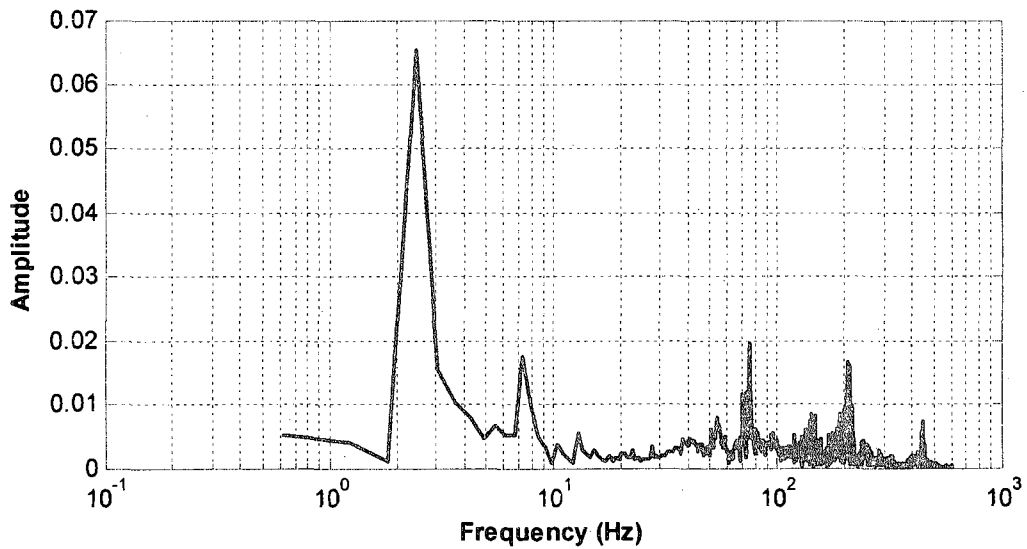
Figure E.3   Unfiltered Data FFT for Chord-wise Force, F_x, at 2.5 Hz
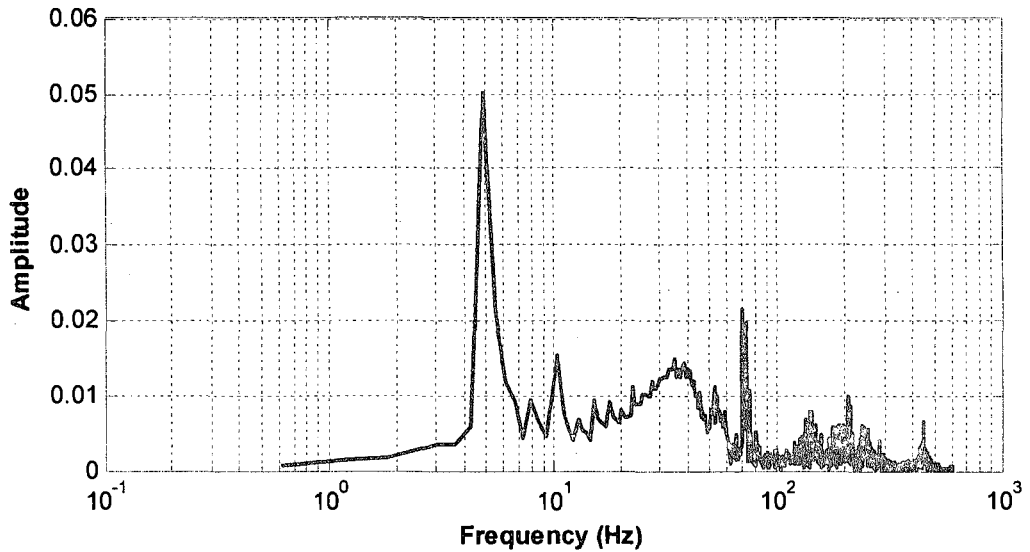
Figure E.4   Unfiltered Data FFT for Normal Force, F_y, at 2.5 Hz

The plots below, Figures E.5-E.13, show the comparison of the experimental and model results for testing at 2.5 flapping frequency. Good correlation is seen in chord-wise force, F_x, and the normal force, F_y. To eliminate noise, the experimental force signal was filtered at 20 Hz as determined by the FFT of F_x and F_y. Difference in experimental results could account factors discussed in Chapter 7. For the span-wise force, F_z, the difference in signal could be explained by any looseness in joints creates force along this direction and cannot be reflected in the model. Overall good correlation is seen with model and experimental results.
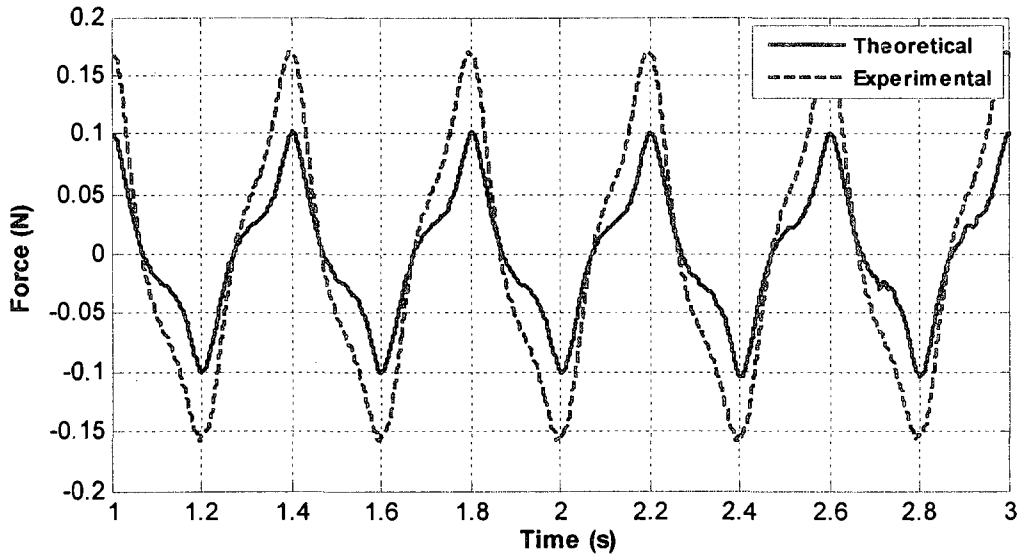
Figure E.5   Chord-wise Force, F_x, at 2.5 Hz
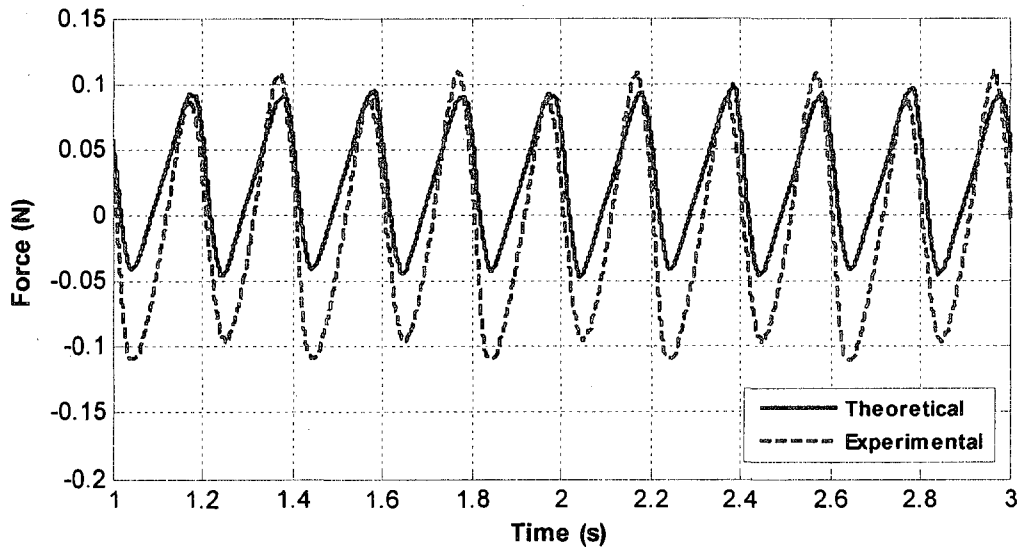
Figure E.6   Normal Force, F_y, at 2.5 Hz
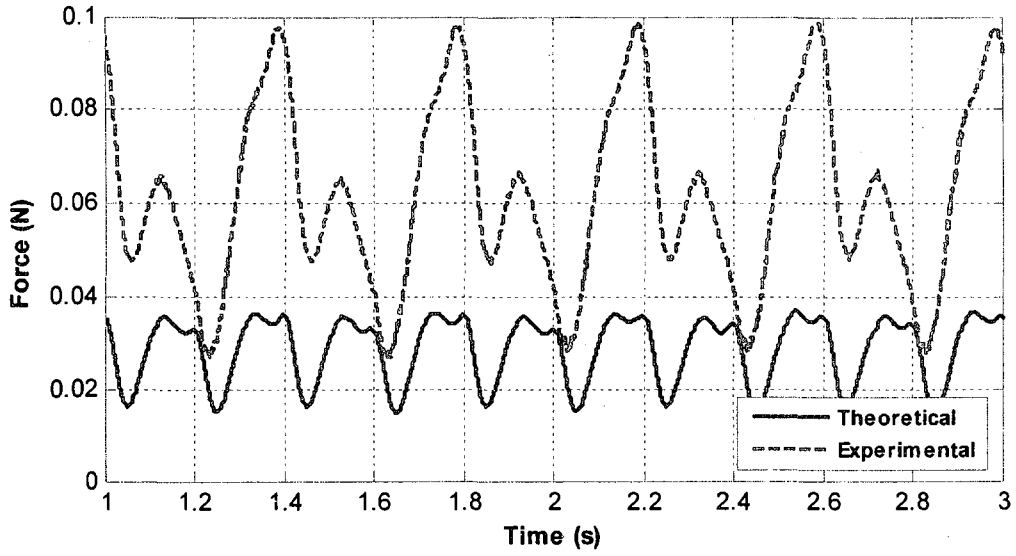
Figure E.7   Span-wise Force, F_z, at 2.5 Hz
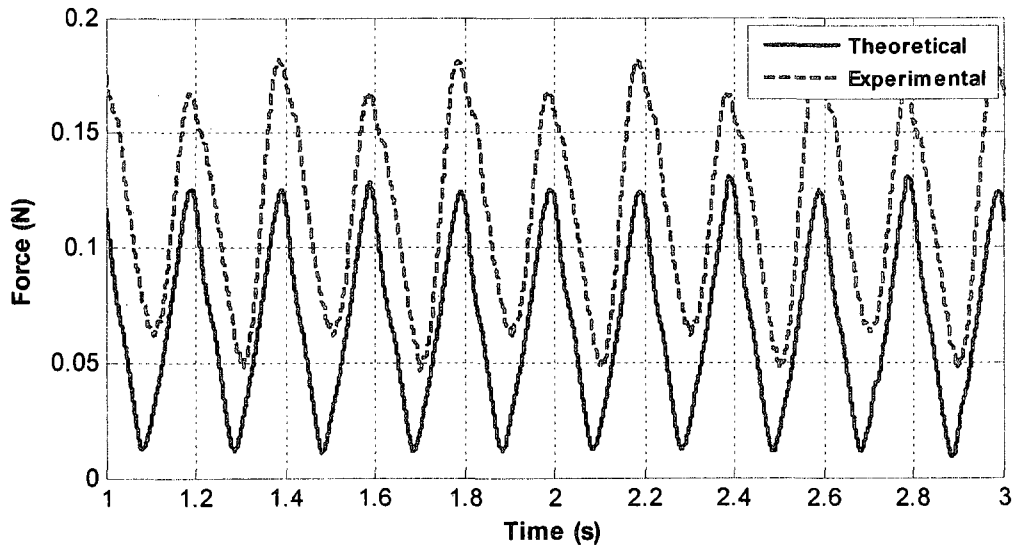
Figure E.8   Force Magnitude of Chord-wise, F_x, and Normal Force, F_y, at 2.5 Hz
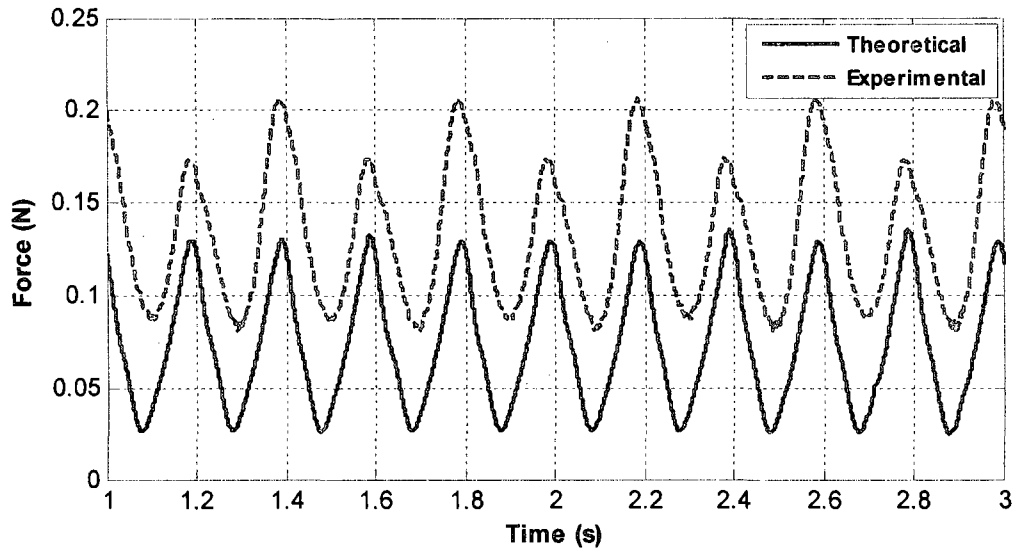
Figure E.9   Force Magnitude, F, at 2.5 Hz
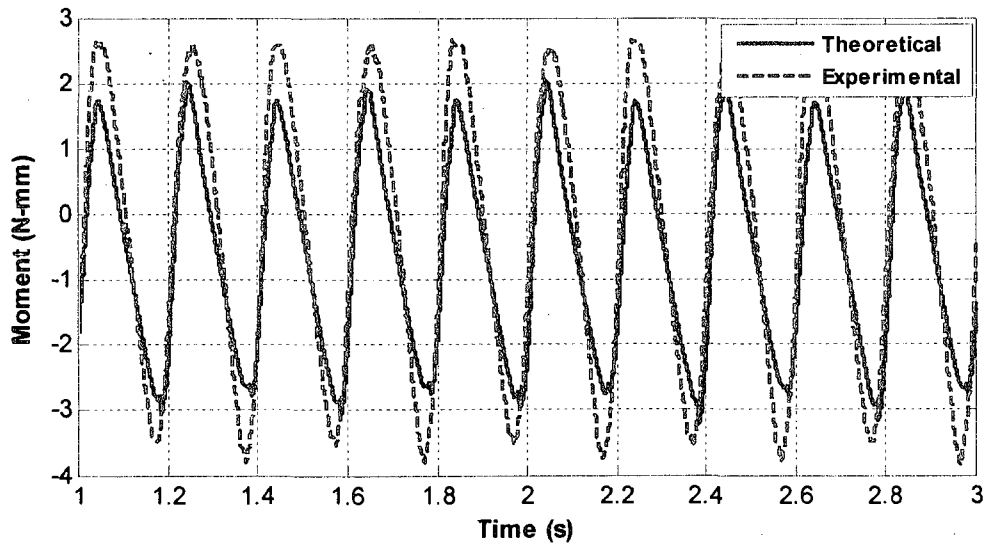
Figure E.10   Moment, M_x, at 2.5 Hz
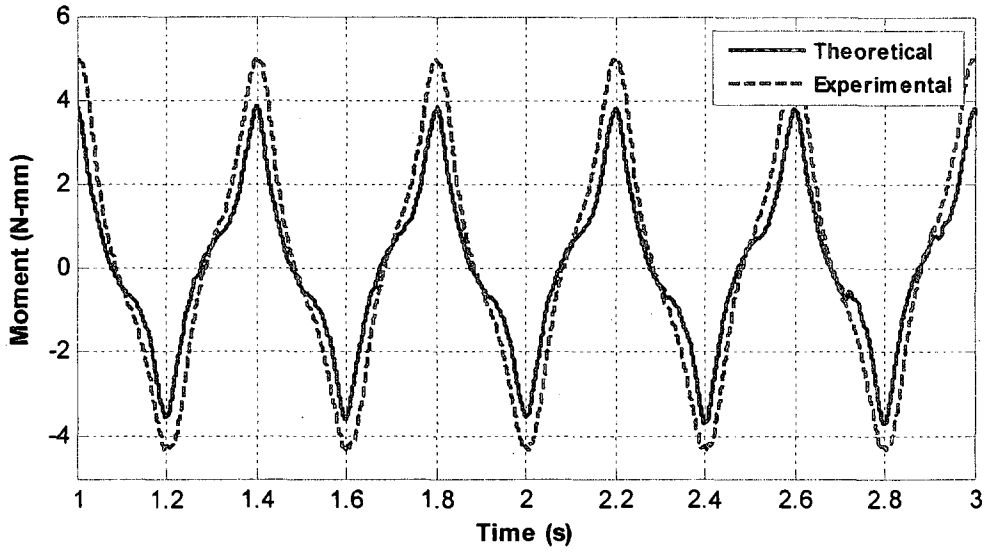
Figure E.11   Moment, M$_y$, at 2.5 Hz
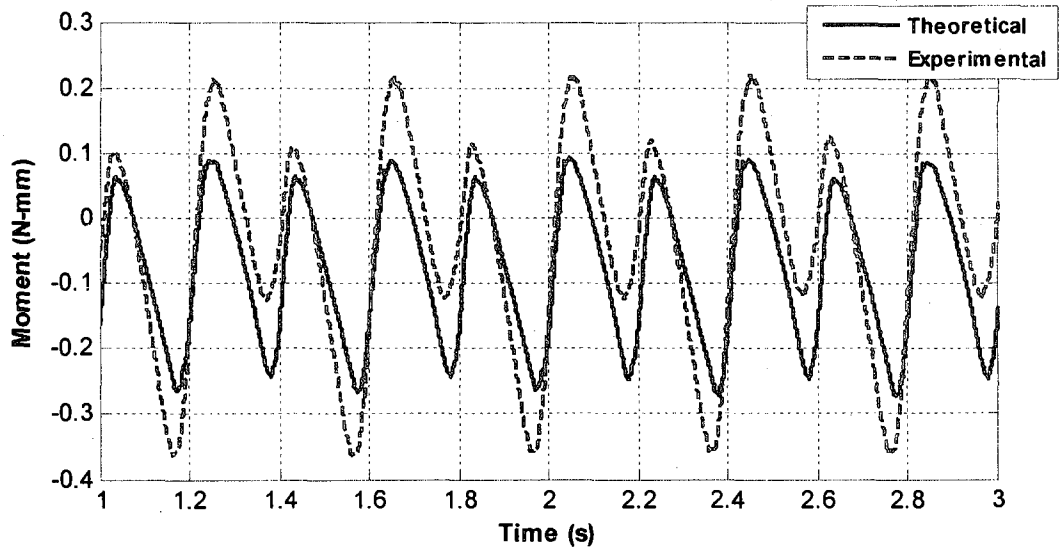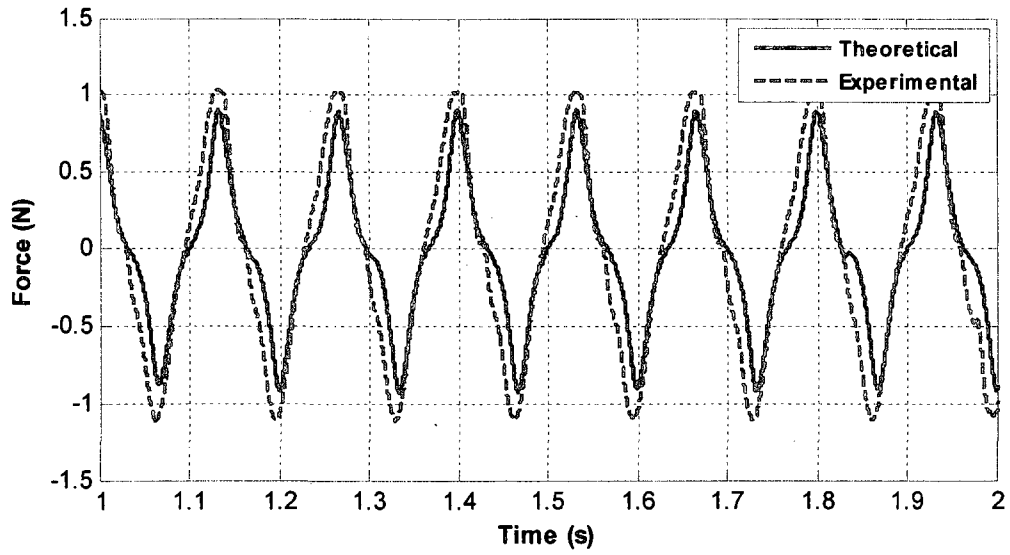

Figure E.12   Moment, M_z, at 2.5 Hz
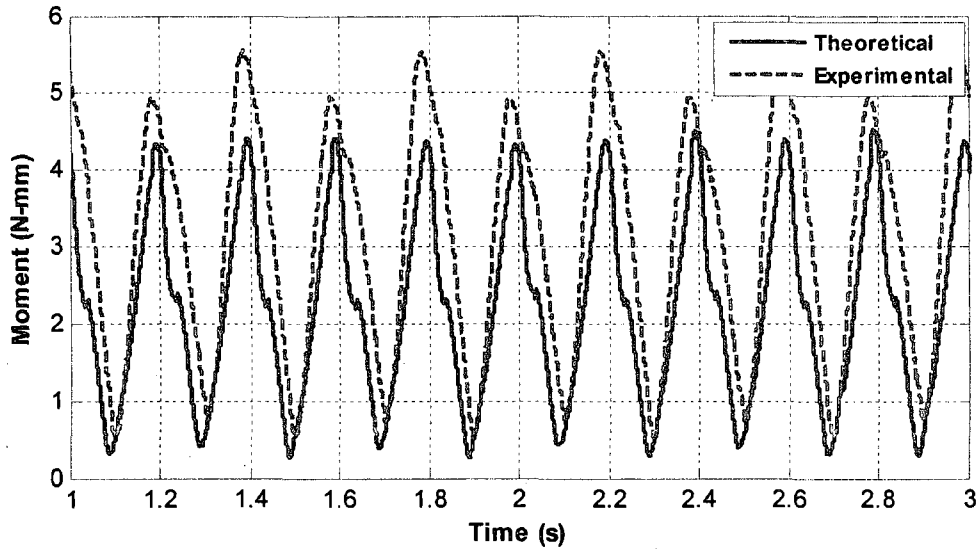
Figure E.13   Moment Magnitude, *M*, at 2.5 Hz

For 5 Hz testing, good correlation is seen the components that have aerodynamic contribution. A comparison of the model and experimental results for each force component is shown in Figures E.14 to E.22. Good correlation is seen in chord-wise force, F_x, and the normal force, F_y. To eliminate noise, the experimental force signal was filtered at 25 Hz as determined by the FFT of F_x and F_y. Difference in experimental results could account factors discussed in Chapter 7. For the span-wise force, F_z, the difference in signal could be explained by any looseness in joints creates force along this direction and cannot be reflected in the model. Overall good correlation is seen with model and experimental results.
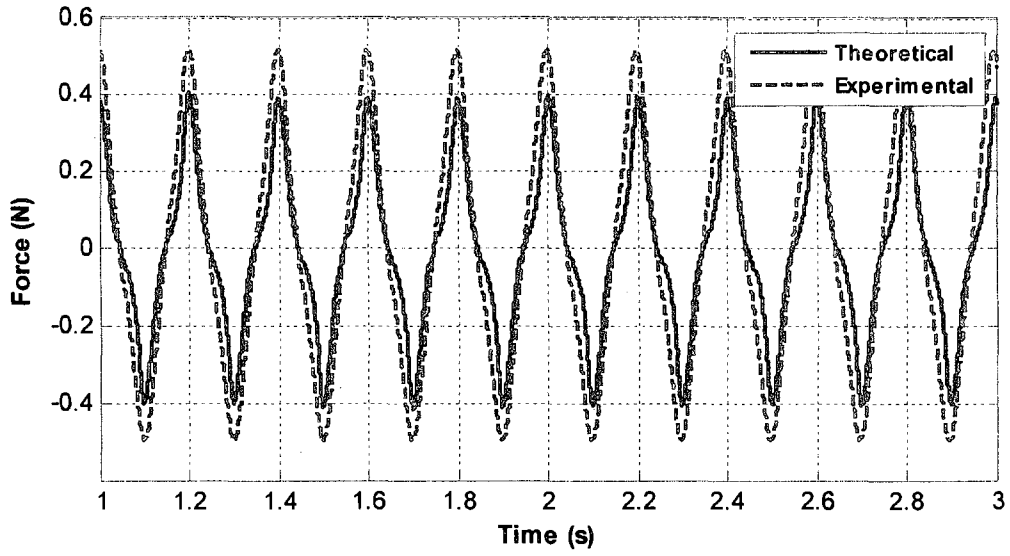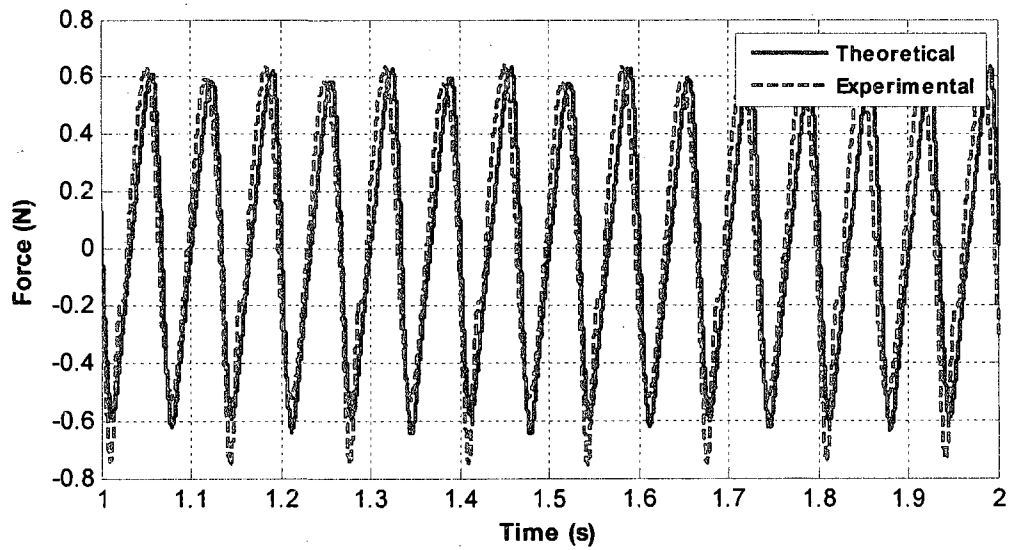
Figure E.14   Chord-wise Force, F_x, at 5 Hz
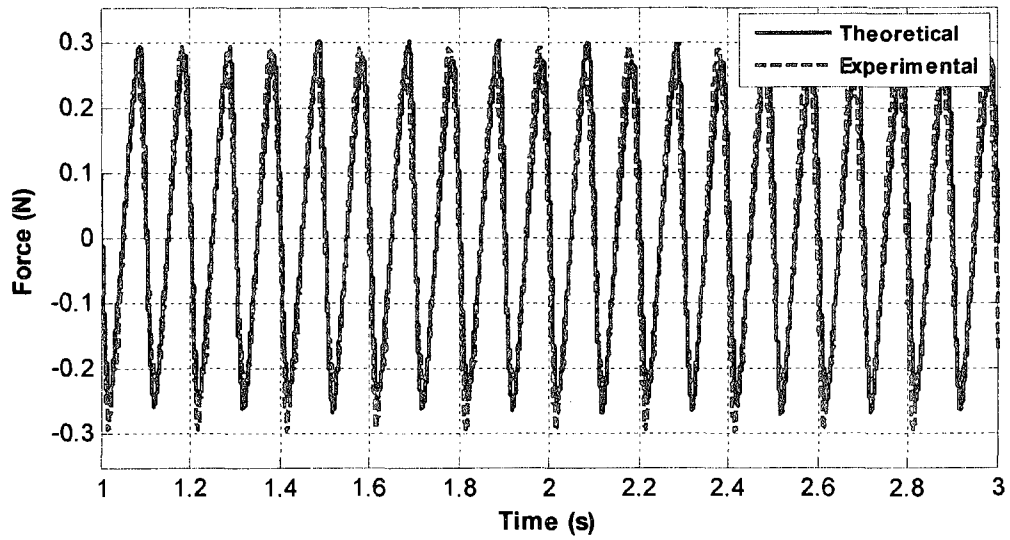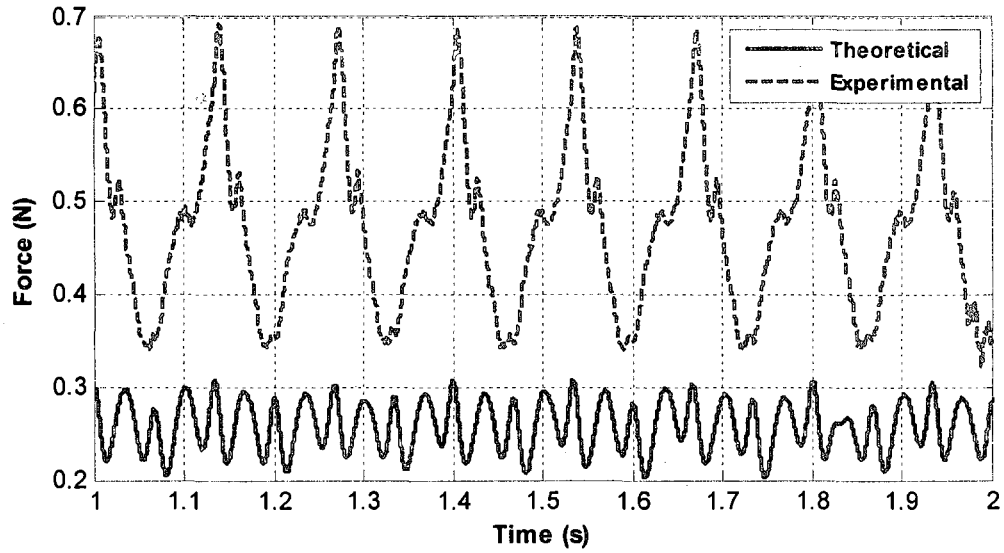

Figure E.15   Normal Force, F_y, at 5 Hz
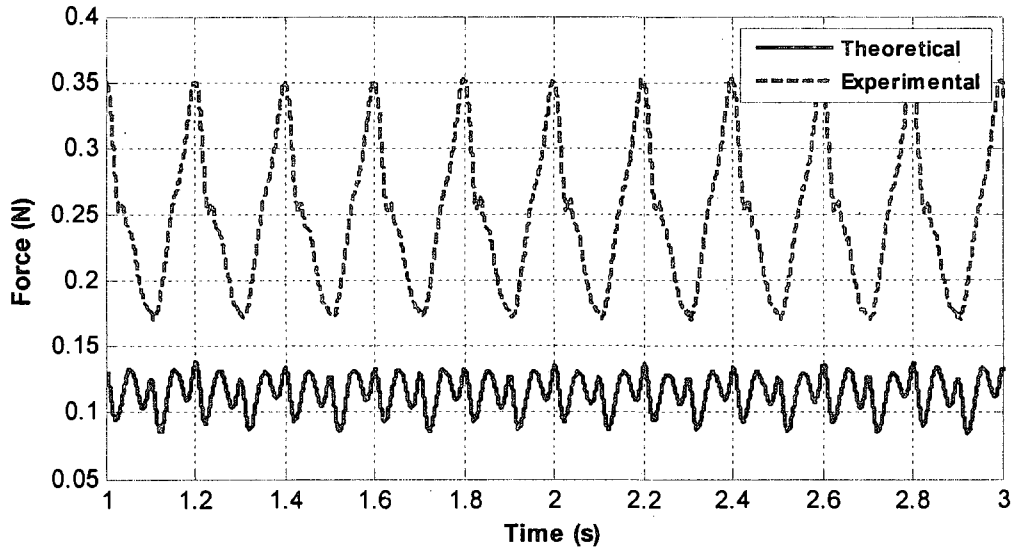
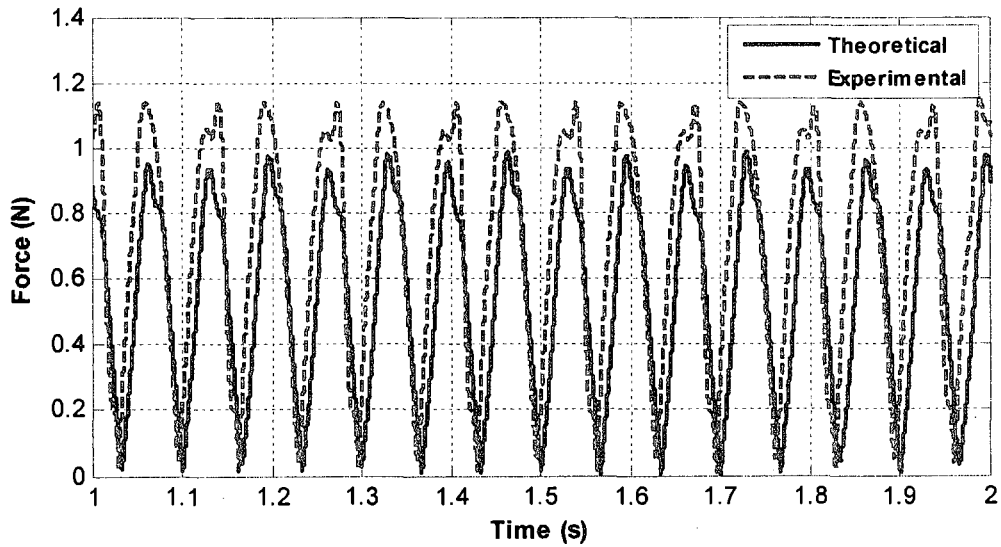Figure E.16   Span-wise Force, F_z, at 5 Hz
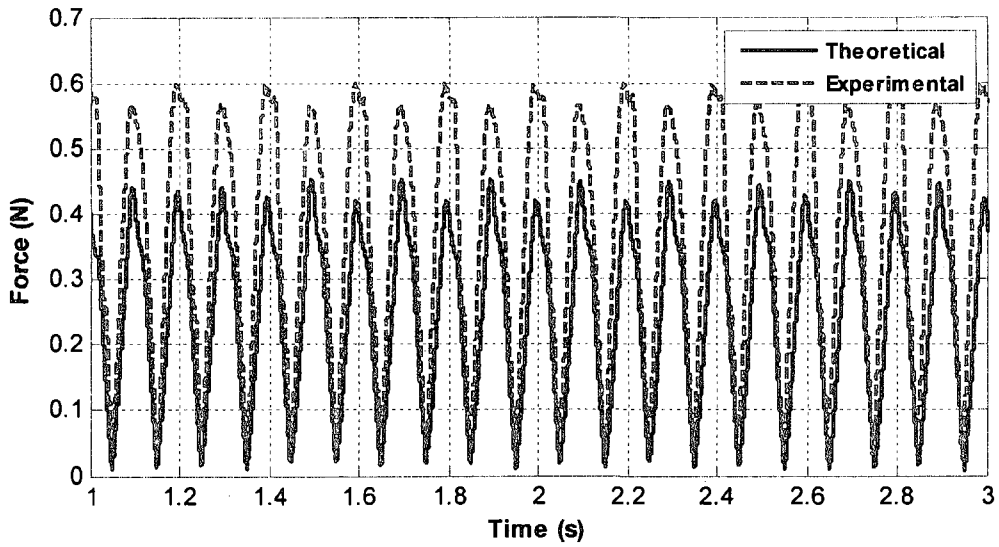
Figure E.17   Force Magnitude of Chord-wise, F_x, and Normal Force, F_y, at 5 Hz
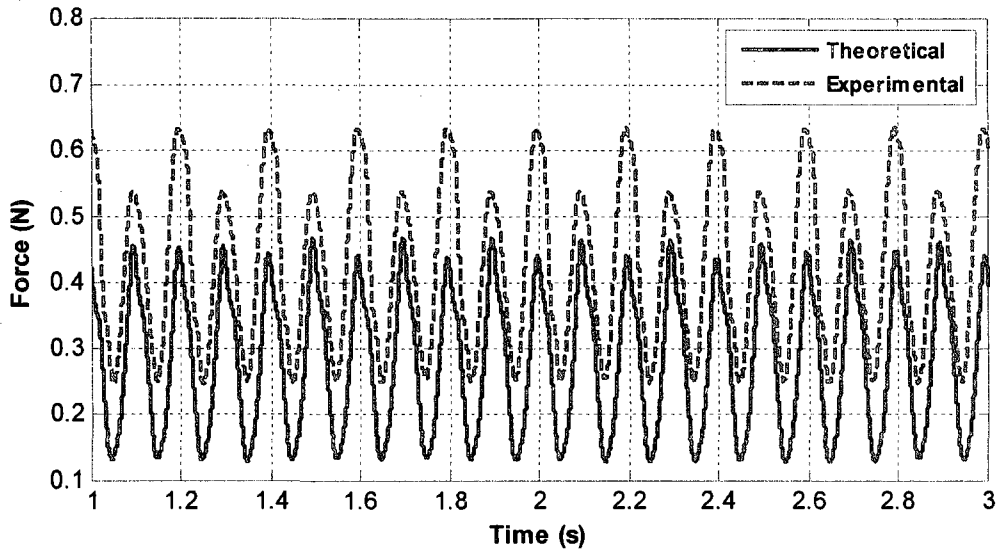
Figure E.18   Force Magnitude, *F*, at 5 Hz
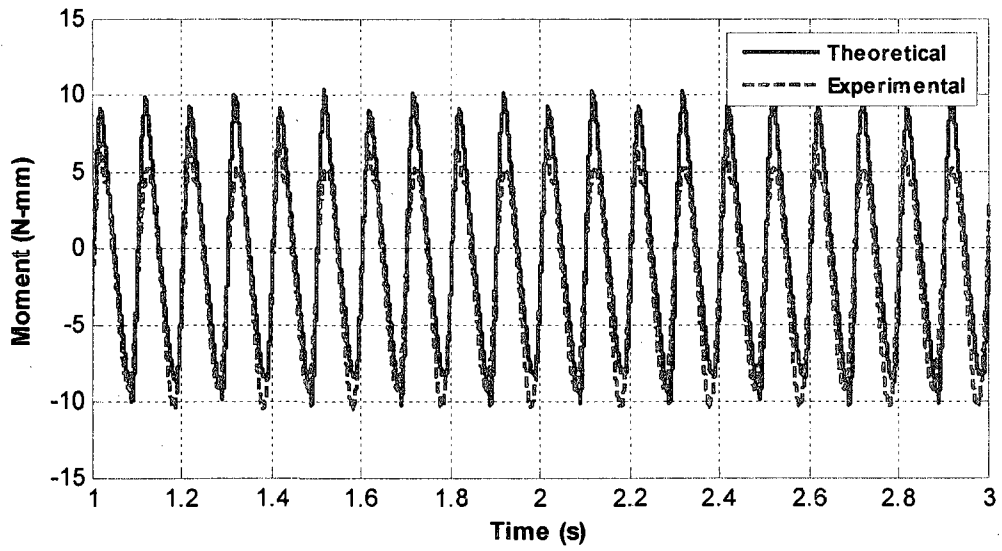

Figure E.19   Moment, M_x, at 5 Hz
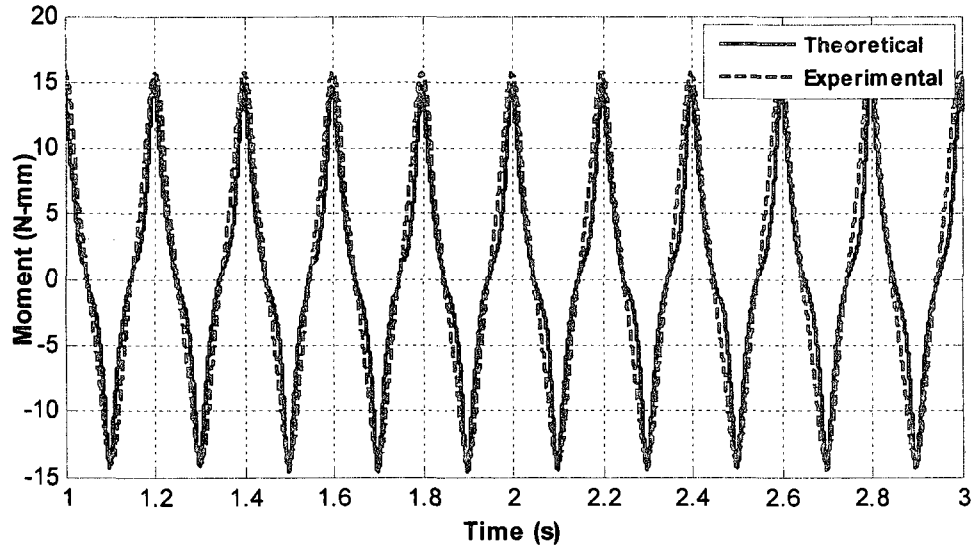
Figure E.20   Moment, M_y, at 5 Hz
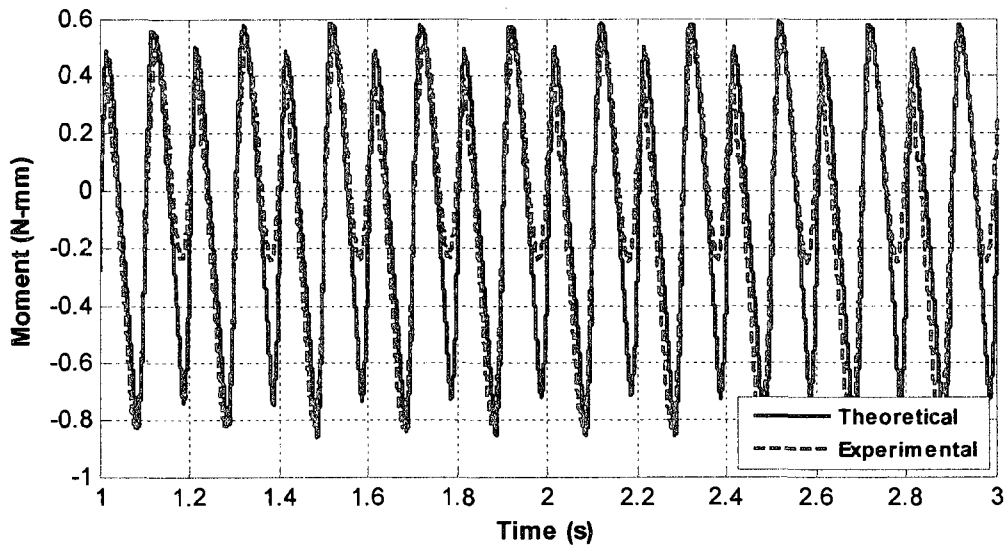
Figure E.21   Moment, M_z, at 5 Hz
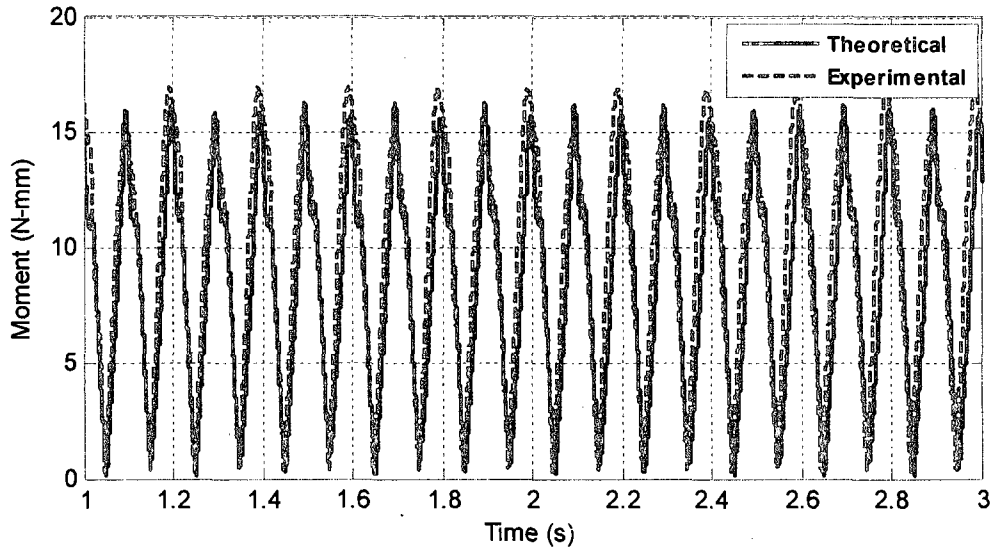
Figure E.22   Moment Magnitude, *M*, at 5 Hz

Similarly, good correlation in results between model and experimental data is seen at 7.5 Hz flapping frequency. A comparison of the model and experimental results for each force component is shown in Figures E.23 to E.31. Good correlation is seen in chord-wise force, F_x, and the normal force, F_y. To eliminate noise, the experimental force signal was filtered at 35 Hz as determined by the FFT of F_x and F_y. Difference in experimental results could account factors discussed in Chapter 7. For the span-wise force, F_z, the difference in signal could be explained by any looseness in joints creates force along this direction and cannot be reflected in the model. Overall good correlation is seen with model and experimental results.

Figure E.23   Chord-wise Force, F_x, at 7.5 Hz

Figure E.24   Normal Force, F_y, at 7.5 Hz

Figure E.25   Span-wise Force, F_z, at 7.5 Hz

Figure E.26   Force Magnitude of Chord-wise, F_x, and Normal Force, F_y, at 7.5 Hz
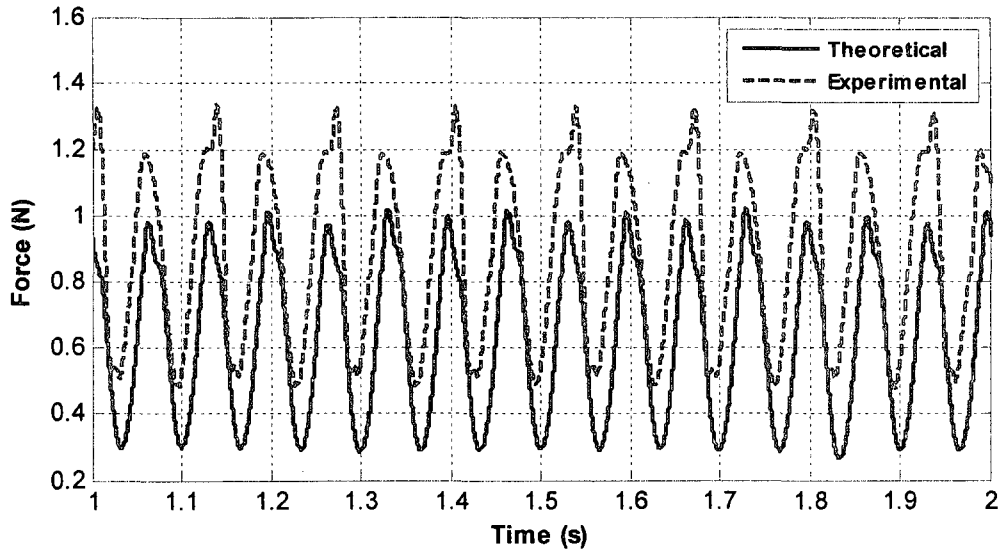
Figure E.27   Force Magnitude, F, at 7.5 Hz
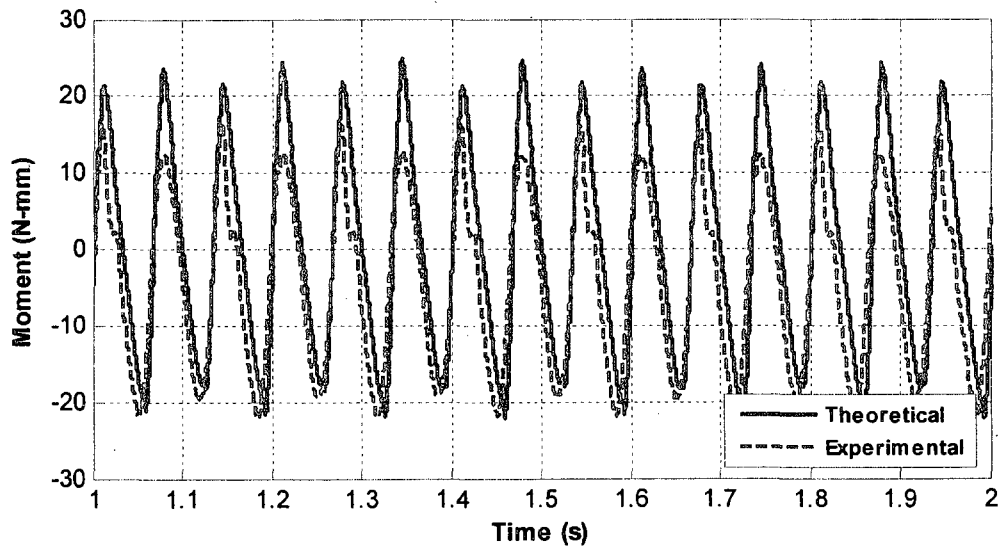
Figure E.28   Moment, M_x, at 7.5 Hz
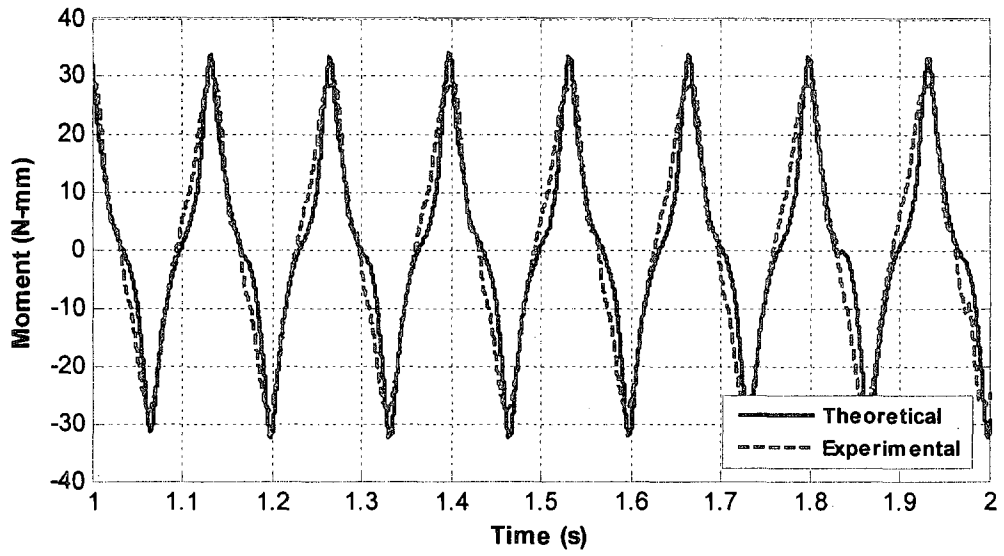
Figure E.29   Moment, M_y, at 7.5 Hz
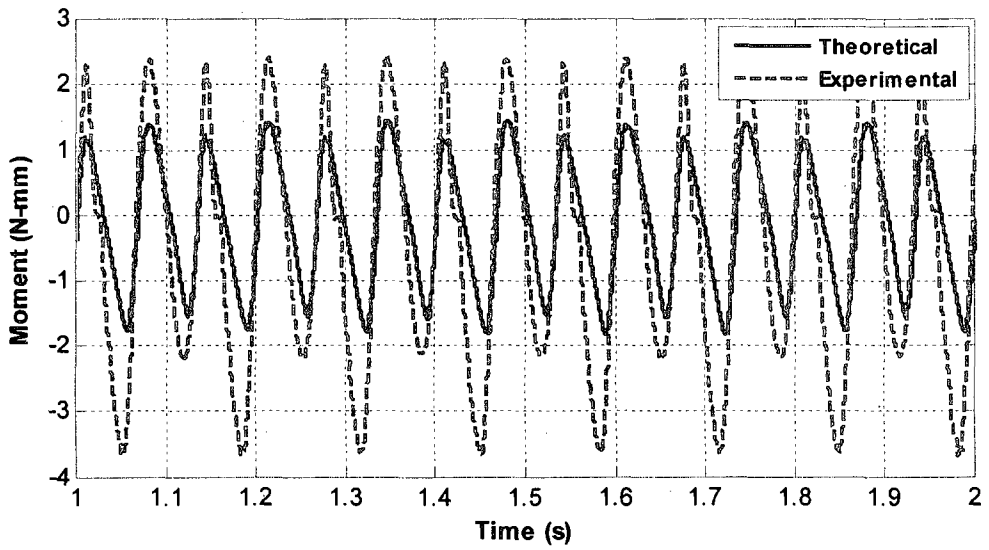
Figure E.30   Moment, M_z, at 7.5 Hz

140
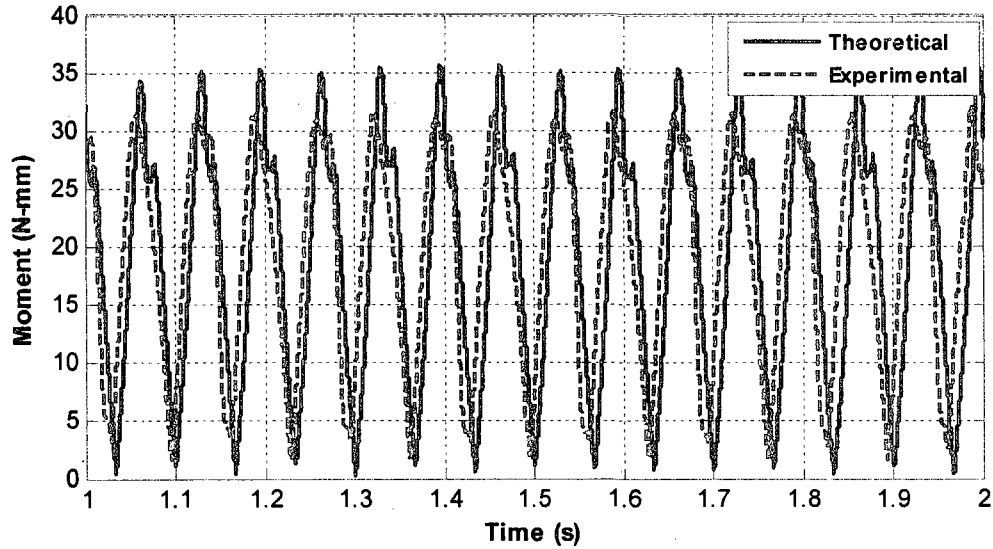
Figure E.31   Moment Magnitude, *M*, at 7.5 Hz

For 10 Hz testing, good correlation is seen the components that have aerodynamic contribution. A comparison of the model and experimental results for each force component is shown in Figures E.32 to E.40. Good correlation is seen in chord-wise force, F_x, and the normal force, F_y. To eliminate noise, the experimental force signal was filtered at 40 Hz as determined by the FFT of F_x and F_y. Difference in experimental results could account factors discussed in Chapter 7. For the span-wise force, F_z, the difference in signal could be explained by any looseness in joints creates force along this direction and cannot be reflected in the model. Overall good correlation is seen with model and experimental results.
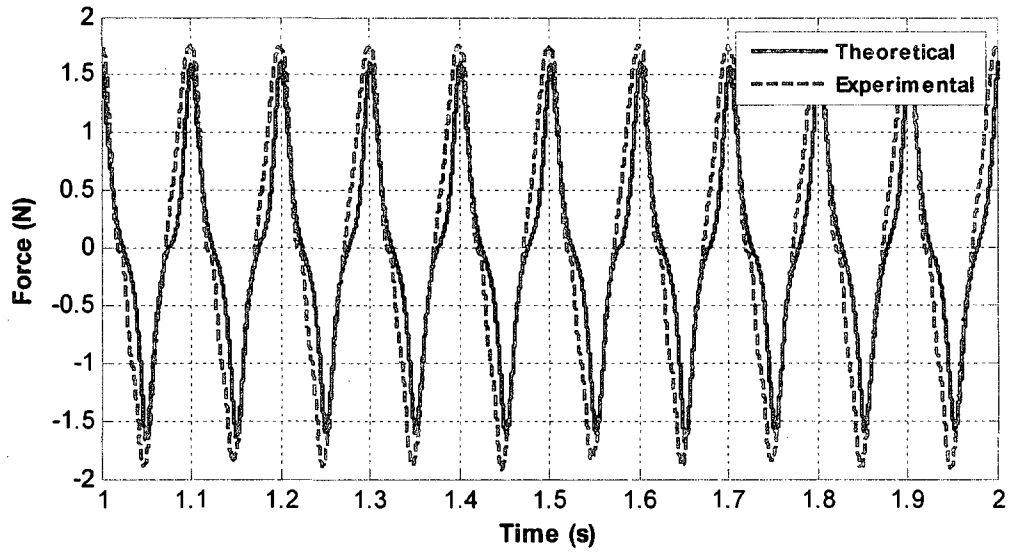
Figure E.32   Chord-wise Force, F_x, at 10 Hz
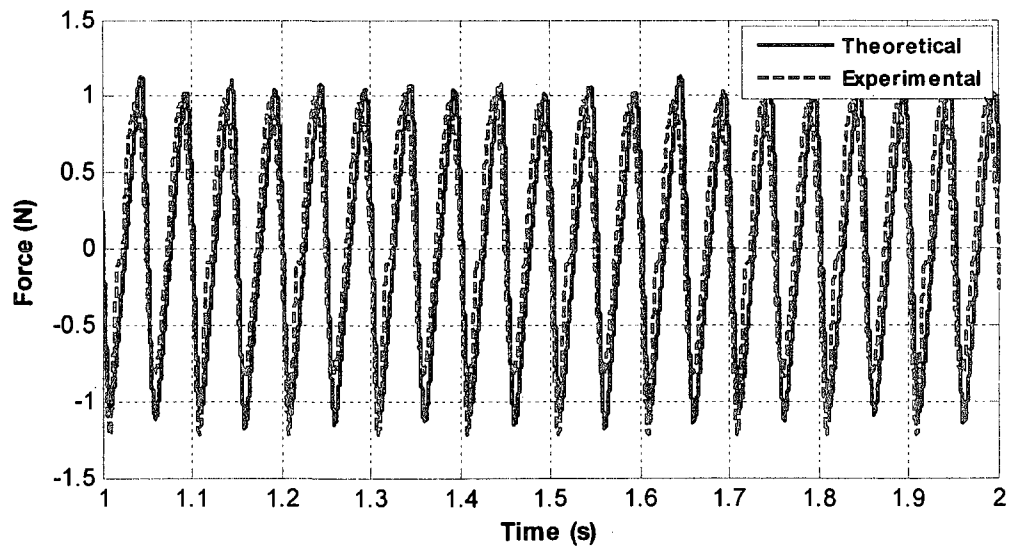
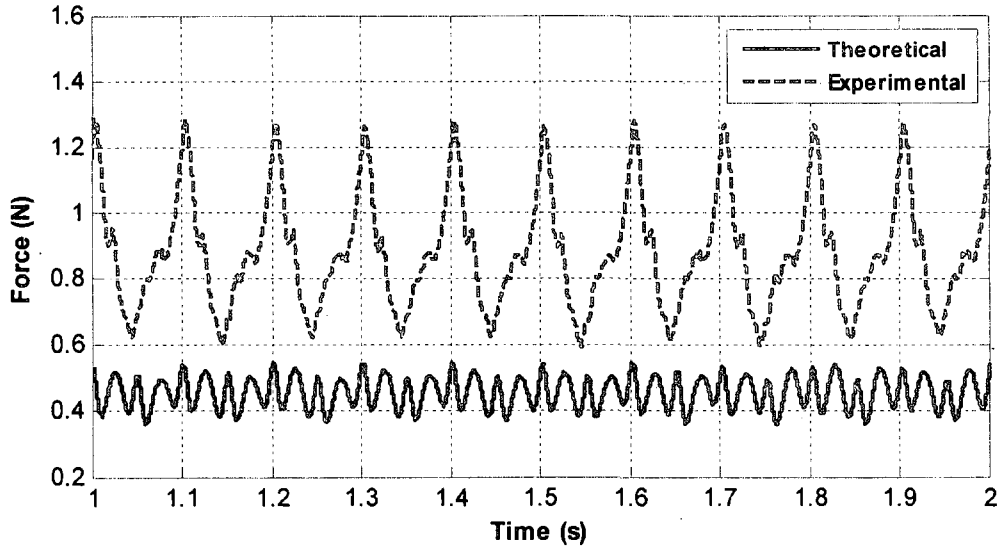
Figure E.33   Normal Force, F_y, at 10 Hz

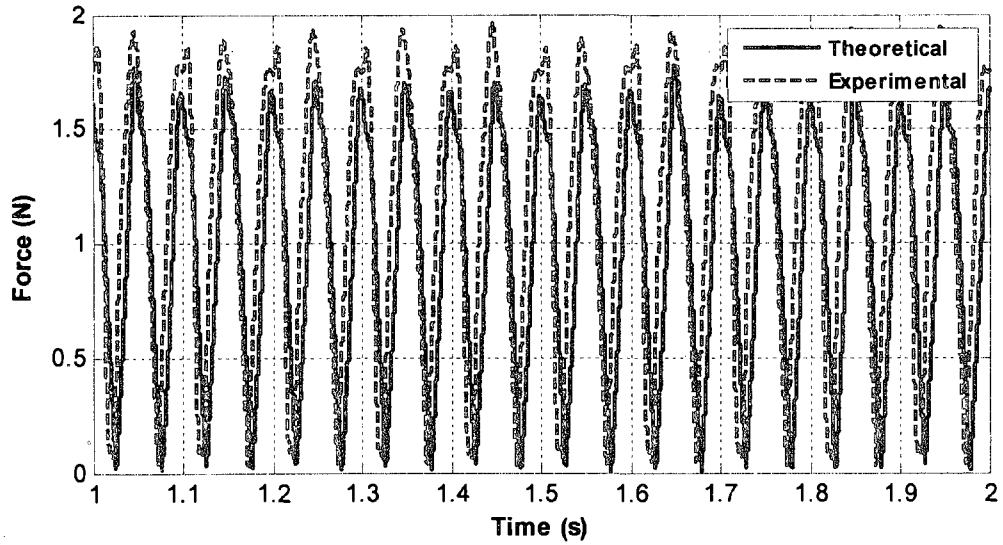Figure E.34   Span-wise Force, F_z, at 10 Hz

Figure E.35   Force Magnitude of Chord-wise, F_x, and Normal Force, F_y, at 10 Hz
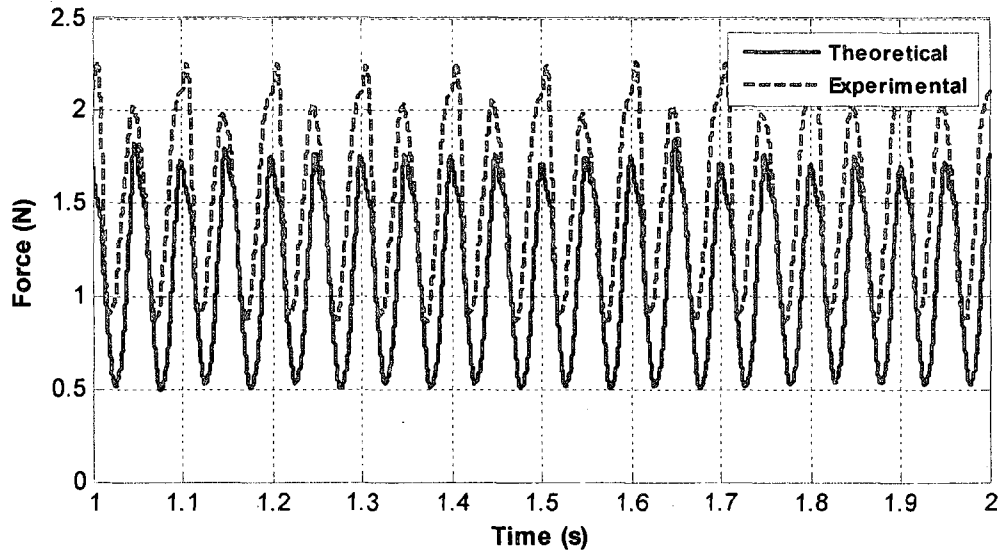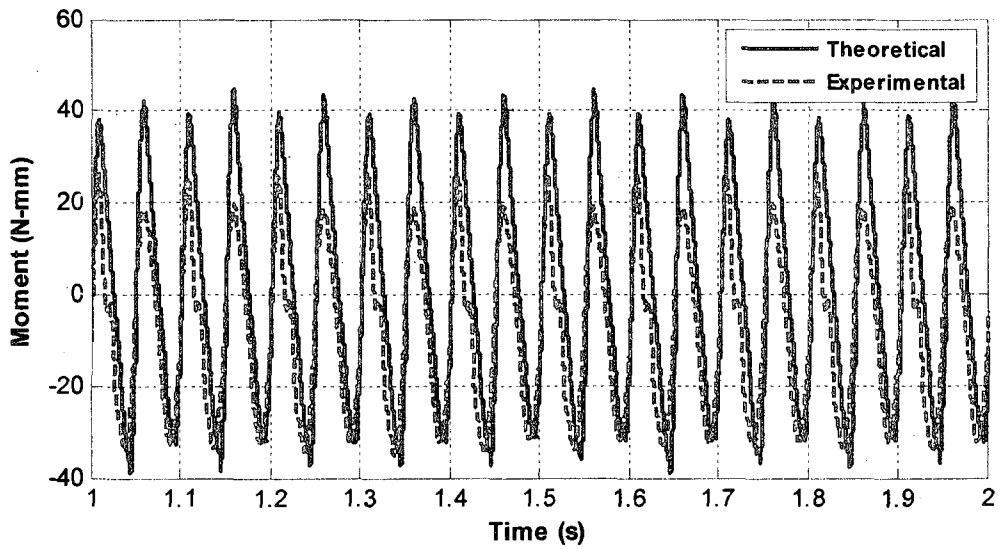
Figure E.36   Force Magnitude, *F*, at 10 Hz

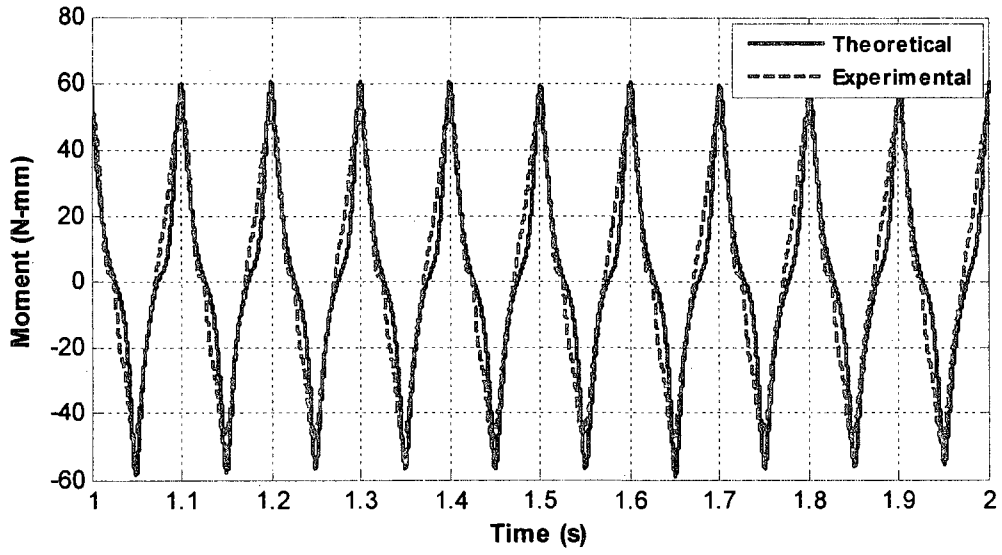Figure E.37   Moment, M_x, at 10 Hz

Figure E.38   Moment, M_y, at 10 Hz
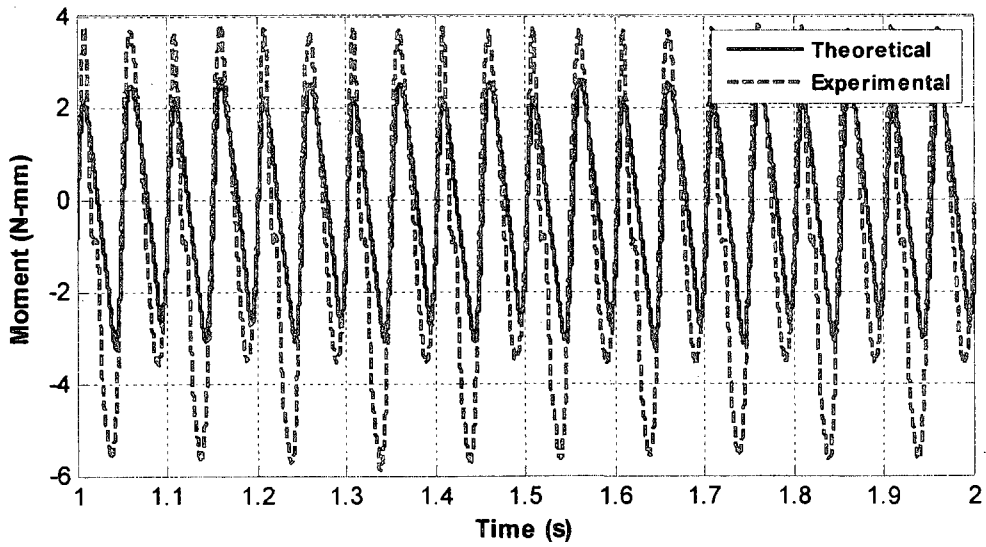

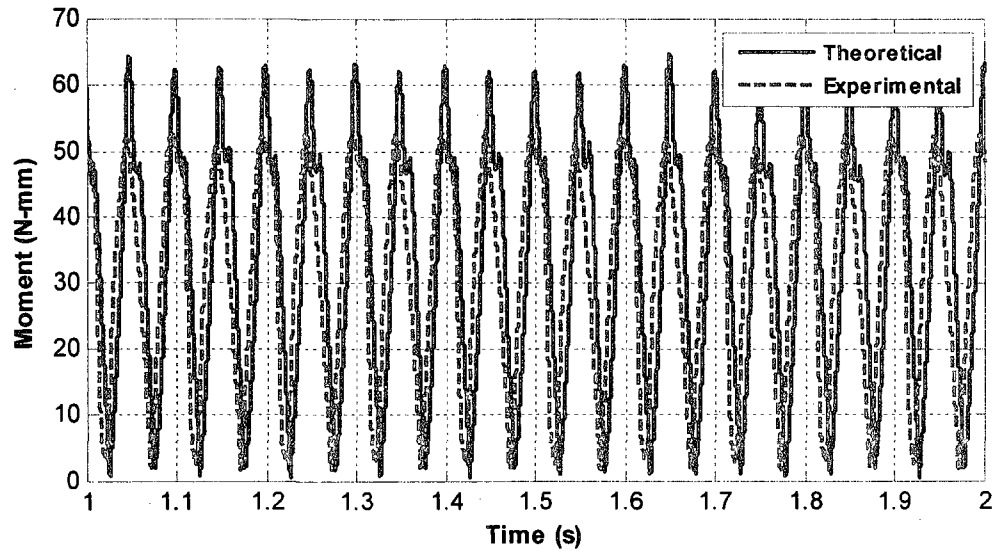Figure E.39   Moment, M_z, at 10 Hz

Figure E.40   Moment Magnitude, *M*, at 10 Hz

VITA

Graduate College
University of Nevada, Las Vegas

Zohaib Parvaiz Rehmat

Home Address:
5622 Sage Pines Drive
Las Vegas, NV 89118

Degrees:
Bachelor of Science, Mechanical Engineering Technology
Vaughn College of Aeronautics and Technology

Publications:
Design of "Figure-8" Spherical Motion Flapping Wing for Miniature UAV (submitted)
Flight Characteristics of Flapping Wing Miniature Air Vehicles with "Figure-8" Spherical Motion (submitted)

Thesis Title:
Design of a "Figure – 8" Spherical Motion Flapping Wing for Miniature UAV's

Thesis Examination Committee:
Co-Chairperson, Mohamed B. Trabia, Ph.D.
Co-Chairperson, Woosoon Yim, Ph.D.
Committee Member, Georg Mauer, Ph.D.
Committee Member, Brendan J. O'Toole, Ph.D.
Graduate Faculty Representative, Edward Neumann, Ph.D.